THE UNIVERSITY OF HULL

Optimisation and Frequency Tuning Concepts for a

Vibration Energy Harvester

being a Thesis submitted for the Degree of

Doctor of Philosophy

in the University of Hull

by

Beng Lee Ooi, MEng. (Hull)

DECEMBER 2010

Abstract

With current electronic designs becoming more versatile and mobile, applications that were wired and bulky before have now seen a great reduction in size and increase in portability. However, the issue is that the scaling down in size and cost of electronics has far outpaced the scaling up of energy density in batteries. Therefore, a great deal of research has been carried out to search for alternative power sources that can replace or enhance the conventional battery. Energy harvesting (also known as energy scavenging) is the process whereby ambient energy is captured and stored. The ambient energy here refers to energy that is pre-existing in nature, and is self-regenerating and has extended life time from a battery.

After reviewing many possible energy scavenging methods, the conversion of ambient vibrations to electricity is chosen as a method for further research. There are plenty of different methods to transform ambient vibration to electricity, but in this research only piezoelectric and electromagnetic conversions are pursued. In order to harvest the most energy with the harvesting device, the harvester's fundamental mode must be excited. However, this is not always possible due to fluctuations in the frequency of the vibration source. By being able to change the natural frequencies of the device, the harvester could be more effective in capturing ambient energy.

In this thesis, the behaviour of the various types of energy sources is studied and the obtained information is later used to generate a vibration signal for subsequent simulation and experiments. A converter based on a piezoelectric bimorph is investigated. The resultant outputs from the design are compared to the model and the analysis is presented. The mechanical strain distributions on the beam's surface for five different

geometric structures are compared and discussed. This is followed by a discussion of the feasibility of improving the strain distribution by changing the beam's depth (height) along the cantilever beam length. Lastly, a novel frequency tuning method, which involves applying a different effective electrical damping in different quadrants of the oscillating cycle, is proposed. The results of this analysis are presented, along with experimental results that indicate that the behaviour of the system can be changed over a limited range by changing the effective electrical damping during the oscillation cycle.

Table of Contents

List of Figures

List of Tables

List of Symbols

n = Carnot efficiency

k = spring constant

m = seismic mass

ω_n= system initial resonant frequency

ω = driving frequency

ξ_T=total damping ratio

ξ_m= mechanical damping ratio

ξ_e= electrical induced damping ratio

Y= displacement amplitude/Young's modulus

A= vibration acceleration amplitude

Q=electric charge

ε= dielectric constant/mechanical bending strain

σ=mechanical stress

d= distance / piezoelectric strain coefficient

k_e= emf constant

B = magnetic field

L=length

$\emptyset$ = phase shift

Kc= vibrator calibration constant

Cp = capacitance across the piezoelectric device

Yc = Young's modulus for piezoelectric ceramic

Ys= Young's modulus for piezoelectric centre shim

tc = thickness of an individual piezoelectric ceramic layer

k_{co}= electro-mechanical coupling coefficient

l_b=piezoelectric beam length

l_e=piezoelectric bender electrode length

l_m=tip mass length for piezoelectric bender

m_{eff}= effective mass of a cantilever beam

m_{tip}= tip mass for a cantilever beam

m_{beam}= cantilever beam mass

M=mechanical bending moment

h = beam height

b = total damping coefficient/distance from centre of the shim to the centre of the piezo layers/beam width

b_e= electrical induced damping coefficient

b_m= mechanical damping coefficient

b_{free}= beam free end width

b_o=beam fixed end width

I = moment of inertia

E=material Young's modulus

ε_{ratio} = Strain Ratio

ε_M= maximum Strain Ratio

ε_{total} =sum of the strain ratio in a structure

$\varepsilon_{average}$ = average strain for a structure

ε_{normal} = normalised average strain against the analytical structure 1

η_b= total of available nodes across a beam width

η_{total}= total available nodes in a structure

$\eta_{\%}$= number of nodes in percentage

υ_g= voltage from generating coil

υ_s= voltage from sensing coil

Acknowledgments

Throughout the course of this research I have had the opportunity to work and interact with wide range of people from different backgrounds. I wish to acknowledge some that have been particularly helpful to me during the entire period of the course.

First of all, I would like to thank to my supervisor, Dr. J.M Gilbert for his guiding and help in my research project. He has given me a lot of guidance as well as many useful ideas to carry out my research. His interest in the work, and his material and intellectual support has sustained the project and me personally, for which I am very grateful. It would be a real tough task for me without his guidance and help. Followed by Dr. A.J. Wilkinson who given me such a valuable chance to work with him. His advice and encouragement as my second supervisor is much appreciated.

My lab mates F. Balouchi and C.K. Yew have provided many important insights and have aided in the direction of the research. I am grateful for their lively discussions, their moral support and friendship which made my time in graduate school a very enjoyable one. I would also like to take this opportunity to thank to all academic and nonacademic staff members in this engineering department for their help and assistances.

I am ever grateful to my parents (T.C. Ooi & K. H. Saw) and other family members for their constant love and confidence in me. Lastly, I would like to thank to my girl friend (G. H Toh) for her loving, supportive, and understanding throughout my university years.

For all the guidance, helps, understanding, supports and encouragements from all the above people, thank you once again.

Chapter 1 : Introduction

Since the last century, energy has been essential in building up modern society. It is required everywhere and can be found from many different places in a different form. According to the Energy Theory, energy will never disappear. Heat, electricity, dynamic, chemical and biomass forms of energy are all stored differently, but they can be converted from one form to the other. Among many types of energy, electricity is the most commonly used form for modern devices [46]. Many researchers have begun investigating methods of obtaining electrical energy from the ambient energy surrounding the electronic device. There are plenty of energies wasting around the device in every single second. For example the energy from a normal range of human activities (walking, jogging, jumping..) , solar energy in the case where the device location is expose to the sufficient sun light and the most interesting energy for this research: ambient vibration energy harvesting. Energy harvesting is the process by which energy is captured and stored. Frequently, this term is applied when speaking about small autonomous devices like wireless sensor network nodes. In typical energy harvesting, up to few miliwatt of power (Power is the rate of using the energy) are captured, accumulated and stored for later use.

In the electronic technology, the vast reduction in size and power consumption of CMOS circuitry has led to a huge research on wireless sensor and communication devices. Furthermore, by removing wires there is the potential for embedding sensors in previously inaccessible locations. Although these electronic devices are very small, they still require power sources such as batteries to operate. These can degrade and would have to be replaced from time to time. This led to the large research effort to seek for alternative portable and long lasting energy sources, especially in applications where the replacement of batteries is unfeasible or costly. For instance wireless sensors used for environmental monitoring, animal tracking and some military application. If self-powered devices are

available, large amount of saving can be made in the power source replacement processes. For example the labour fee to pay for replacing a sensor deeply embedded under a concrete floor.

Recently, plenty of research has been carried out to investigate the methods of converting vibration energy into an electrical form. There are three main methods typically used to for this conversion. They are electromagnetic, electrostatic and lastly piezoelectric conversion. For electromagnetic conversion, a current will be induced in the coil when there is a relative motion between the coil and a magnetic field. The electrostatic generator is formed of two conductors that are separated by a dielectric. Electrical energy will be induced whenever the conductors move relative to each other and this causes the energy stored in the conductors to change. Lastly, for piezoelectric conversion, the strain applied on the piezoelectric material causes a charge separation across the material; this produces an output voltage from the electrodes of the piezoelectric. Each of the mechanism has their own advantages and disadvantages if compared to the others. However in this research, only piezoelectric and electromagnetic will be further discussed.

Recent research has shown that the general output energy density provided by a cantilever beam can be improved by altering the cantilever beam's shape (width). By properly adjusting the beam geometry, the strain on the cantilever beam will distribute more evenly and a higher average strain can be applied on the beam. This has eventually improved the power density of the beam as well as the shifting of the beam's resonant frequency. Apart from varying the cantilever beam's width, this research will discuss on the feasibility of improving the strain distribution by changing the beam's depth (height) of the cantilever beam.

A vibration-based generator will generally produce an optimum output when the system reaches its resonant condition. In this case, the vibration energy generator has to be designed so that it will resonate at a frequency that matches or is somewhere close to an ambient vibration frequency. Therefore, it will be highly desirable if the generator can tune its own resonance frequency to match that of the driving vibrations. The main goal of this research is to investigate and demonstrate a frequency tuning methods for a generator. A novel approach to frequency tuning is proposed and will be demonstrated through simulation and experiment in the later chapters.

1.1 Outline of the thesis

The thesis is laid out in the following manner. Initially, a general overview of energy harvesting is given, discussing some potential ambient energy sources that are suited to energy harvesting purposes. Followed by some discussion on general vibration to electricity conversion model and also the comparison between the three main conversion mechanisms (electromagnetic, electrostatic, and piezoelectric). Although three mechanisms will be introduced, only piezoelectric and electromagnetic conversion will be further considered.

Coming next is Chapter 3, the terminology explanation that is necessary to understand the general piezoelectric and electromagnetic concepts. Some background information including their historical review will be given before the technical information for the vibration-to-electrical conversion. This is followed by a literature review that will cover previous achievements in energy harvesting for piezoelectric and electromagnetic generators, which provides some results obtained by other researchers in both analytical and experimental ways. In particular frequency tuning methods for the harvesting devices will be reviewed.

In order to perform a test on an energy harvesting device, a constant vibration source is required. Therefore, in Chapter 5 the behaviour of the ambient vibration is studied and the obtained information is then converted into a useful form. After this, the converted information is used to generate some replica signals for further use in subsequent simulation and experiments. Some examples from various vibrating sources will be presented and discussed. This is followed by the modelling of the piezoelectric converters by using Matlab in Chapter 6. All the experimental setups will be described. The models will be developed for validation by comparing the analytical and experimental outcomes.

In Chapter 7, investigations of the mechanical strain distribution for five different geometry beam structures will be carried out. The behaviour of the strain distribution on different beams structures will be discussed and the feasibility of improving the strain distribution by changing the cantilever beam's depth (height) will be considered. This chapter will end with the experimental comparison between a triangular and rectangular beam structure.

Last but not least, a load switching frequency tuning method will be introduced. The theory of changing the system resonant frequency by applying a different effective electrical damping at different points during the oscillating cycle will be described as well as the simulation and the experimental setup. Next, the resultant outcomes from the simulation and the experiment will be compared and analysed. Finally some conclusions are presented from the research, along with some discussion of reasonable future research directions.

Chapter 2 : Overview of Energy Harvesting

As mentioned previously, this research will focus on the potential of vibration energy harvesting in applications where vibrations are present. However, in this section, a range of energy sources will be discussed and compared. This is followed by a discussion of the potential source for vibration- based energy harvesting. Last but not least, a simple modelling of the general vibration conversion is presented and the three main conversion mechanisms (electrostatic, electromagnetic, piezoelectric) are discussed and compared.

2.1 Energy sources suitable for scavenging

From previous discussion, it is known that energy does not disappear but is just transformed from one form to another. Therefore, energy is everywhere but in order to capture it a suitable conversion technology must be applied. Electrochemical batteries have been the dominant power source for mobile electronic devices over the past century. However, they provide a finite amount of energy and so need to be replaced for the lifetime of the device. Although these ordinary batteries have improved over the years [24], this improvement is fairly gradual compared with other areas of electronics [62] and cannot satisfy all of the simultaneous demands for long life (up to 20 years), low volume (few mm^3), low weight and limited environmental impact [21].

There are many sources of energy which have been considered for energy harvesting and their lifetime is potentially infinite [2][49][35][53]. For example, solar power, electromagnetic radiation, thermal, human power, wind energy, ambient vibration and the like. Although not all solutions listed here are fit for electronic devices, still it is worthwhile to study scavenging techniques and the possible amount of energy available.

2.1.1 Solar energy (Photovoltaics)

Solar energy is abundant outdoors during the daytime. It is one of the favourite and the main clean energy source and is harvested directly from the sunlight. In a sunny climate, the power density of solar radiation on the earth's surface is roughly 100mW/cm^2 which would be sufficient to power a 100W (take the consideration of the efficiency) light bulb from one square meter of solar panel [51]. Silicon solar cells are a mature technology with efficiencies of single crystal silicon cells ranging from 15% to 20% [47]. Obviously solar energy outdoors during the mid day is the best for energy harvesting if the electronic devices are placed directly under the sun light, yet the disadvantage is that it is only available during the day time and it is climate dependant. On the contrary, indoor lighting has far lower power density than outdoor light. There is a comparison of solar power density measured at varying distances from a 60 watt incandescent bulb by Roundy[49] in Table 2.1 which shows that the indoors power density with office lighting (distance has not given by the author) is not generally appropriate for energy harvesting.

Distance	8 inches	12 inches	18 inches	Office lighting
Power ($\mu W/cm^2$)	503	236	111	7.2

Table 2.1 – Available power density taken under various distance from the energy source

2.1.2 Radio Frequency (RF) electromagnetic radiation

Another energy capturing method is to harvest energy from ambient radio frequency (RF) waves. The designed antenna and the receiver are designed to pick up a wide range of radio frequencies and convert the electromagnetic waves into an electrical current. A prototype has been developed by Nokia Research Laboratory and proved that the harvester was able to scavenge between 3 to 5mW from the ambient radio waves that emitted from mobile antennas, satellite communication, radio, TV masts and other sources

[26]. Moreover, radio frequency signals can be also be used to power many passive electronic devices, such as smart card and radio frequency identification (RFID tags). However, this type of energy is very low at the ambient level. In order for the harvester to obtain a sufficient level of energy to drive an electronic device, many strong signal sources from a wide range of frequencies are required. Apart from that, the antenna and the receiver circuit are required to design and tune to the presented RF signals. In reality the received energy at the receiving end falls rapidly with distance from the energy sources. Therefore, in these ambient conditions, a large broadband antenna is required for the harvesting device or a dedicated source of radio frequency can be used.

2.1.3 Thermal (Temperature gradients)

Naturally, energy can be harvested during the variation of environment temperature. The efficiency of conversion from a thermal source is limited to the Carnot efficiency, which is given as:

$$n = \frac{T_{high} - T_{low}}{T_{high}} \tag{2.1}$$

where T_{high} is the absolute higher temperate on one side and T_{low} is the absolute lower temperate on the other side of the device. So the greater the temperature difference, the greater the efficiency of the energy conversion. It has been proven that the harvested power could eventually result in 15μW/cm^3 from 10˚C temperature gradients by Stordeur [65]. Besides, Zhou[70] investigated the possibility of harvesting energy from a running processor and found that 7mW of power can be obtained from a processor running at 1 GHz using a commercial thermoelectric generator. The maximum conversion efficiency is determined as about 4%. While this is promising, with a better improvement of thermoelectric device, the eventual captured power will be more than that.

2.1.4 Human Power

From various researches, it is known that the human body is a tremendous store house of energy. Starner[63] noted that an average human body burns about 10.5 MJ of energy per day. This is corresponds to an average power dissipation of 121 W. A distinction was made between active human power and passive human power [51]. For active human power, it normally required the user to perform a specific power generating motion. On the other hand, passive human power scavenging occurs during normal activities. Therefore, active human power is not appropriate for most of the applications since it is not a wise method to generate power by performing a specific activity. A significant amount of work has been done on the possibility of scavenging power from the human body for use by wearable electronic devices, such as generating electricity from the compression of the shoe sole. For this device, a generator is mounted in the shoe sole and energy can be captured during normal walking. Paradiso[42] has developed piezoelectric generators in shoes which can produce an average power of 8.3mW at the heel and 1.3mW at the toes during a standard walk. The shoe inserts method offers a good solution for energy scavenging, but the application space for this generation method is extremely limited. Recently, Donelan[16] developed the biomechanical energy harvester which is mounted at the knee and the tested subjects, walking with one device on each leg, produced an average of 5 watts of electricity, which is significantly more than what obtained from shoe-mounted devices. This method seems to be well-suited for charging some portable electronic devices.

2.1.5 Ambient vibrations

Low level mechanical vibrations are present in many environments. From this reason, the potential of converting this mechanical vibrations energy into a useful electrical form is feasible and is abundant enough to be of use. The utility of this type of energy depends on the amplitude of the vibration and its frequency. Vibration sources vary considerably in amplitude and dominant frequency on different objects. Table 2.2 shows the results of measurements on several different vibrations sources performed by various authors. It will be noticed that the fundamental frequency of all sources is between 34 and 200 Hz. Acceleration amplitudes range from 0.1 to 12.3 ms^{-2}. Nevertheless, the vibration present in most environments is not made up of a single frequency but is typically made up of a number of fundamental frequencies and their harmonics. For example the vibration data shown in Figure 2.1, was taken by the author from a desktop computer when a CD was running, indicates a fundamental frequency of 120 Hz with an acceleration amplitude of 0.54 ms^{-2} with the 2nd and higher harmonics present at lower amplitudes. Since most of the vibration-based conversion devices have a relatively narrow range of operating frequencies (high Q-factor), it is important that the nature of the source be understood first so that the generator can be designed to resonate at an appropriate frequency peak in the vibration spectrum.

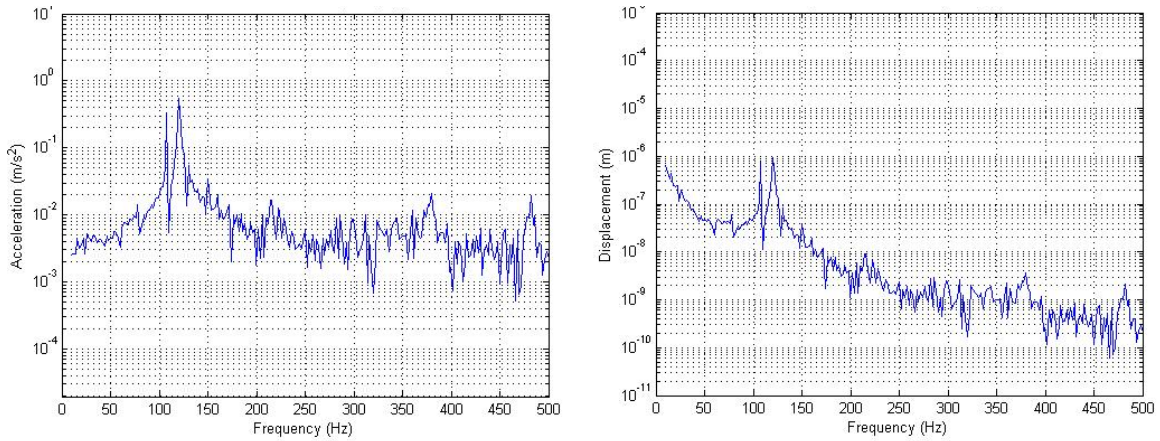

Figure 2.1- Vibration spectra for desktop computer with CD is running

Vibration sources	Acceleration A (m/s^2)	Resonant frequency F_{re} (Hz)	Source of Information
Car engine compartment	12	200	[53]
Second floor of busy office	0.2	100	[53]
Windows next to busy road	0.7	120	[51]
Bread Maker	1.03	121	[51]
Washing Machine	0.5	109	[51]
Blender casing	6.4	121	[51],[53]
Clothes dryer	3.5	121	[51],[53]
Small microwave oven	2.5	121	[51],[53]
HVAC vents	0.2-1.5	60	[51],[53]
Desktop computer casing [On top of the casing]	0.5	120	Author's Experiment
Desktop computer casing (with CD running) [On top of the casing]	0.54	120	Author's Experiment
Standalone fan Heater [On top of the casing)	1.5	34	Author's Experiment
Mobile phone (vibrate mode) [At the back cover when the phone is horizontally]	12.3	170	Author's Experiment
Domestic Freezer [On top of the Freezer]	0.1	50	Author's Experiment

Table 2.2 – Acceleration amplitude and frequency of fundamental vibration mode for various sources

2.1.6 Conclusions regarding energy sources suitable for scavenging

Based on this survey, notice that many energy sources look promising as methods to scavenge power from the environment. However, this research will only focus on energy harvesting from a vibration source. This is not to suggest that vibration-based power sources are the best energy scavenging solution, but only it is one of the most appropriate energy for the self-powered microsystems.

2.2 Modelling of general vibration conversion

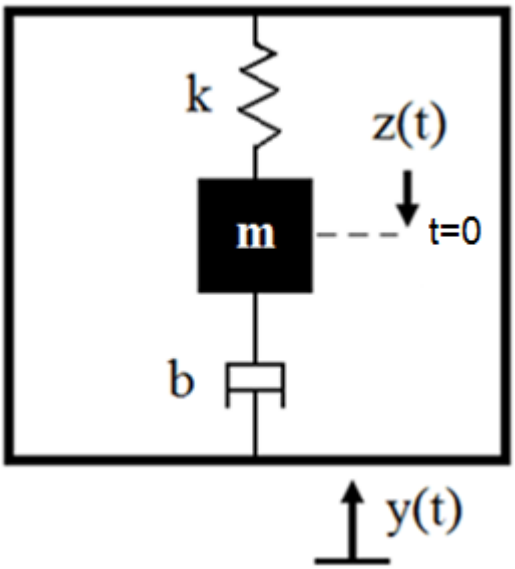

Figure 2.2 - Schematic diagram of a vibration converter

A simple model based on the schematic in Figure 2.2 has been proposed by Williams[68]. The generator consists of a seismic mass, m, on a spring, k. When the generator is vibrated, the mass moves out of phase with the generator housing, so that there is a net movement between the mass and the housing. The dashpot, b, represents the damping coefficient that causes the loss of mechanical energy some of which transforms into electrical energy. This system is described by Equation (2.2).

$$m\ddot{z}(t) + b\dot{z}(t) + kz(t) = -m\ddot{y}(t) \tag{2.2}$$

where z is the spring deflection and y the input displacement

The instantaneous power transfer to the mass, P(t), is the product of the force on the mass and its velocity:

$$P(t) = -m\ddot{y}(t)[\dot{y}(t) + \dot{z}(t)] \tag{2.3}$$

For a sinusoidal excitation vibration, $y(t) = Y\sin(\omega t)$, the total power generated in the damping element is [68]:

$$P_{generated} = \frac{m\xi_T Y^2 (\frac{\omega}{\omega_n})^3 \omega^3}{[1-(\frac{\omega}{\omega_n})^2]^2 + \left[2\xi_T \frac{\omega}{\omega_n}\right]^2} \tag{2.4}$$

where, $\omega_n = \sqrt{k/m}$ is the resonant angular frequency, $\xi_T = b/(2m\omega_n)$ is the total damping ratio, Y is the amplitude of vibration and ω is the angular frequency of vibration. If the spring mass system frequency, ω, is matched with the resonant frequency, ω_n, Equation (2.4) can be simplified to become Equation (2.5) and substituting the acceleration, $A=Y\omega^2$, into this equation yields the absolute power as in Equation (2.6).

$$P_{generated} = \frac{m\omega^3 Y^2}{4{\xi_T}^2} \tag{2.5}$$

$$\left|P_{generated}\right| = \frac{mA^2}{4\omega{\xi_T}^2} \tag{2.6}$$

From Equation (2.6), it can be seen that the power is inversely proportional to frequency. Therefore, if the acceleration amplitude of the vibrations is constant or decreasing with frequency, then the converter should be designed to resonate at the lowest fundamental frequency.

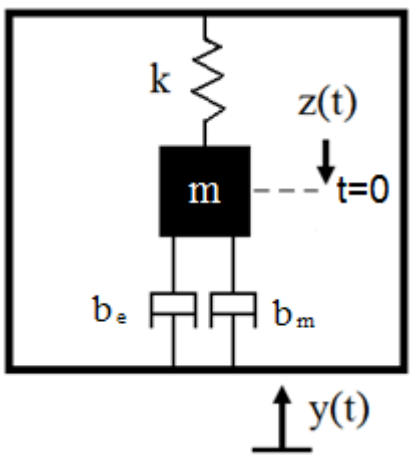

Figure 2.3-Schematic diagram of vibration generator (with electrical damping)

In Figure 2.3 that is the improved model where the damping coefficient of this model is separated into electrical induced damping coefficient, b_e, and mechanical damping coefficient, b_m. Due to the fact that $b=b_e+b_m$, therefore, the power expression for Equation (2.4) and Equation (2.6) can be given as Equation (2.7) and Equation (2.8) respectively. Where ξ_e is the electrical damping ratio.

$$P_{generated} = \frac{m\xi_e Y^2 (\frac{\omega}{\omega_n})^3 \omega^3}{[1-(\frac{\omega}{\omega_n})^2]^2 + \left[2\xi_T \frac{\omega}{\omega_n}\right]^2} \tag{2.7}$$

$$\left|P_{generated}\right| = \frac{m\xi_e A^2}{4\omega {\xi_T}^2} \tag{2.8}$$

The relationship in Equation (2.7) is plotted in Figure 2.4 by assuming that the proof mass, m and acceleration, A, are constant that the resonant frequency is 100Hz and that input vibration frequencies vary from 10 to 1000 Hz. By assuming that $\xi_m = \xi_e$, three different damping ratios (ξ_T) are shown. It can be seen that a generator will provide its optimum output power when the vibration frequency is matched with the system resonant frequency ($\omega = \omega_n$). It may also be noted that increasing the damping, ξ_T has the effect of reducing the peak power but increasing the bandwidth.

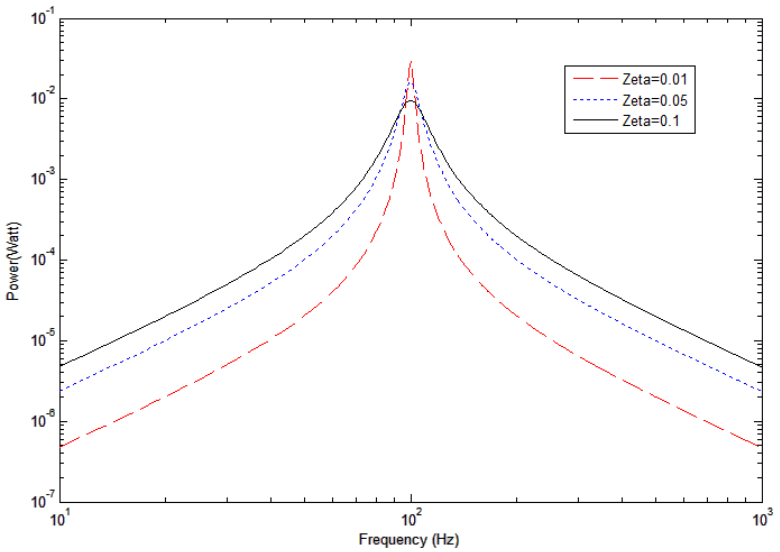

Figure 2.4- Generated power vs vibration frequency of the system

Roundy[51] showed that by using Equation (2.7), some simulation can be carried to investigate on the effect on the generated power of different conditions of electrical damping ratio, ξ_e, and mechanical damping ratio, ξ_m. Figure 2.5 show that the generated power will become optimum when $\xi_e = \xi_m$. However, the generator will perform badly if ξ_m is greater than ξ_e. On the other hand, there is just a small penalty on the case when ξ_e is greater than ξ_m. Therefore, in order to develop a high efficient generator, the designer must always make sure that ξ_m is equal to or smaller than the system ξ_e since most of the damping is electrically induced (attributable to ξ_e).

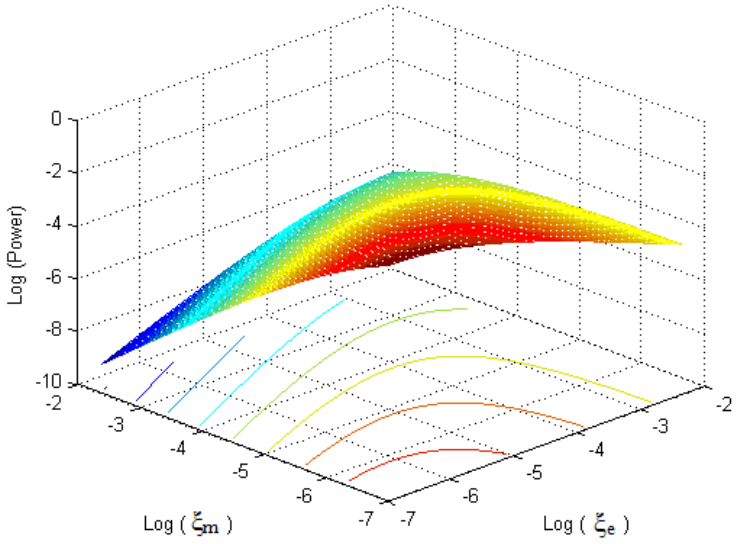

Figure 2.5- Simulation of generated power vs mechanical & electrical damping ratios

Concluding from the discussion above, in order to create a highly efficient generator, the generator should be designed to resonate at the lowest frequency peak in the vibration spectrum provided that higher frequency peaks do not have higher acceleration amplitude. Or more specifically, higher value of A^2/ω. Moreover, the generator needs to be properly designed so that the mechanical damping ratio is smaller than the electrical damping ratio and both of them must be as small as possible (according to Equation (2.8)) to provide a better output at the resonant frequency. Equation (2.8) indicates that the power generated will tends to infinity as ξ_T tends to zero, but in practice it is not possible

to reduce the ξ_m to an arbitrarily small value. This implies that the generated power will always be a finite value and depends on the design of the generator. The amplitude of z is $Z = Y/2\xi_T$ and so reducing the damping factor implies increasing the displacement range of the mass. The maximum movement range of the mass can move is limited by the size and the design of the resonator. Therefore, the damping ratio must be designed to be large enough to keep the range of movement within the limits which the resonator is capable of making without damage. However, from Figure 2.4 it can be seen that the output power can be improved by increasing the electrically induced damping at the point where the driving frequency does not match the resonance frequency. Thus, if the vibration source has a fixed frequency then a low level of damping (high Q-factor) is preferable but if the source frequency varies, it may give better average power to use a higher damping factor (low Q-factor) resonator. On the contrary, one of the main penalty for this solution is the power output is still less than what it would be if the resonance frequency matched the driving frequency.

2.3 Comparing the conversion mechanisms

Practically there are three different ways to convert the vibration energy into the electrical form. They are electrostatic, electromagnetic, and piezoelectric. For an electrostatic generator, it typically involves two plates which are electrically isolated from each other, typically by air, vacuum or an insulator, which move relative to each other. As the conductors move, the energy stored in the capacitor will changes, thus providing the mechanism for mechanical to electrical energy conversion. Secondly, for an electromagnetic converter, energy is generated due to the relative motion between a coil and a magnetic field which will cause current flow in the coil. Lastly, for piezoelectric materials, mechanical strain in the material causes a charge separation across the different layers of the material (which is a dielectric), producing an output voltage.

To illustrate the principle of electrostatic energy conversion, a parallel plate capacitor can be used. The capacitance is approximately:

$$C = \frac{Q}{V} = \varepsilon \frac{A}{d} \tag{2.9}$$

where ε is the dielectric constant of the insulating material between the plates, A is the area of the plates, d is the distance separated between two plates, Q and V are the charge and the voltage on the capacitor respectively. The energy stored in a capacitor with plate charge Q and potential difference V is given by:

$$E = \frac{1}{2} QV = \frac{1}{2} CV^2 = \frac{1}{2} Q^2 C^{-1} \tag{2.10}$$

Changing the stored energy by moving the capacitor plates causes a reaction force and the work done against the electrostatic force between the plates provides the harvested energy. If the separation of a parallel plate capacitor is changed and the charge is held constant, the force can be given as Equation (2.11). While if the voltage is constrained, the force will becomes Equation (2.12) [9].

$$F = \frac{Q^2}{2\varepsilon A} \tag{2.11}$$

$$F = \frac{\varepsilon A V^2}{2d^2} \tag{2.12}$$

There are three types of electrostatic generator classified by Roundy[51], they are In-plane overlap varying in which the overlap area of interdigitated fingers varies; In-plane gap closing in which the separation of interdigitated fingers varies and Out-of-plane gap closing in which the separation of a simple parallel plate capacitor varies in response

to the vibration. There are many researches carried out in recent year for this type of conversion technology. Again Roundy[53] states that in-plane gap closing offers the highest power output with an optimized design producing 100μW/cm^3, out-of-plane gap closing is second highest, followed by the in-plane overlap varying. The maximum power generation occurs for very small dielectric gaps. Meninger[36] have simulated an in-plane overlap varying electrostatic generator based on a comb-driven structure and 8 μW was successfully obtained from 2.5 kHz input vibration motion. Miyazak[39] carried out some investigation on the out-of-plane cantilever-based generator. The device resonated at 45 Hz and tested on a wall with a 1μm displacement up to 100 Hz. 120nW was harvested for the wall acceleration of 0.08 ms^{-2}.

For the electrostatic converter, the primary disadvantage of this kind of converter is that they need an external voltage source during the initiate stage of the conversion process because the capacitor must be charged up to an initial voltage (initial separated voltage) for the conversion process to start. Another disadvantage is that for many design configurations mechanical limit stops must be included to ensure that the capacitor electrodes do not come into contact and short the circuit. The resulting mechanical contact could cause reliability problem as well as increase the amount of mechanical damping and presumable it would removes the initial charge. On the contrary, the great advantage of electrostatic converters is that MEMS (Micro-Electro-Mechanical-System) processing technology offers an effective method to obtain close integration with electronics. Besides, the potential to scale down to much smaller sizes is greater for electrostatic converters.

For electromagnetic converters, there are a couple of significant strengths for this implementation other than its simplicity. First of all, it does not require a separate voltage

source to get the process started as in electrostatic conversion. Secondly, the system can be easily designed without the necessity of mechanical contact between any part, which improves reliability and reduces mechanical damping that would cause a reduction in the output power. However, the disadvantage is that it is not easy to integrate coils into micro-fabrication processes due to its size. In recent years, the practical volume of the electromagnetic generator has been greatly reduced to 0.15 cm^3 but still delivering 30% of the power supplied from the environment [6]. Besides, in order to improve the generated power for this type of generator, a stronger magnetic field can be used to provide more current flow during the motion between the magnet and the coil. Furthermore, by implementing a better conducting material as the coil, this will also improve the output power by reducing the internal resistance and power loss for the system.

Lastly for piezoelectric converters, it requires no separate voltage during the initial stage of the conversion process and is able to generate appropriate voltage directly. Besides, there is generally no need for mechanical limit stops and hence these devices can be designed to exhibit very little mechanical damping. It may be said that piezoelectric converters combine most of the advantages of both electromagnetic and electrostatic converters [41]. On the contrary, the only disadvantage of piezoelectric conversion is the difficulty of implementation on the micro-scale and integration with microelectronics due to its size. However, it is true that a thin film piezoelectric was successfully integrated into MEMS processing but the piezoelectric coupling (efficiency) is greatly reduced [28]. In a study conducted to investigate the feasibility of three different vibration conversion mechanisms, the energy densities provided by these converters were compared. Table 2.3 summarizes the energy density for all three types of converters. However, Roundy[51] seem to restrain their material properties more strictly on both electromagnetic and piezoelectric mechanisms, hence smaller densities were obtained.

Mechanism	Energy Density	Energy Density
	Roundy [51]	Marzencki [33]
Electrostatic	4mJ/cm^3	4mJ/cm^3
Electromagnetic	4mJ/cm^3	24.8mJ/cm^3
Piezoelectric	17.7mJ/cm^3	35.4mJ/cm^3

Table 2.3- Summary of maximum energy density of three types of transducers

Mechanism	Advantages	Disadvantages
Electrostatic	- Easier to integrate in microsystems.	- Separate voltage source needed. - Mechanical stops needed.
Electromagnetic	- No started voltage source needed. - No mechanical stops.	- Output voltage is Low (can be increased by number of turn in the coil but will increase the size of the generator and system loss).
Piezoelectric	- No started voltage source needed. - Output voltage is large - No mechanical stops - High energy density	- Hard to integrate in microsystems and piezo thin films have poor coupling. - The material characteristic and behaviour are more complex and sophisticated. - low output current.

Table 2.4 – Comparison of the three types of converters

The above discussion of the merits and disadvantages of the three different methods of power conversion serves as a basis for narrowing the range of design possibilities before performing detailed analysis, design and optimization. The primary advantages and disadvantages of each type of converter based on those comparisons are summarized in Table 2.4 above. From this table, it can be noticed that piezoelectric converters exhibit all of the advantages of electromagnetic converters while additionally directly providing useful voltages. On the contrary, the behaviour and material characteristic of an electromagnetic converter are less complex and unsophisticated. These also led to the decision that the electromagnetic converter would be used as the conversion

technology in the frequency tuning device investigated in Chapter 8. Though three types of converters have been introduced here, only piezoelectric and electromagnetic converters will be considered in more details in the following chapters.

Chapter 3 : Background information for piezoelectric and electromagnetic harvester

In the previous chapter, a qualitative comparison of electrostatic, piezoelectric and electromagnetic conversion mechanism was presented. However in this chapter, only piezoelectric and electromagnetic will be further discussed. First of all, some terminology of both piezoelectric and electromagnetic will be looked at. This followed by the background information including their historical review and the technical information for the vibration-to-electrical conversion.

3.1 Piezoelectric power conversion

Piezoelectricity is the ability of crystals and certain ceramic materials to generate a voltage in response to applied mechanical stress. Piez*o*electricity was discovered by Pierre Curie and the word is derived from the Greek *piezein*, which means to squeeze or press. The piezoelectric effect is reversible in that piezoelectric crystals, when subjected to an externally applied voltage, can change shape by a small amount. The effect finds useful applications such as the production and detection of sound, generation of high voltages, electronic frequency generation, microbalance, and ultra fine focusing of optical assemblies.

There are twenty natural crystal classes such as tourmaline, quartz, topaz, cane sugar and Rochelle salt which exhibit direct piezoelectricity. Among the crystals, quartz and Rochelle salt exhibited the most piezoelectricity. Apart from that, piezoelectricity can also be observed in ceramics with the perovskite or tungsten–bronze structures ($BaTiO_3$, $KNbO_3$, $LiNbO_3$, $LiTaO_3$, $BiFeO_3$, Na_xWO_3, $Ba_2NaNb_5O_{15}$, $Pb_2KNb_5O_{15}$). Polymer materials like rubber, wool, hair, wood fiber, and silk exhibit piezoelectricity to some extent [59].

3.1.1 Historical review

In the year 1880, during experiments on quartz, the brothers Pierre and Jacques Curie discovered an unusual characteristic of certain type of crystalline minerals. The crystals became electrically polarized when they were subjected to a mechanical force. Tension and compression generated voltages of opposite polarity, and in proportional to the applied force. Subsequently, the converse of this relationship was mathematically deduced from fundamental thermodynamic principles by Lippmann in 1881. If one of these voltage-generating crystals was exposed to an electrical field, it lengthened or shortened according to the polarity of the field, and proportional to the strength of the field. A year later (1882), the Curie brothers verified experimentally this phenomenon by showing that the coefficients for both direct and reverse effects were identical. These behaviours were named the piezoelectric effect and the inverse piezoelectric effect respectively [44].

Added to the above, in 1917 (during World War I), in France, Paul Langevin and his co-workers developed an ultrasonic submarine detector by using a quartz piezoelectric material to generate and detect sound waves in water. The detector consisted of a transducer, made of thin quartz crystals carefully glued between two steel plates, and a hydrophone to detect the returned echo. By emitting a high-frequency chirp from the transducer, and measuring the time taken to hear an echo from the sound waves bouncing off an object, one can calculate the distance to that object. The use of piezoelectricity in sonar, and the success of that project, created intense development interest in piezoelectric devices. Over the next few decades, new piezoelectric materials and new applications for those materials were explored and developed [45].

3.1.2 Piezoelectric vibration-to-electrical conversion

Piezoelectric materials are materials that physically deform in the presence of an electric field, or conversely, produce an electrical charge when mechanically deformed. When mechanical stress is applied on a piezoelectric material, an open circuit voltage (a charge separation) appears across the material. Likewise, if a voltage is put across the material, a mechanical stress develops in the material. These relationships are described by the piezoelectric strain coefficient, d, which gives the relationship between the electric field and stress, while the electro-mechanical coupling coefficient, k_{co}, describes the efficiency with which energy is converted by the material between mechanical and electrical forms. The electro-mechanical coupling coefficient can be functionally related to the piezoelectric strain coefficient by Equation (3.1)[51] which clearly indicate that materials with larger strain and electro-mechanical coupling coefficients have a higher potential for energy conversion.

$$k_{co} = \sqrt{\frac{Y}{\varepsilon}}\, d \tag{3.1}$$

where Y is the material Young's modulus

ε is the dielectric constant of the piezoelectric material

There are two different modes that commonly used in piezoelectric material which are illustrated in Figure 3.1. The x, y, and z axes are labelled as 1,2, and 3 and the material is poled in the 3 direction. The first mode, called 33 mode, in which the stress is applied on the same side as the voltage and the other is called 31 mode, meaning that the voltage acts in the direction 3 and the mechanical stress acts in direction 1. Though the electrical coupling (k_{co}) for mode 31 is lower than mode 33, there is still a key advantage for using mode 31 in energy harvesting. The 31 system is much more compliant, thus larger strains

can be produced with smaller input forces. Besides, the resonant frequency is much lower which will be beneficial to the energy harvesting application.

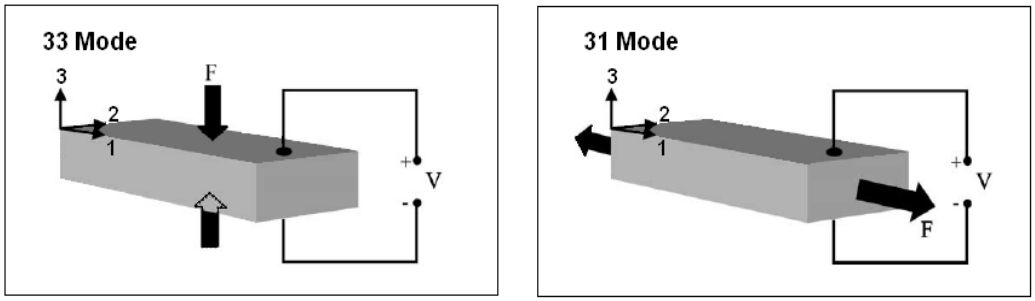

Figure 3.1 a) 33 mode piezoelectric b) 31 mode piezoelectric [51]

The cantilever beam is a commonly used structure for an actuator or generator. The cantilever is able to create relatively large deflections, takes up less space and also resonates at low dominant frequency than in 33 mode. Some of the piezoelectric materials are brittle, so it is very common that manufacturers add stiffness by putting some non-piezoelectric layer attached to the piezo material. The non-piezoelectric layer is used to improve the stiffness of the device while the piezoelectric layer is used to produce the energy. The device is known as a unimorph when one layer of piezoelectric is attached to a non-piezoelectric material. Moreover, when a non-piezoelectric layer is sandwiched between two piezoelectric materials, this device is known as bimorph. These structures are depicted as Figure 3.2.

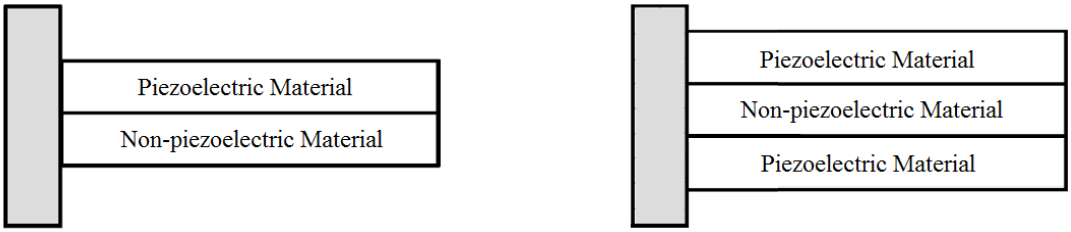

Figure 3.2 a) Unimorph Piezoelectric bender b) Bimorph Piezoelectric bender

For 31 mode piezoelectric materials, the most common type elements are bimorphs as depicted in Figure 3.2(b). As the element bends, one layer is in tension and another is in compression or vice versa. Besides, there are two different ways to connect the layers, Series and Parallel type. The cantilever mounted bimorphs are illustrated in Figure 3.3, which shows the poling and signal fields as well as direction of strain and deflection. For series operation the two plates must be polarized in the same direction with respect to the centre shim (not shown in the figure) either positive or negative. Conversely, for parallel type, the two plates need to be polarized in opposite directions with respect to the centre shim. The electrical connections for the series type are made to the two outer electrodes with no connection to the centre. On the other hand, for the parallel type one connection is required to connect to the centre shim and the other lead to both outer electrodes.

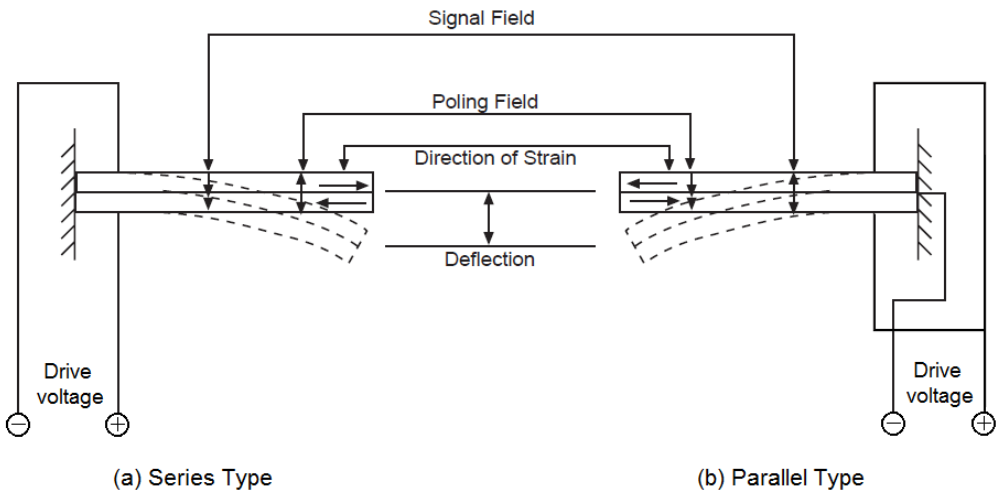

Figure 3.3 – Cantilever mounted bimorphs [40]

Although there is a wide range of materials that exhibit piezoelectric behaviour, PZT (lead zirconate titanate) is probably the most commonly used piezoelectric material in vibration based energy harvesting devices at the current time because of its stiffness and high electro-mechanical coupling coefficient (k_{co}) value. There are several types of PZT available that all have similar but slightly different properties. The specific material used in this entire research is a commonly available PSI-5A4E [43] unless otherwise stated.

3.2 Electromagnetic (induction) power conversion

Electromagnetic induction is the phenomenon of production of an Electromotive force (emf) either by motion of a conductor through a magnetic field in such a manner as to cut across the magnetic flux or by change in the magnetic flux that threads a conductor. If the flux threading a coil is produced by a current in the coil, any change in that current will cause a change in flux, and thus there will be an induced emf while the current is changing. This process is called self-induction. The emf of self-induction is proportional to the rate at which flux is linked as shown in Equation (3.2). The phenomenon of electromagnetic induction has a great many important applications in modern technology especially in the micro-sensors area that has been developed in recent years.

$$|\epsilon| = \left|\frac{d\Phi_B}{dt}\right| \tag{3.2}$$

where:

$|\epsilon|$ is the magnitude of the electromotive force (emf) in volts

Φ_B is the magnetic flux through the circuit

3.2.1 Historical review

Faraday's law was first investigated in 1830-1831 by Michael Faraday. The effect was also discovered by Joseph Henry at about the same time; however Faraday was the first person who published. They discovered that an electric current could be detected from a conductor when the magnetic field around an electromagnet near to the conductor was changing. Apart from that, they found that a current can also be induced by moving a permanent magnet in and out of a coil of wire, or by moving a conductor near a stationary permanent magnet. This led to the discovery of induced electromotive force.

Michael Faraday hypothesized that a changing magnetic field is necessary to induce a current in a nearby circuit. In late 1831, Michael Faraday proposed three laws of electromagnetic induction which are the basic of modern electromagnetic generator nowadays. Those laws are:

1) A changing magnetic field induces an electromagnetic force in a conductor.
2) The electromagnetic force is proportional to the rate of change of the magnetic field.
3) The direction of the induced electromagnetic force depends on the orientation of the field.

3.2.2 Electromagnetic vibration-to-electrical conversion

An Electromagnetic generator is based on the generation of electric current in a conductor located within a magnetic field. Electricity is generated by either the relative movement of the magnet and coil, or due to the changes in the magnetic field. According to William[68], the amount of electrical power generated depends upon the strength of the magnetic field produced by the magnet, relative velocity of magnet (ż) and coil and the practical coil length. The induced open-circuit voltage υ_g can be expressed as:

$$\upsilon_g = k_e \dot{z} \tag{3.3}$$

$$k_e = BL \tag{3.4}$$

where υ_g is the induced open-circuit emf

k_e is the emf constant

B is the magnetic field produced by the magnet

L is the practical coil length

Currently, there are two general designs for vibration-based electromagnetic generators for energy harvesting. The first design involves mounting a group of permanent magnets on a resonating cantilever beam and a coil fixed at the base as shown in Figure

3.4. Conversely for the second design, the group of permanent magnets are fixed at the common base and the copper coil is attached at the end of the cantilever beam as in Figure 8.8 in Chapter 8. Practically, either the magnets or the conductor (coil) can be chosen to be mounted on the cantilever beam while the other remains fixed. For the fixed coil design, it makes the system wiring easier since the conductor is fixed to the common base. On the contrary, for the fixed magnets design, it makes the wiring more difficult while the beam is oscillating. Yet, if a different magnet or multiple magnets is required in the experiment, the fixed magnets design is more appropriate. This is due to the fact that the magnets act as the inertial mass if they are attached on the beam and this will vary the beam's mechanical behaviour for the fixed coil design. On the other hand, for the fixed magnet design, the beam behaviour will remain unchanged even if the initial set of magnets has been replaced with bigger or heavier magnet. Therefore, this concludes that both designs have their pros and cons, also the best design will be the design that suits the applications and objectives the most.

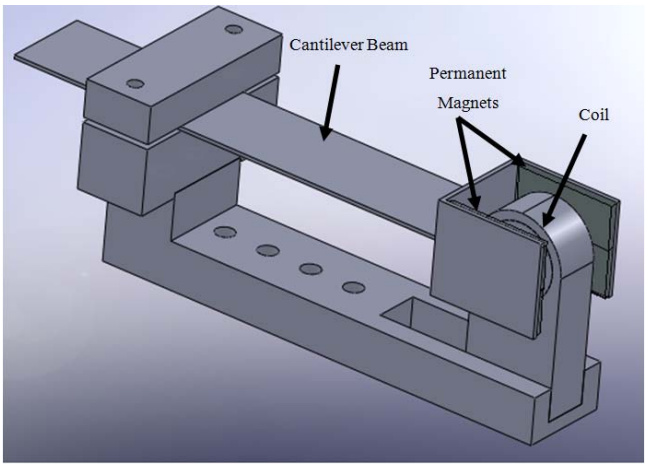

Figure 3.4 – Fixed coil electromagnetic generator

Chapter 4 : Literature Review

For the last decade, vibration-based generators have received increasing levels of attention. Therefore, there has been increasing research effort in the area of power or energy harvesting from vibration. This chapter will review some of the work that has been done previously in this energy scavenging area. It will begin with a look at the piezoelectric based harvester and this will be followed by a review of the electromagnetic based harvester. To end with this chapter, some works and concepts of frequency tuning in energy harvesting devices are discussed.

4.1 Piezoelectric energy harvester

There has been an increasing interest in the investigation of piezoelectric generators in the recent year due to the capability of producing higher output power for a given size than an electromagnetic generator. This section will review some of the work that has been previously done in energy harvesting using piezoelectric material.

There are lots of different applications for the energy harvesting device and also piezoelectric materials can be configured in many different ways that prove useful in power harvesting applications. For example numerous studies involving energy harvesting with piezoelectric material in different disciplines, Starner[63] investigated the possibility of using human daily activities to generate power to run an electronic device. Many possible energy sources have been discussed such as blood pressure, body heat and breathing. Kymissis[27] investigated the use of capturing energy parasitically while walking. They also concluded that magnetic rotary generator can produces 2 orders of magnitude (0.23Watt) more power than either piezoelectric systems they tested (Average power for their PZT & PVDF system are 1.8mW and 1.1mW respectively). However, it is

much harder to integrate smoothly into the design of conventional shoes without interfering with the form factor of the footwear. Besides, a test had been done to prove that by using PVDF stave and PZT unimorph, it was sufficient to power up an active RFID tag by accumulate the energy from several steps.

Moreover research done by Sodano[60][61] comparing several composite actuators for power generation. Three different materials were assessed on their effectiveness in power-harvesting applications. Quick Pack, PZT and MFC (Mico-Fiber Composite) were mounted to a cantilever beam which was tested at 12 different resonant frequencies. The Quick Pack actuator is a bimorph piezoelectric device that uses monolithic piezoceramic material embedded in an epoxy matrix and PZT is the traditionally used monolithic piezoceramic material. Lastly, the MFC actuator is constructed using piezofibers surrounded in an epoxy matrix and covered with an epoxy shell. From the experiment, the MFC performed poorly compared to the Quick Pack and PZT in term of conversion efficiency. It was believed that the poor performance of the MFC is caused by the increased impedance due to the use of interdigitated electrodes in its structure. Additionally, Quick Pack was found to perform very well at resonance but was less effective when excited with a range of frequencies. On the other hand, PZT was shown to be more effective in the random vibration environments that are usually encountered when dealing with ambient vibrations.

Cho[13] analytically optimizing the coupling coefficient in a piezoelectric power harvesting system. The analysis showed that for a given substrate material and thickness an optimum piezoelectric thickness can be found to achieve the maximum coupling coefficient that can be obtained. The coverage of the electrode was found to be important to the electromechanical coupling. Their model predicted that the coupling coefficient increases with the electrode size and reaches its maximum when the electrode covers 42%

of the membrane area. Later on, they further investigate the same idea and found that electrode coverage about 60% produces the optimum coupling and application of a dc bias also leads to an increase in coupling [14].

Jiang [25] also investigated methods of increasing the efficiency of a piezoelectric bimorph. They analyzed the performance of a piezoelectric bimorph in the flexural mode for scavenging ambient vibration and determined the relationship between performance and physical and geometrical parameters. They had shown that by reducing the thickness of the bimorph and the centre shim, or increase the proof mass at the end of the cantilever, the resonant frequency of the system will substantially decreased. The maximum power harvested was shown to be greater for lower a resonant frequency described in Equation (2.6).

Mateu[34] proposed an analytical comparison between a rectangular and triangular shaped cantilever. It was proven mathematically that a triangular cantilever with the same beam volume as a rectangular beam will have a higher average strain and maximum deflection for a given load. Therefore, they concluded that a triangular cantilever beam will produce more power per unit volume than a normal rectangular beam. At almost the same time, Roundy[52] proposed that with an increasingly trapezoidal (a transformation process from a rectangular to a triangular geometry) shaped cantilever, the strain will be distributed more evenly. He also stated that a trapezoidal cantilever can generate more than twice the energy than a rectangular beam provided the volumes of both cantilevers are equal. He also concluded that by changing the configuration of the cantilever, the cost and the size of the generation can be reduced significantly by using less material but still satisfying the given power requirement. More details about the alternative beam structure will be discussed in Chapter 7.

Minazara[38] focused on the development of piezoelectric generators to convert mechanical power to electrical power from vibrations in dynamic environment. The experimental setup used is shown in Figure 4.1. The membrane transducer is rigidly fixed on the piezoelectric actuator. The mechanical vibration force (F) which causes an oscillating motion of the macroscopic 25mm diameter piezoelectric membrane, resulting in strain on the piezoelectric layer and generating a low-frequency voltage signal. Their experimental results shown that 1.7mW power was generated at the resonance frequency of 1.71kHz across a 47kΩ optimal resistor and for a 80 N force.

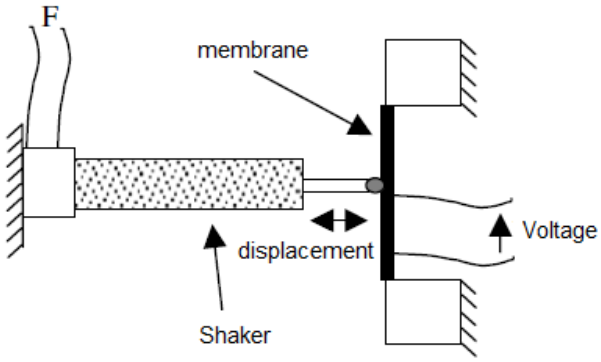

Figure 4.1- Experimental setup of a membrane transducer [38]

Leland[30] carried out an exercise to verify the feasibility of powering an electronic device in a real-world deployment situation. They successfully produced 30μW from the vibration generated by a wooden staircase at 27 Hz. The piezoelectric generator which was mounted on the staircase used a piezoelectric bimorph to generate the electrical energy which was sufficiently to power a temperature sensor and radio hardware. The prototype required 50 minutes of continuous staircase foot traffic from two people to take and transmit a set of two temperature readings.

Shen[58] presented a MEMS PZT energy harvesting cantilever device with an integrated Si (Silicon) proof mass for low frequency (hundreds of hertz) and high amplitude (>1g) vibration applications. The piezoelectric cantilever device in this research

consists of multi-layers films deposited on a Si substrate as in Figure 4.2. The Si is used as the proof mass at the tip to reduce the resonant frequency and to improve the beam's mechanical strength. The silicon oxide (SiO_2) is used as the insulator between the electrode and Si. The interlayer titanium (Ti) is used to improve the adhesion between the PZT and platinum (Pt). The top and bottom layer of Pt are used as the electrodes. The prototype successfully produced 2.15μW with an optimal load of 6kΩ from 2g acceleration at its resonant frequency of 461.15Hz. The effective volume (beam plus the proof mass) is about 0.6520mm^3.

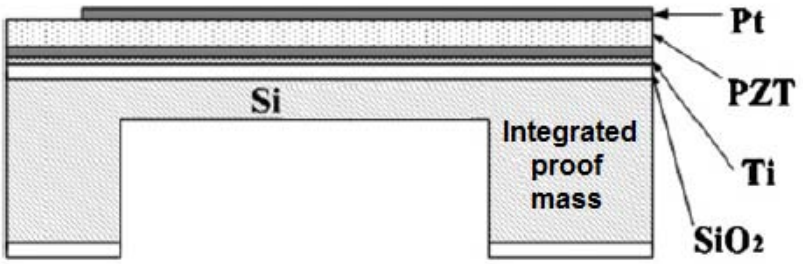

Figure 4.2- Side view of a piezoelectric energy harvesting cantilever [58]

It has been reported that common environmental vibrations such as those found in a building exhibit at lower frequencies (50-200 Hz) [53]. Therefore a year later, the multi-layers cantilever design was further improved by the some author using an SOI (silicon on insulator) structure [57]. With the use of a layered silicon-insulator-silicon substrate as depicted in Figure 4.3, the whole structure becomes more flat and the cantilever exhibited a much smaller curvature as preferred. Apart from is, the SiO_2 layer in the SOI wafer can be used to precisely control the thickness of the silicon supporting layer in the cantilever beam. Therefore, the resonant frequency for the beam can be easily altered. The average power was measured as 0.32μW across the optimum load of 16kΩ when the cantilever was excited at 0.75g acceleration amplitude at its resonant frequency of 183.8Hz. The effective beam plus mass volume for this generator was reported as 0.7690mm^3.

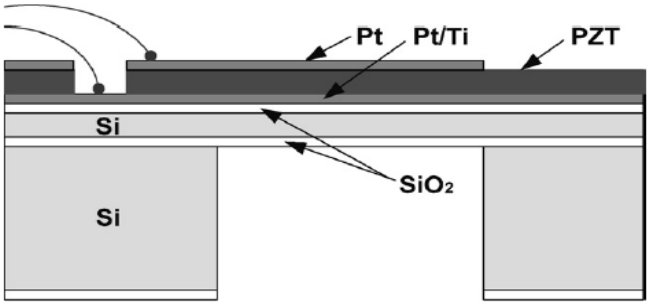

Figure 4.3- Side view of piezoelectric energy harvesting cantilever [57]

4.2 Electromagnetic energy harvester

Apart from the piezoelectric generator, an electromagnetic energy converter is another vastly investigated topic for researchers in recently years. Williams [68] proposed a device, which generated electricity when embedded in a vibrating environment. For their investigation, an electromagnetic transducer was chosen. The microgenerator has dimensions of around 5×5×1mm and the power generation of 1μW at an excitation frequency of 70 Hz and 0.1mW at 330 Hz (assuming a deflection of 50μm). It was also determined that a low damping factor was required to maximize power generation.

A few years later, El-hami[18] carried out some simulation and modelling of a electromagnetic transducer based on the relative movement of a magnet pole with respect to a coil. Their demonstration also proved that the generation of practical amounts of power within a reasonable space is possible. Power generation of more than 1mW within a volume of 240 mm^3 at a vibration frequency of 320Hz has been obtained. Following the work, Glynne-Jone [22] assessed two prototypes based on cantilever structures, but having different combinations of magnets and coils structure. The first prototypes based on the moving coil between two fixed magnets and the second prototypes based on moving two magnets with fixed coil (improving the magnetic coupling between the magnets and the coil). The first prototype generated power levels up to 180 μW (with 0.85 mm

displacement) and the second prototype generated more than four times higher power than the first one.

Beeby[8] developed a silicon-based generator that consisted of a silicon paddle beam, four magnets and a wire-wound coil. The design is shown in Figure 4.4. Two magnets are located within etched recesses in the Pyrex wafers and two Pyrex wafers are bonded to each face of the silicon wafer. The bonding process is aligned to ensure correct placement of the coil relative to the magnets. The coil is located on a silicon cantilevered paddle designed to vibrate laterally in the plane of the wafer. In the same year, Beeby[7] carried out finite element analysis using ANSYS to determine the resonance frequency and the material stress. They found that levels of 4 to 9V can be achieved from a single beam generator design in their simulation and emphasise the importance of reducing unwanted loss mechanisms such as air damping in order to improve the generator performance. Under normal atmospheric pressure, they experimentally showed that this device has a resonant frequency of 9.5 kHz and generated 0.5 μW into a matched load at 9.81 ms^{-2}.

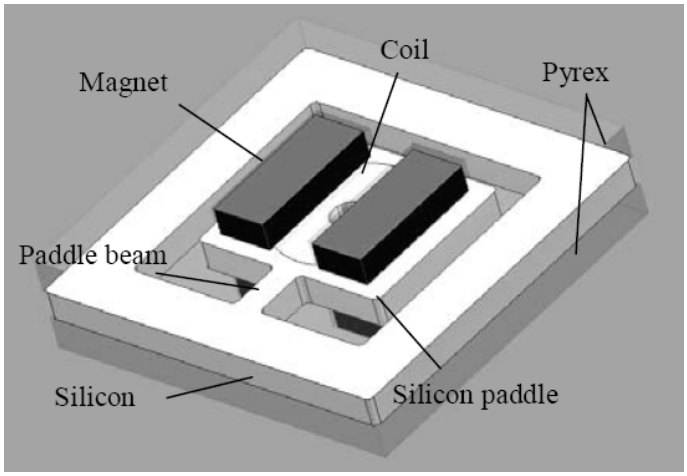

Figure 4.4- Micromachined Silicon generator design [8]

A few years later, a micro electromagnetic generator with a practical volume of $0.15cm^3$ was presented by Beeby[6] as in Figure 4.5. This generator uses four high density energy density sintered rare earth neodymium iron boron (NdFeB) magnets arranged on an etched cantilever with a wound coil located within the moving magnetic field. A Zintec keeper was used to concentrate the flux gradient through the copper coil during the oscillation. A double polished wafer with thickness of 50μm was selected as the cantilever beam to give resonant frequencies between 50-60 Hz. The beam was clamped onto the high performance plastic base (Tecatron GF40) using a steel washer. From their experiment, it was reported that the final device was able to produce 46μW from just 0.59 ms^{-2} acceleration levels at its resonant frequency of 52Hz across the 4kΩ optimum resistance.

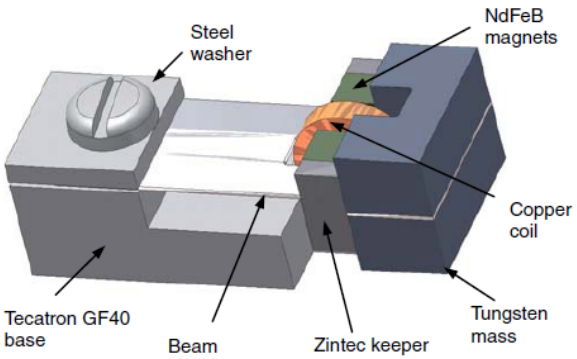

Figure 4.5 – A micro cantilever generator [6]

Wang[67] presented an electromagnetic energy harvester that consists of an electroplated copper planar spring, a permanent magnet and a copper planar coil with high aspect ratio, as depicted in Figure 4.6. Their electromagnetic simulation indicated that the peak to peak open circuit voltage of the optimized structure is 42.6mV and the maximal output power is 0.7 μW. On the other hand, their prototype testing result shows that the prototype could only generated an open circuit voltage of 18mV and output power of 0.61 μW. However the prototype model tested was not in an optimized structure. Therefore,

they believed that by further optimizing the dimensions of the permanent magnet, the output voltage and power could be improved.

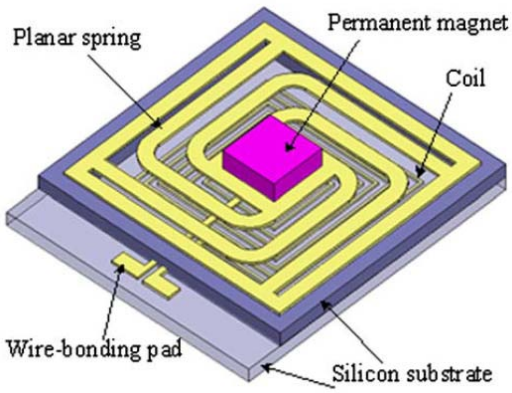

Figure 4.6 – Schematic structure of electromagnetic generator [67]

Added to the above, Bedekar [5] had successfully developed a pulse rate sensor with a vibration energy harvester integrated inside a pen to capture energy from normal human activities. An electromagnetic energy harvesting was selected in order to achieve high power at lower frequencies. The fabricated pen harvester prototype (placed in the test subject's pocket) was connected across an optimum load of 22Ω and was found to generate a constant 3.7μW, 0.46mW and 0.66mW under regular walking, jumping and jogging respectively. Although the power generated under regular walking from the test subject was very low, the prototype was found able to generate a continuous power of 0.46-0.66mW (during jumping and jogging) which was enough to power a small scale pulse rate sensor.

4.3 Frequency tuning in energy harvesting devices

Practically, as the frequency of ambient vibrations typically varies over time, it is not possible to guarantee that a fixed frequency generator will always work at resonance and produce the maximum output power. Therefore, research on frequency tuning has been carried out to overcome this problem.

Agah[1] investigates the effect of the natural frequency of a piezo element when the physical structure or the internal material properties were changed. They predicted that the output power of the system is maximized when the mechanical damping in the system is minimized. A three-beam microgenerator, which exhibit natural resonance frequencies of 400Hz, 800Hz and 1500Hz, was tested. This generator is proposed to cover a wider range of frequencies and proved that for an operating frequency of 400Hz, power of 1-5μW can be delivered to the output. They also suggested that to reduce the mechanical damping in order to maximize the power efficiency, it may require to operate the device in a vacuum-sealed package. Then the damping ratio can be easily controlled by the air pressure inside the package.

Shahruz [55] later used the multiple beams method to design a mechanical band-pass filter for use in energy scavenging. The filter contains an ensemble of multi cantilever beams. Some beams come with proof masses at their ends but some were left free. By appropriately choosing the length of the beams and the size of the mass, a wide frequency band can be harvested and is not limited to just one. Figure 4.7 show the ensemble of cantilever beams with proof masses at theirs tips and the Bode magnitude plots from the band-pass filter. However, it proved hard to determine the dimension and the proof mass value of the cantilevers in order to get the best possible performance from the filter. Therefore, the author proposed a method called the “limits of performance” to optimize the mechanical filter. The knowledge of such limits leads to a systematic procedure for determining dimensions of the beams and masses of the proof masses of band-pass filters with best possible performance [56]. The main disadvantages for multi cantilever beams system is that the power density will go down as the number of beams goes up. This is due to the power from the multiple cantilevers must be effectively combined and if there is any

of the beams has lower output power, the total output power density of the system will be affected.

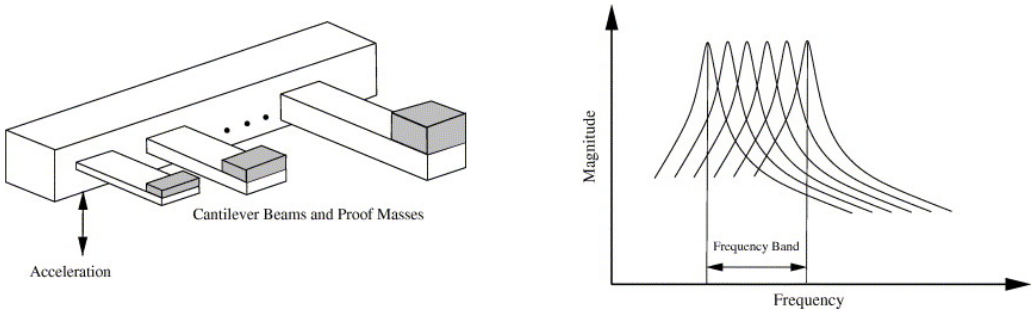

Figure 4.7 - An ensemble of cantilever beams and the Bode magnitude plots [55]

A year after, Liu[31] investigated a micro-power generator array utilizing PZT film as the transducer to harvest ambient low-level vibration. The generator was successfully fabricated by the MEMS process. The generator produced 3.98 μW of effective electrical power and 3.93 DC output voltage from the multi AC-DC rectification. Theirs concepts is depicted as Figure 4.8. Their experiment showed that the arrayed device is promising in improving operation bandwidth and power output of the generator.

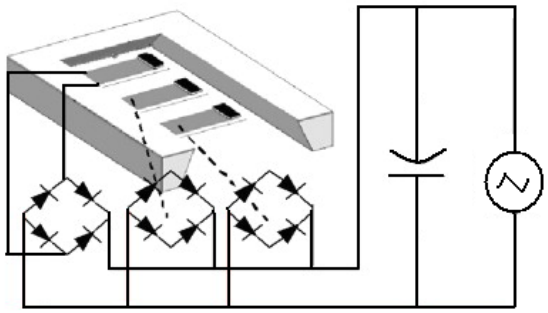

Figure 4.8 – Electrical connection of piezoelectric power generator [31]

The same multiple beams concept may be applied to electromagnetic generators as well as piezoelectric devices. Sari[54] have reported an electromagnetic generator that consists of an array of cantilevers with varying lengths and resonance frequencies to solve the bandwidth problem. By carefully adjusting the length of the cantilevers, those cantilevers will have an overlapping frequency spectrum with the peak powers at close but

different frequencies. The proposed multi cantilever generator and the resultant frequency response are shown as Figure 4.9. By utilizing 35 cantilevers, this fabricated device can generates 10 mV voltage and 0.4 µW power continuously within a frequency band of 800 Hz (4.2-5 kHz). Besides the generated output, they found that by using Parylene as the structural material, larger deflection are allowed before mechanical failure compare to silicon. Thus, larger power can be obtained.

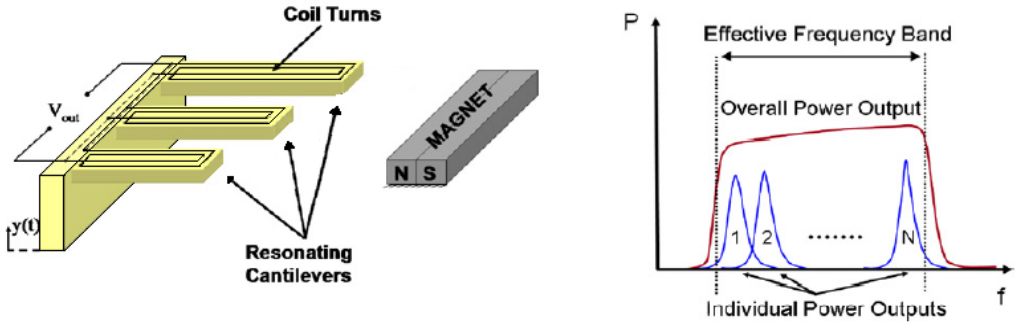

Figure 4.9 – Proposed electromagnetic generators and the resultant frequency response [54]

Bin [11] proposed another type of multi-frequency energy harvester which consists of three permanent magnets, three sets of two-layer copper coils and a supported beam of acrylic. These coils were made of thin fire resistant (FR4) substrates using a standard printed circuit board (PCB) as shown in Figure 4.10. They noted that PCB with multiple Cu coils could easily be fabricated at much lower cost than piezo cantilevers. Therefore, this method not only provides multiple frequency generation but also a less expensive energy converter. The energy under the first, second and third resonant modes can be harvested, corresponding to resonant frequencies of 369 Hz, 938Hz and 1184Hz respectively. A total output power of 1.157 µW can be obtained when three sets of coils are connected in series in the case of 14 µm exciting vibration amplitude and 0.4 mm gap between the magnet and the coils. The generated power is not an outstanding one compared to the others multi frequency generator, but the major advantage of this device is low cost and capability of capturing a range of different vibration frequencies.

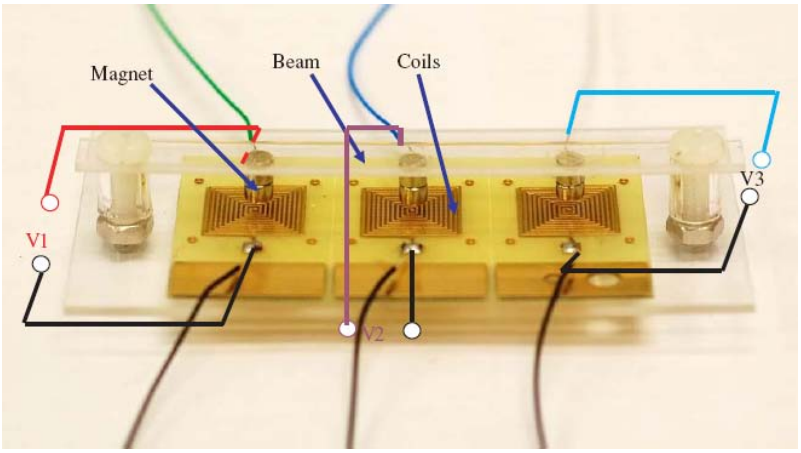

Figure 4.10 – Multiple frequency generator design[11]

Qi [46] demonstrated a new form of multiple cantilever beam structure as shown in Figure 4.11. All the side mounted cantilevers were designed with different tip masses and beam lengths which created many resonant frequencies. During the excitation, the central clamped-clamped beam will accelerate equally at both of its clamped ends and the strains will be produced at every side cantilevers at their own resonant frequencies. All the strains were then summated within the clamped-clamped beam and converted to an electrical energy by the central piezoelectric fibre composite (PFC). The prototype was reported to produce 18 V pk-pk and 0.01mA pk-pk respectively when both of the clamped supports are subjected to an excitation level of 10.47ms^{-2} pk-pk. It was noted that this was higher than it would be met in practice but this was used to ensure the maximum output. However, the driving frequency for this data was not reported. Added to the above, they claimed that this multiple side mounted generator can produce a better output power than a generator which comprising several individual piezo cantilevers because of the out-of-phase effect from multi individual piezo cantilevers can be simply avoided. Apart from the output power, this generator was believed to be more cost effective than an ordinary array cantilever generator.

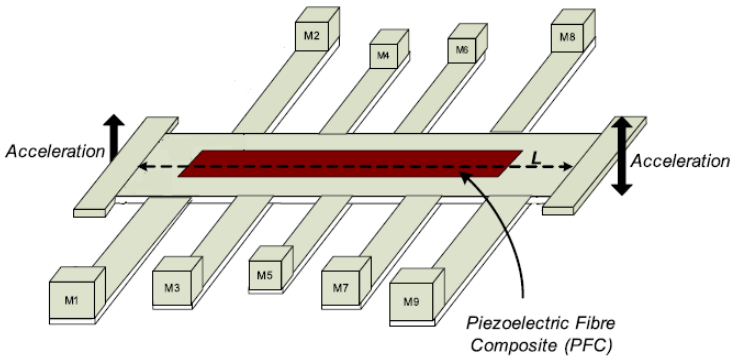

Figure 4.11- Clamped-clamped beam with multiple side mounted cantilever [46]

Cottone[15] proposed a new method based on the exploitation of the dynamical features of stochastic nonlinear oscillators. In this method, consider two permanent magnets with opposite polarities, respectively on the cantilever tip and on an external fixed support at a distance Δ along the beam axis. A repulsive force acts between the two magnets which decrease in magnitude with increased distance Δ. Under the action of the excitation and when the external magnet is far away, the cantilever beam behaves like a linear oscillator whose dynamics are resonant with a resonance frequency determined by the system parameters. On the contrary, when Δ is small enough, the cantilever beam can show two different types of behaviours as a function of the distance of Δ and the cantilever bounces between two stable states. This similar idea was then used by Ferrari [20] as in Figure 4.12, where x and V_p represents the vertical displacement of the mass and the generated voltage respectively during the excitation. Their experimental results showed a good agreement with their simulation analyses. The experimental outcomes showed that the nonlinear bistable case can provides a spectrum with a wider bandwidth compare to the resonant behaviour of the linear case and so is expected to produce an improved effectiveness in converting wide-spectrum vibration, especially at frequencies below the initial resonance. Figure 4.13 shown the experimental frequency amplitude spectra of the output voltage V_p measured from different values of the distance Δ (legend in Figure 4.13) under an acceleration of 0.3g ($1g=9.81ms^{-2}$). The experimental results

showed the reducing of resonant frequency of the system with the reduced distance between the magnets Δ, as long as the system maintains the linear oscillation behaviour. On the other hand, when the distance Δ reduces to a lower value, a bistable system wi ll be created and bouncing between two stable states can occur. In this condition, the cantilever converter will produces a marked improvement in the output voltage over a wider bandwidth with respect to the linear behaviour.

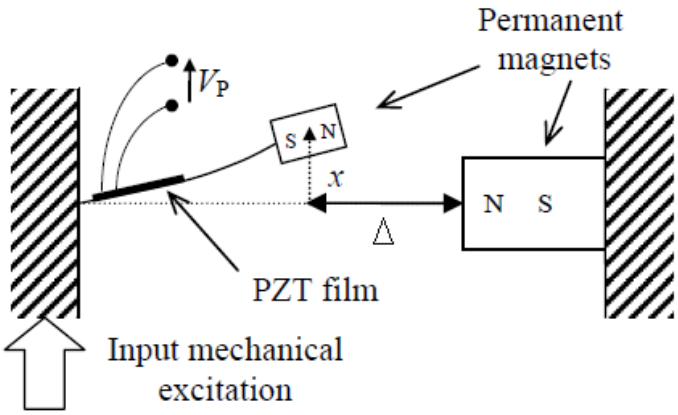

Figure 4.12 – Setup for a nonlinear generator [20]

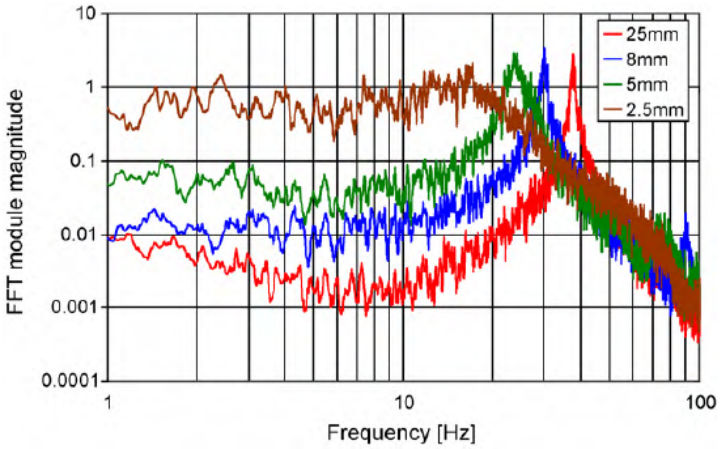

Figure 4.13- Frequency amplitude spectra of the output voltage Vp [20]

After an increasing amount of research on frequency tuning generators, Roundy[50] started to examined the possibility of ‘actively’ tuning a device’s resonance characteristics and presented a design that used electrical feedback to alter the resonance frequency of a piezoelectric bimorph. Apart from that, a distinction was made between ‘active’ tuning

actuators that must continuously supply power to alter the system resonance frequency, and ‘passive’ tuning actuators that supply power initially to tune the frequency, and they are able to ‘turn off’ while maintaining the new resonance frequency. An “active” tuneable piezoelectric bending generator was built and their experimental data suggested that “passive” tuning generators are better than the “active” tuning generator because the latter will never result in a net increase in electrical power output. However, recently Zhu [72] had claimed that this conclusion was not correct. They stated that only the situation where the tuning force is proportional to the generator’s displacement or acceleration was studied in [50], but for most cases the tuning force is not linked to the generator’s movement and methods of calculating actuation power may be different. Therefore, they claimed that the analysis made by Roundy[50] should not apply to all situations. Yet, they agree to that “passive” tuning mechanism has an advantage over an “active” tuning mechanism in term of energy consumption at the points when the device was already resonating at the ambient frequency. However, this still depend on how often the ambient vibration frequency changes. If the vibration frequency of the environment changes periodically, a “passive” tuning will become practically unfeasible due to its inflexibility. On the contrary, an “active” tuning will be more appropriate in this situation. Therefore, it can be concluded that the suitability of different tuning approaches will depend upon the application and there will be no party that should be considered better or worse than the other.

The idea of this “smart scavenger” was then implemented by Wu [69]. A real-time resonant frequency tuning system was presented by using a microcontroller to sample the external frequency and adjust the variable capacitive load to shift the gain curve of the cantilever beam so that the system natural frequency will matched with the external vibration frequency in real-time (active tuning) as depicted in Figure 4.14. The upper

panel of the bimorph was used in the frequency tuning purpose and the lower panel on the beam is then used to harvest energy and generate a dc voltage to the electronic device.

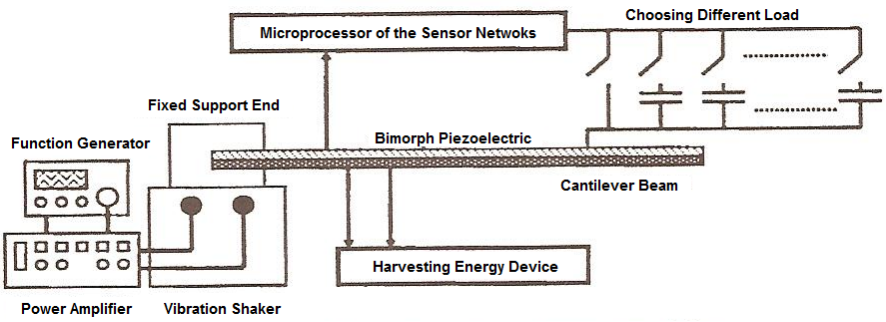

Figure 4.14 – Power Harvesting Device Experimental Setup [69]

Roundy[48] investigated the self and adaptive-tuning energy generator. They modelled a beam as a simply supported beam with a proof mass in the middle and the beam's stiffness is a function of the axial compressive preload. The preload can be easily applied by set of screws that push on the clamps at either end of the beam. They successfully reduced the resonance frequency by approximately 40% by using a preload equal to half of the critical buckling load. However, no output power was reported by this author. The structure of their model is depicted in Figure 4.15.

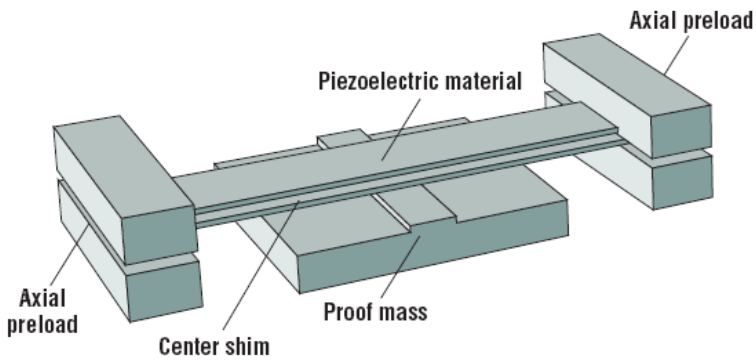

Figure 4.15- A Supported piezoelectric beam scavenger with an axial preload [48]

Leland [29] later used this method to adjust the natural frequency of an energy harvester. A simply supported piezoelectric bimorph was used to evaluate harvester

performance. They determined that an axial pre-load can lower the resonance frequency by up to 24% and the coupling coefficient can be increased by up to 25%. Prototypes were developed that produced 300-400μW of power at an acceleration of 9.8 ms^{-2} and the operating range was from 200 to 250 Hz. The piezoelectric bimorph had dimensions of 31.7mm×12.7mm×0.509mm and the weight of the proof mass was 7.1g. They concluded that by using this method, a harvesting device can be tuned across a bandwidth of frequencies.

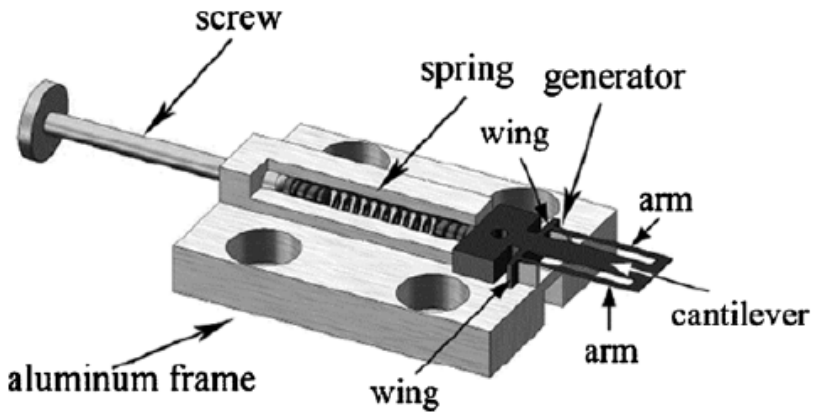

Figure 4.16- Schematic diagram of the test device designed [17]

This axial preload principle was further developed by Eichhom [17] as in Figure 4.16. This design consists of a piezo-polymer cantilever beam with arms on both sides to enable the application of an axial force (compressive or tensile) to the free end of the beam. The tuning force was applied by a screw and a steel spring. Their resultant data showed that by applying a compressive axial preload, a frequency shift of 22% (380 to 292Hz) was reached while a tensile preload led to a frequency shift of about 4% (440 to 460Hz). Apart from that, their experimental outcomes also indicated that for the compressive load, the quality factor (Q-factor) decreases, which indicates a higher damping coefficient. On the other hand, the quality factor was augmented slightly by applying a tensile load to the tip of the beam.

Another way to tune the resonance frequency of the piezoelectric beam has been proposed by Challa[12]. By using the magnetic force from a permanent magnet, the effective stiffness of the beam can be tuned. Four permanent magnets are used: instead of placing the magnets axially to each other, two magnets are fixed at the free end of the cantilever beam, while the other two magnets are fixed to the enclosure of the device at the top and bottom, vertically aligned with the magnets on the beam as depicted in Figure 4.17. Those magnets were placed such that attractive and repulsive magnetic forces can be applied on each side of the beam. The cantilever beam was fixed on a clamp that can be vertically displaced using a screw-spring mechanism so that the distance between the magnets can be controlled to alter the magnetic force that exists between the magnets on the beam and the enclosure. Approximately 240-280 μW was generated over the frequencies between 22-32 Hz for this experiment at 0.8 ms^{-2} acceleration.

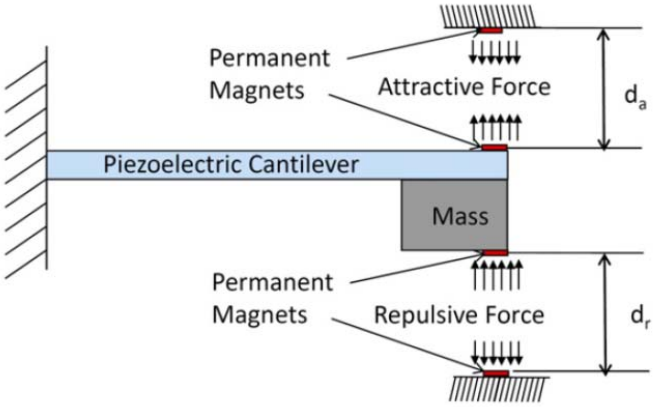

Figure 4.17 –Resonance tunable energy harvesting device [12]

Another magnetic force tuning method of applying an axial load to a cantilever-based generator was reported by Zhu[71] who presented a tunable electromagnetic vibration-based generator with closed loop frequency tuning. The frequency tuning was realized by applying an axial tensile magnetic force to the micro-generator as in Figure 4.18. The tuning force was provided by the attractive force between those tuning magnets

with opposite poles facing each other. The magnet attached on the linear actuator can be adjusted and placed axially in line with the cantilever so that the axial force acting on the cantilever can be altered. Experimentally the resonant frequency had been successfully tuned from 67.6 to 98 Hz by changing the distance between two tuning magnets from 5 to 1.2mm respectively. The generator produced a power of 61.6 to 156.6μW over the tuning range when it was excited at constant vibration acceleration level of 0.588 ms^{-2}.

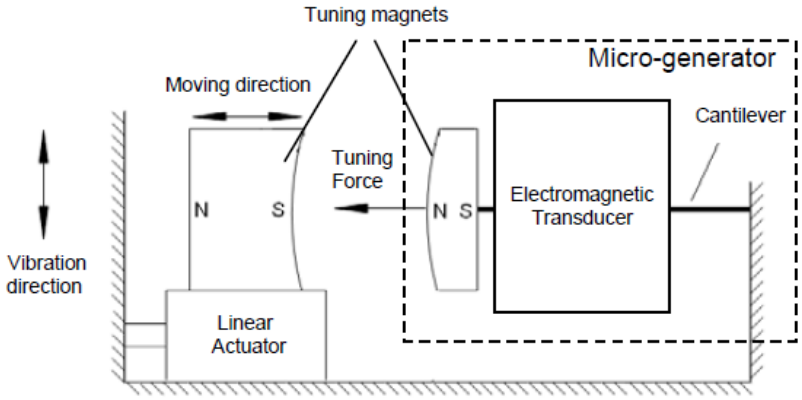

Figure 4.18- Schematic diagram of the tuning mechanism [71]

A similar frequency tuning approach was implemented by Mansour [32]. However, their harvester utilized piezoelectric instead of electromagnetic energy transduction. As in Figure 4.19, a cantilever beam provided with a top piezoelectric (PVDF) sheet is mounted on a shaker. The beam carries a tip mass in the form of a permanent magnet placed in a holder which is attached to the beam tip. An opposite magnet is firmly attached to the common base and is allowed to traverse axially using a screw to alter the tensile force applied to the beam. By altering the stiffening effect of the attractive magnetic forces provided by the interaction of a tip magnet and the adjacent magnet fixed on the common base, this generator was reported that able to tune the fundamental natural frequency from 3.19 to 12 Hz. Nevertheless, their experimental results also reported that the tuning range comes at the expense of reduced output voltage for higher magnetic tensile force.

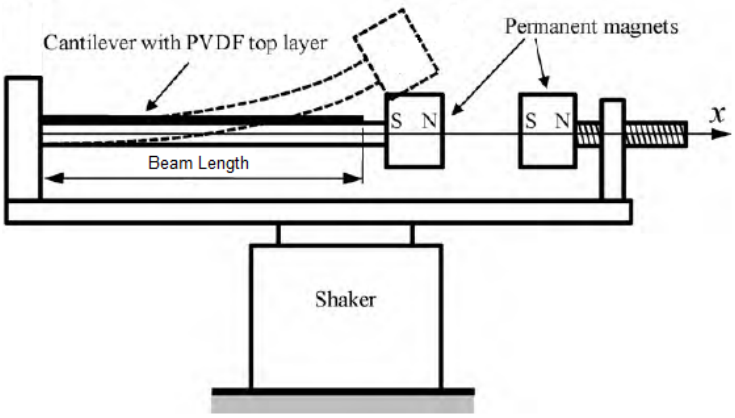

Figure 4.19- Schematic of the resonator proposed by Mansour [32]

From the above discussion, all the tuning methods can be categorised as in the "tree" structure proposed in Figure 4.20. It can be seen that there are typically two possible solutions to match the generators resonance to the ambient vibration. The first solution is widening the generator's bandwidth. This solution can be further categorising into two approaches: Multiple Generators and Nonlinear Generators. Multiple generators involves the designing of a generator consisting of an array of elements each of which resonates at a different frequency [1][11][31][46][54][55][56]. The nonlinear generators, involves the design of a generator having a nonlinear behaviour during the excitation [15][20]. On the other hand, the second solution is to tune the resonant frequency of the generator so that it matches the frequency of the ambient vibration. This approach consists of an active tuning (Active Generator) that is defined as a tuning mechanism that is continuously applied even if the resonant frequency equals the ambient vibration frequency and a passive tuning (Passive Generator) that is defined as a tuning mechanism that operates periodically. The active tuning consists of Capacitive Tuning which involves tuning the resonant frequency by altering the capacitive load of the system [69]. This is followed by a novel load switching method proposed by this research author. More information regarding the load switching tuning will be further described in the later chapter. On the other hand, there are two tuning methods available for passive tuning in

this review, which are named as Mechanical Tuning and Magnetic Tuning. The earlier approach involves pre-stressing the cantilever and axial preload beam using a mechanical force [17][48]. Similarly for the latter approach, it involves applying stress to the generator beam, however magnetic force will be used instead for this approach [12][32][71]. Although there may be other methods which also perform the frequency altering effect, in order to avoid confusion, only those methods that fit into this categorisation were included.

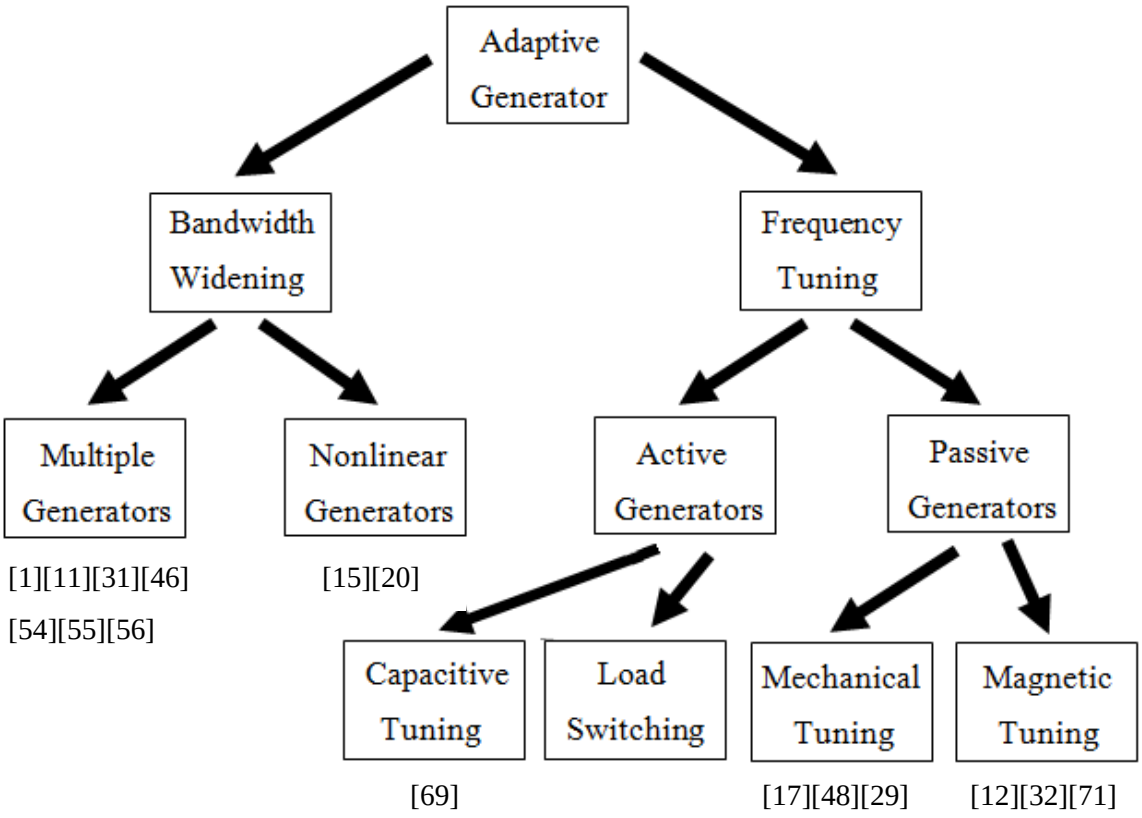

Figure 4.20 - Tree structure for frequency tuning methods

Chapter 5 : Generation and capture of a vibration sources

This chapter presents two different methods for capturing vibration sources from varies objects using an accelerometer. The captured signal will then be converted into a frequency spectrum for better illustration. After the capturing section, this chapter discusses a method to generate a vibration signal to the vibrator through an amplifier so that a reliable vibration signal can be used for subsequent experiments. The main objective for this chapter is to illustrate the behaviour of the ambient vibration and also demonstrate a suitable ways to convert the vibration signal into a useful information form. This information is then used to generate some replicate signals for further use in subsequent simulation and experiments.

5.1 Capture of a vibration source

As proposed, in order to extract the maximum output power from an energy harvesting generator, the generator has to be designed so that it will oscillate in its resonant mode. Therefore the frequency spectra from potential vibration sources need to be examined in advance so that the generator can be designed to match the desired ambient frequency. Therefore, the vibration spectrum for a number of household objects was measured. In this section, two types of spectrum capturing methods will be demonstrated. The first method is called Oscilloscope capturing and followed by the second method called Data Acquisition Toolbox Adapter (DAQ 2205) capturing.

An accelerometer (MTN1800) with a sensitivity of 991.5mV/g was selected in this capturing. This allows a measurement range of ±10g and a wide frequency response from 5Hz to 14 kHz. However, to ensure that the accelerometer will perform at its best accuracy, a constant and sufficient current is required to supply the accelerometer during the

measuring process. The operating circuitry for the accelerometer is attached as Figure 5.1. The transistor in this circuit will behave like a current regulator to ensure that there is constant current supply for the accelerometer (approximately 6mA). The Op-amp acts as a differential amplifier to step down the DC level of the output generated from the accelerometer to ensure that the captured vibration signal swing is in the range of ±10V, which is the maximum rating for the data acquisition adapter (DAQ-2205).

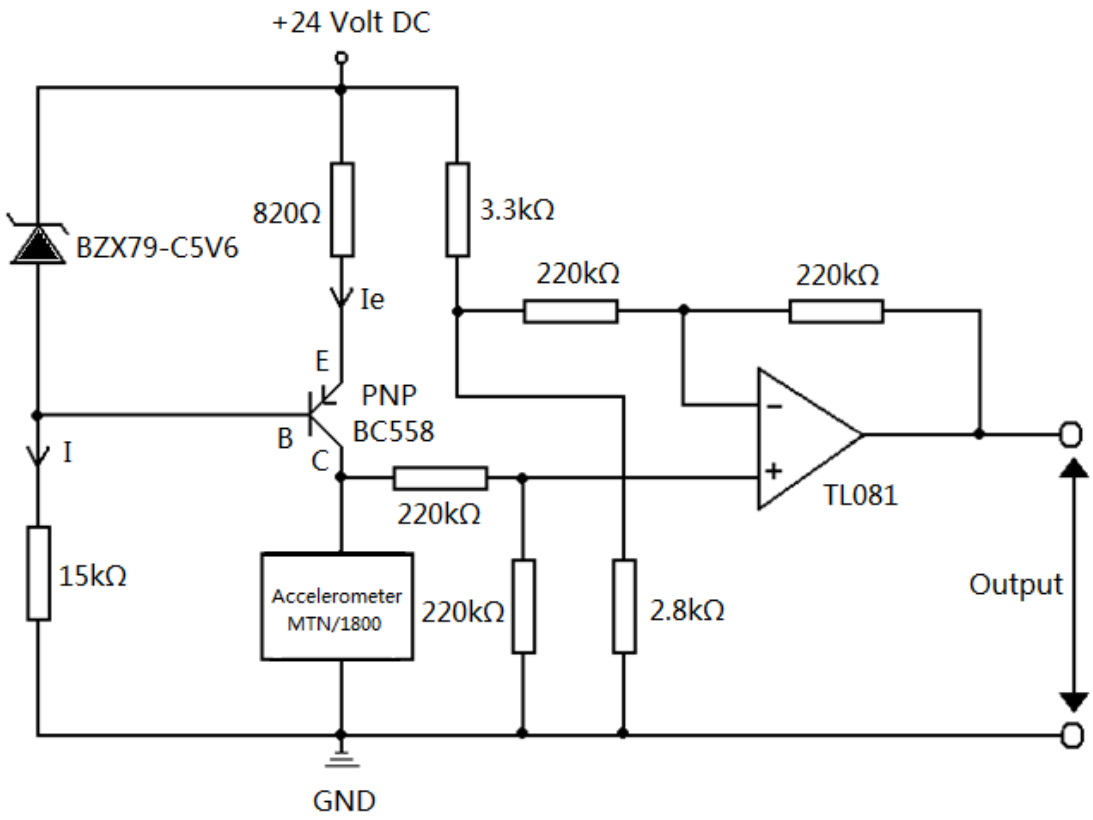

Figure 5.1- An operation circuitry for an accelerometer (MTN 1800)

5.1.1 Oscilloscope Capturing

An oscilloscope capturing method is the way of obtaining the vibration signal by using the oscilloscope (Agilent MSO-6054A). The different stages for this process are depicted in Figure 5.2. The vibration source taken from the object of interest is captured by using an Accelerometer (MTN1800). The obtained voltage is then measured using the oscilloscope (Agilent MSO-6054A) and records into USB flash drive. The data is then

transferred to the Matlab workspace (through a function file from Agilent Technologies) from the USB drive and the frequency spectrum of the captured data is plotted. The Matlab source code for this method is attached as Appendix A.

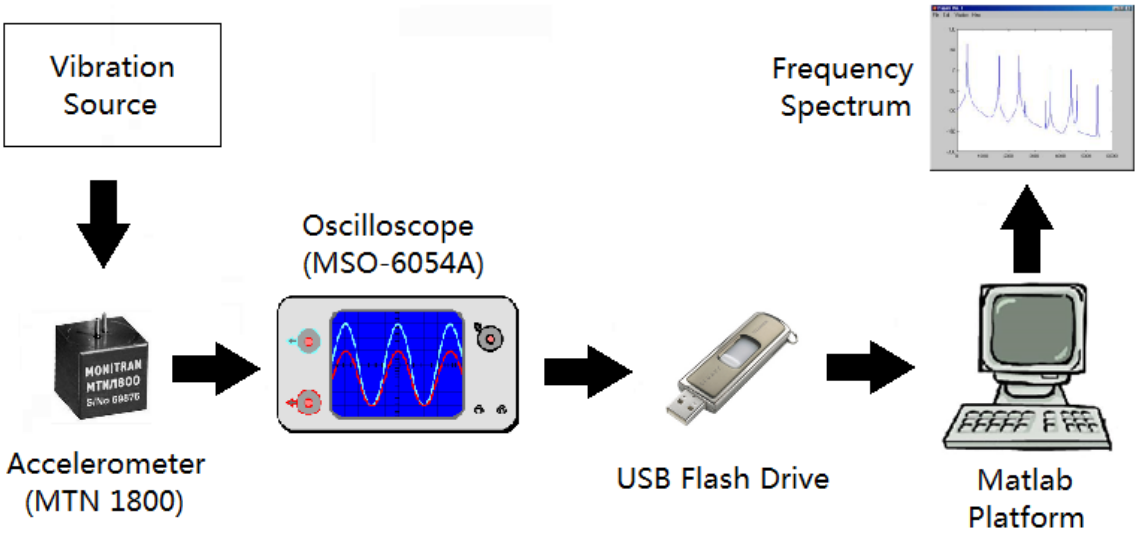

Figure 5.2 – Process of oscilloscope capturing

5.1.2 Data Acquisition Toolbox Adapter (DAQ2205) Capturing

For data acquisition toolbox capturing, the only difference in this process is the captured data from the accelerometer is transferred into the Matlab workspace directly instead of going through another storage medium. A 16-bits (500kS/s) multi-function acquisition adapter (DAQ2205) converts the analogue signal from the accelerometer into a digital form and Matlab will then work out the FFT (Fast Fourier Transform) of the data and the frequency spectrum is plotted. The processes are depicted as Figure 5.3 and the Matlab source code for this acquisition adapter is attached as Appendix B.

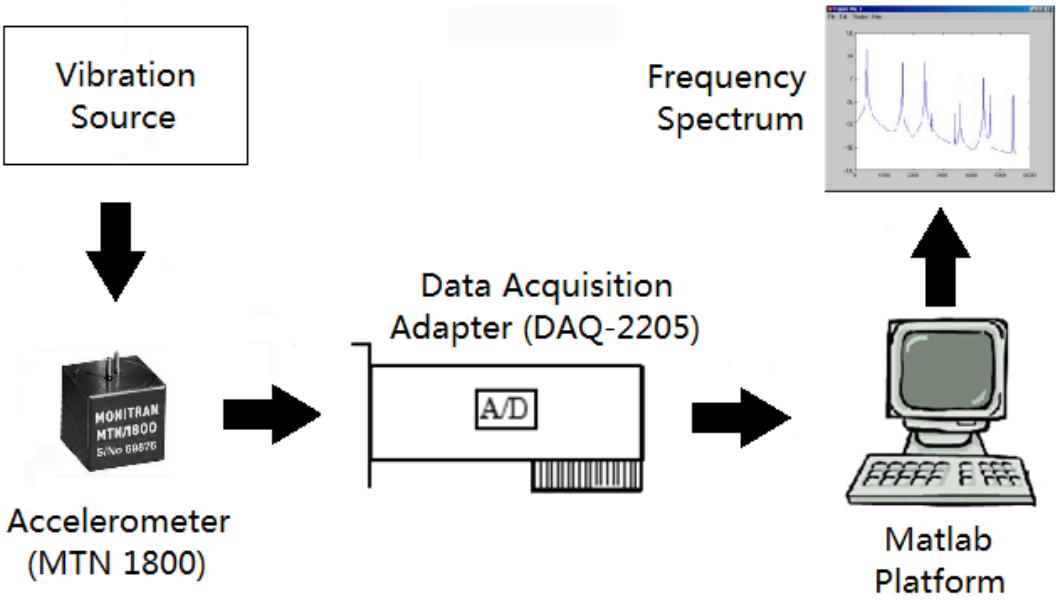

Figure 5.3 – Process of data acquisition toolbox adapter capturing

5.2 Generation of a vibration source

Naturally, most of the ambient vibrations are non-deterministic, meaning that its future behaviour cannot be precisely predicted. This is a so called random vibration. However, to cut down the complexity of the generation coding, only a simple way to generate the sinusoidal wave is proposed here. A vibration can be generated from a vibrator shaker and a driving signal is required. The driving signal used to drive the shaker needs to be calibrated in advance to ensure that the acceleration of the generated vibration is consistent over a range of frequencies. This procedure ensures that these results obtained from different generators in the next few chapters under this vibrator shaker are comparable.

To ensure the generated signal is adaptable and behaves closely to the real ambient vibration, the vibrating amplitude and frequency must be adjustable. Figure 5.4 shows a block diagram for the generation of a sinusoidal vibration. The form of the signal is created in a signal generator (in this case the Matlab platform), where the amplitude of the

acceleration and frequency can be adaptively adjusted. The generated signal is then converted into an analogue form by sending it through the data acquisition adapter (ADLINK DAQ-2205) before the amplification process in the amplifier (LDS-PA100E). Finally the amplified signal will be sent to the vibrator shaker (LDS-V406/8) and transformed into a mechanical vibration.

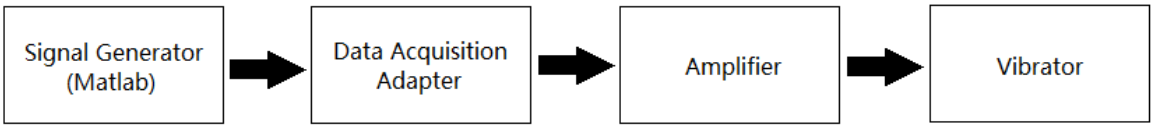

Figure 5.4- Block diagram for the generation of a vibration

To create the signal in Matlab, the basic sinusoid wave form as a function of time (t) is use:

$$y(t) = Ysin(\omega t + \emptyset) \tag{5.1}$$

where Y is the amplitude or the peak deviation of the function from its centre position

ω is the angular frequency for the signal

∅ is the phase shift

In order to make Equation (5.1) to be more specific for this vibration generation, the amplitude Y can be substituted with acceleration (A) and gravity (g = 9.81ms^{-2}) terms as:

$$y(t) = \frac{A}{g}sin(\omega t + \emptyset) \tag{5.2}$$

Practically, every machine has its own natural frequency. The vibrator shaker (LDS-V406/8) that is used in this research is no exception. In order to ensure that the designed system will provides a constant acceleration driving vibration to the vibrator under a range of different frequencies, a calibration test using an accelerometer has been carried to determine the calibration constant $K_c(\omega)$ for this system and the Equation (5.2) can be further modified as:

$$y_c(t) = K_c(\omega)\ \frac{A}{g} sin(\omega t + \emptyset) \tag{5.3}$$

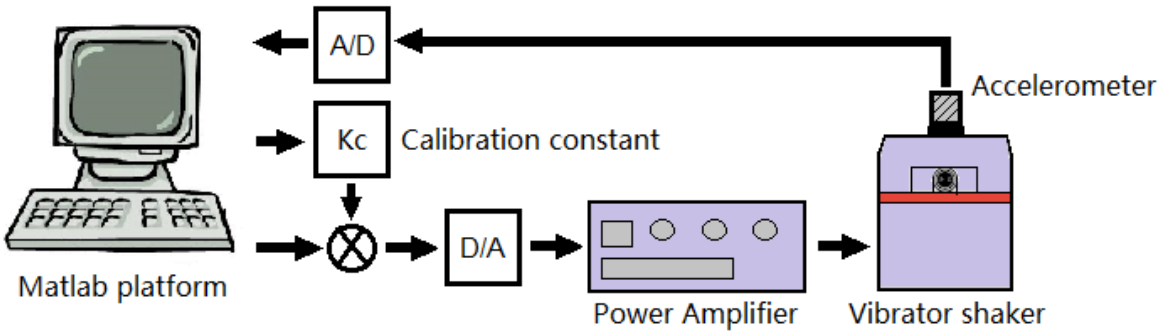

Figure 5.5- Vibrator shaker calibration setup

The configuration of the calibration setup is depicted as Figure 5.5. This configuration shows a feedback system in which the output from the generator (Matlab) will be tuned accordingly to its feedback input obtained from the accelerometer on the vibrator through an A/D converter. The calibration constant K_c is the variable given by the system in order to tune the generated signal to ensure that the acceleration of the driving vibration is constant over the desired range of frequencies. The value for the calibration constant against frequency is plotted as Figure 5.6.

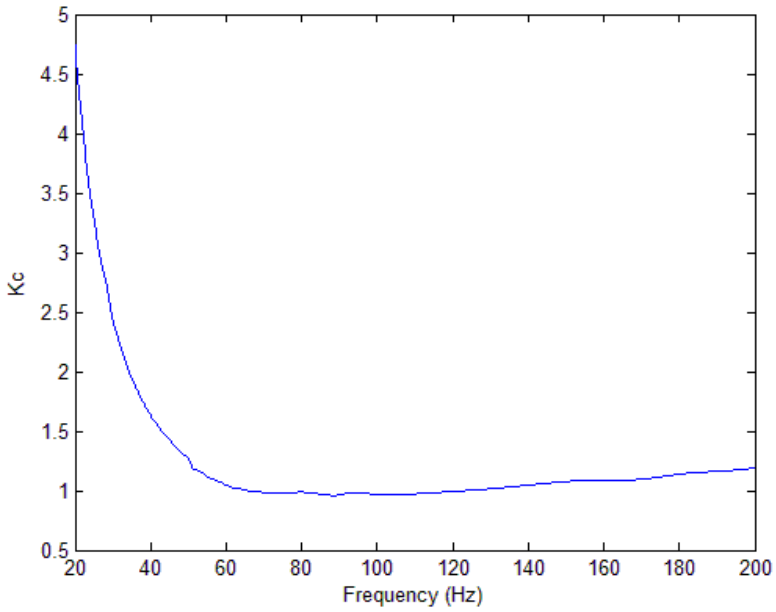

Figure 5.6 - The calibration constant under a range of different frequencies

To generate a constant vibration signal, the signal generator (in this case the Matlab platform) will retrieve the user input such as the desired acceleration of the output, frequency, and repeating loops, followed by the system calibration to obtain the appropriate value of K_c. From Figure 5.6 the calibration plot, it can be clearly seen that under different driving frequencies, a different calibration constants (K_c) is requires to be multiplied with the original signal to ensure that the acceleration on the vibrator shaker is consistent. Finally, the signal generator will generate the output with the number of repetition entered by the user before it stops. The flow chart of the code is shows as Figure 5.7 and the Matlab coding for this signal generation is attached as Appendix C.

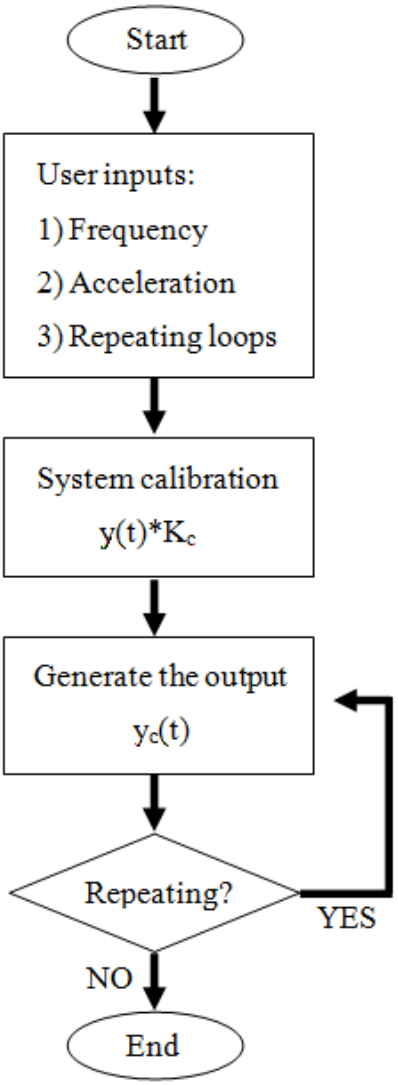

Figure 5.7 - Flow chart of the Matlab vibration signal generation

5.3 Discussion on generation and capture of vibration sources

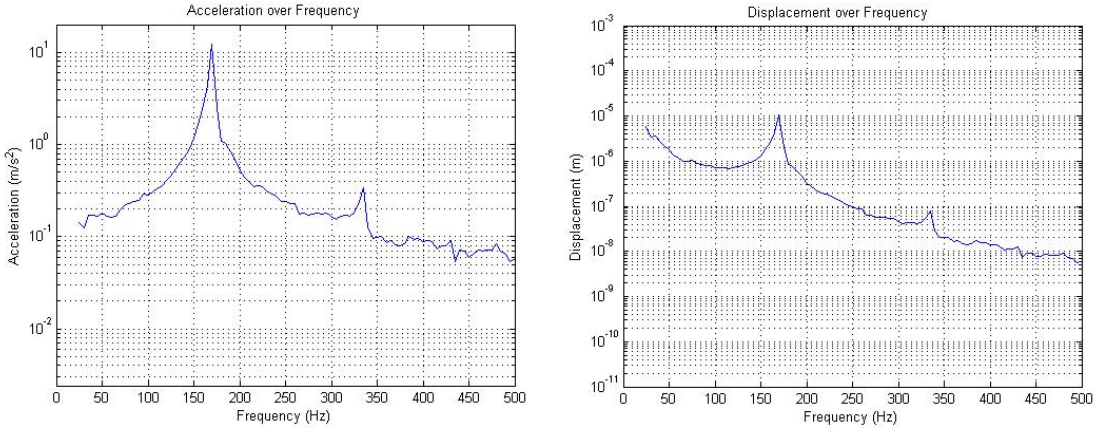

(a) – Spectra measured from the back of mobile phone case

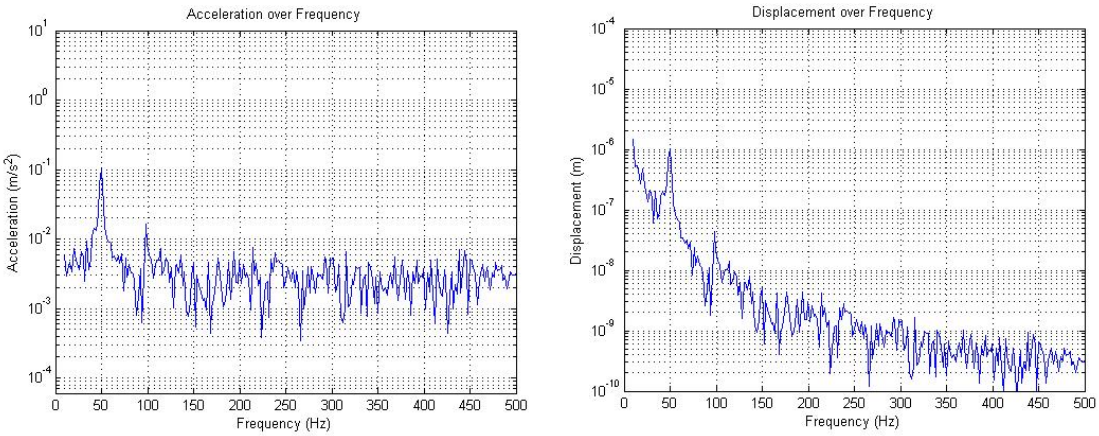

(b) – Spectra measured from the top of a domestic freezer

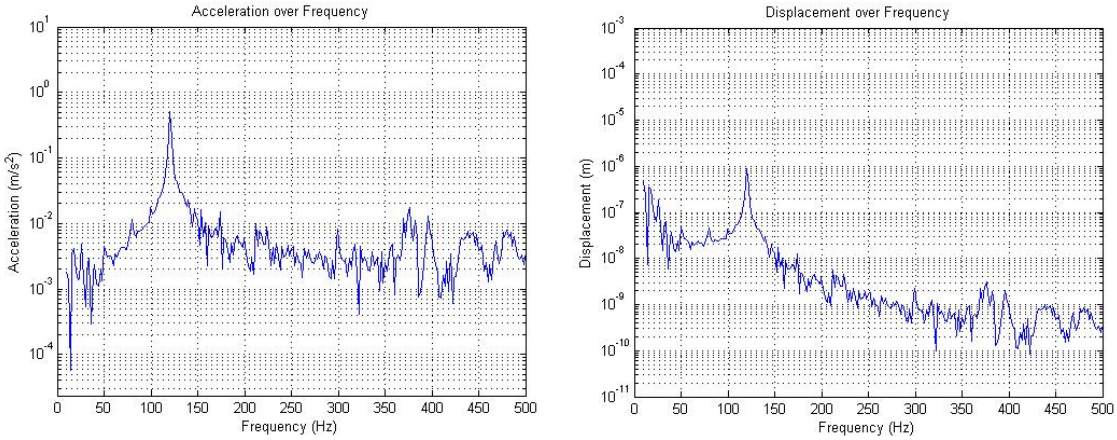

(c) – Spectra measured from the top of a desktop computer with CD is resting

Figure 5.8 – Vibration spectra for a number of household objects by author's experiments

For vibration sources capturing, although both capturing methods will provide a similar frequency spectrum as in Figure 5.8, both have their pros and cons. The advantage of using the oscilloscope capturing is the mobility. Some outdoor vibration readings, for

example the vibration of a tunnel, can be obtained by just using the accelerometer, oscilloscope and USB flash drive. The data in the USB flash memory is then transfer to the machine back in the lab and the frequency spectrum can be obtained easily in the Matlab workspace. However, on the contrary, if the vibrating source is close to the workspace, for example the vibration on the table fan in the office, then the data acquisition toolbox adapter capturing is more appropriate to use in this case. The vibration signal will be transferred into the machine directly from the data acquisition adapter and the frequency spectrum can then be plotted by using Matlab workspace.

For the generation of the vibration source, though most of the objects of interest oscillate at random and unpredicted frequencies, it is still a good way to emulate the vibration source. Moreover, a constant driving frequency can be used to obtain the matched load resistance for the generator which will be further discussed later. Apart from that, a random vibration source can be easily created by doing some minor modification in this design since the initial concept was frequency adaptable generation. One of the examples is creating a function code that will randomly change the driving frequency of the system and apply it to the sinusoidal wave equation in Section 5.2 instead of taking the input from the user.

Chapter 6 : Piezoelectric Converter Modelling

In Chapter 3 and Chapter 4 some comparisons and up-to-date works were discussed between electromagnetic and piezoelectric converters. Chapter 6 will consider the analytical modelling of the piezoelectric converters. The models are then developed and validated. Both analytical and practical outcomes were compared to verify that the modelling is sufficient to use for design and output estimation purposes.

6.1 Setting up the Prototype

A piezoelectric cantilever bender can operate in one of two modes, 31 and 33 modes. Although the coupling for Mode 31 is much lower than the coupling in Mode 33, there are still many advantages to using Mode 31. Larger strain can be produced with smaller input force for Mode 31 and the resonant frequency for this type of operation is much lower. Roundy[51] suggested that the piezoelectric bender can be mounted as a fixed end cantilever as Figure 6.1 with a mass, M, placed at the free end of the cantilever. This can produce a larger strain effect to the piezoelectric material than in Mode 33 when a similar input is applied

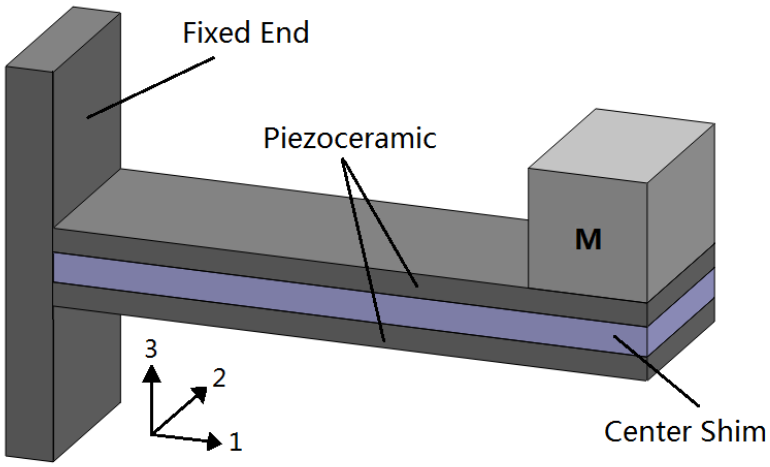

Figure 6.1 - Piezoelectric cantilever operation

The piezoelectric bender used here is a bimorph made of PZT (T220-A4-303Y) supplied by Piezo System Inc [43] in parallel. The thickness of the centre shim is 0.13mm and the total thickness for the bimorph with two ceramic layers as 0.51mm. Both the upper and lower ceramic sheets are connected and the centre shim connected separately. A mass of 4.1 gram is attached at the free end of the piezoelectric beam as depicted in Figure 6.2 and Figure 6.3. The piezoelectric is then clipped in between two sets of hard PVC, modelling a cantilever beam form. The piezoelectric prototype is then screwed to the surface of a vibrator which will be driven by a designed signal from Matlab via a Digital-to-Analogue interface card.

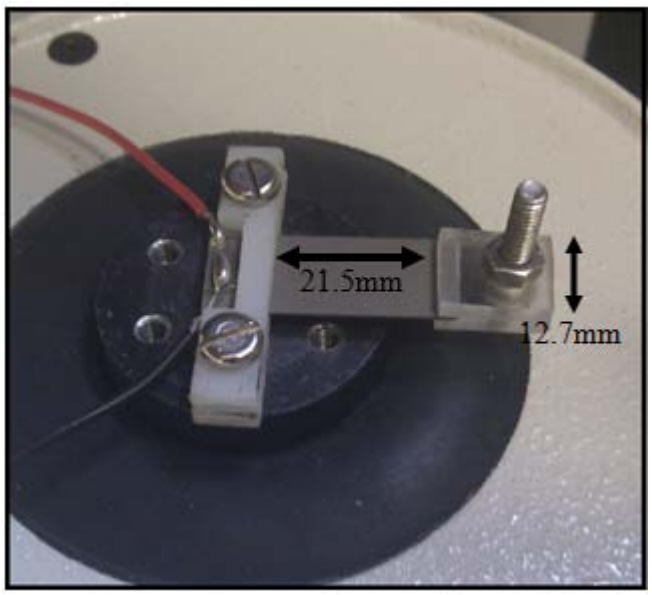

Figure 6.2- Parallel bimorph piezoelectric setup

6.2 Analytical and experimental power with varying load resistance

For an optimum power output from the generator circuit, the load needs to be matched to the effective internal resistance of the generator. Therefore, the effective internal resistance of the generator needs to be determined in order to select a suitable load.

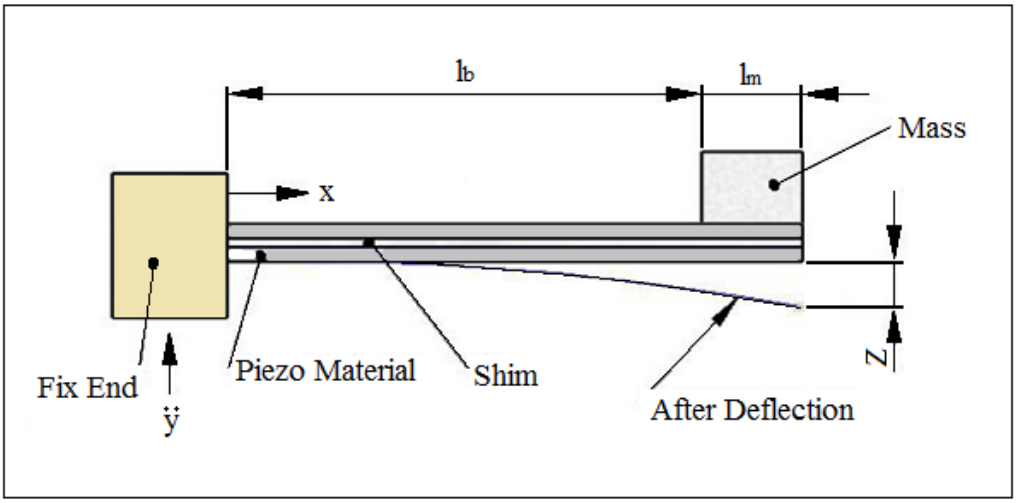

Figure 6.3- Schematic of piezoelectric bender

Figure 6.3 shows the schematic setup for the piezoelectric generator. The electrode length (I_e not shown in the figure) is the total length for the piezoelectric bender in this case. The interface block diagram is shown in Figure 6.4. A set of varying resistance values within the range of 6kΩ to 600kΩ is applied as the load for the generator. The initial tip mass is chosen as 4.1gram. The 0.5g driving signal generated from the Matlab is set at a fixed frequency of 73Hz, the measured resonant frequency of the beam. The generated power from the piezoelectric bender is then recorded along with the different resistive loads through the DAQ (Data Acquisition Adapter).

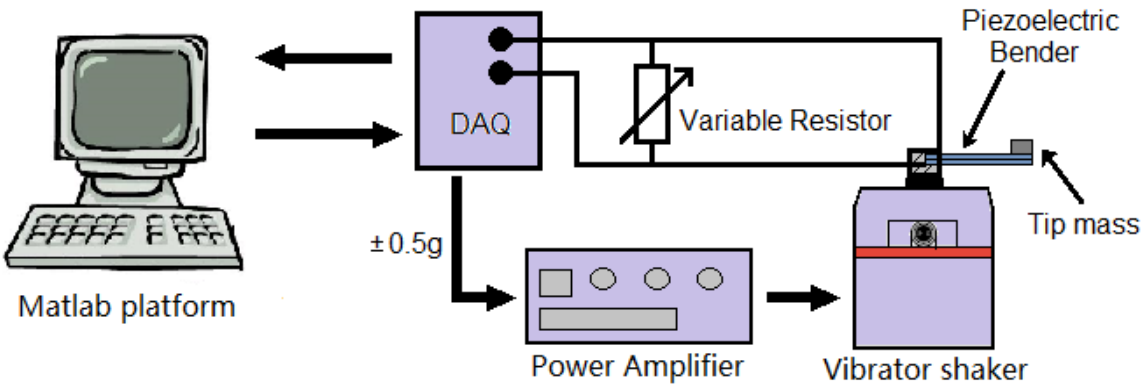

Figure 6.4 – Interface block diagram for varying load resistance

Again Roundy [51] showed that the magnitude of power transferred to the load for a piezoelectric bender can be given as Equation (6.1) assuming that the driving frequency is matches with the natural frequency.

$$P = \frac{1}{2\omega^2} \frac{RC_p^2 \left(\frac{Y_c d t_c b^*}{\epsilon}\right)^2 A^2}{\left(4\xi_m^2 + k_{co}^4\right)\left(RC_p\omega\right)^2 + 4\xi_m k_{co}^2 \left(RC_p\omega\right) + (2\xi_m)^2} \tag{6.1}$$

and

$$b^* = \frac{3b}{l_b^2} \frac{(2l_b + l_m + l_e)}{(2l_b + \frac{3}{2}l_m)} \tag{6.2}$$

where R is the load resistance

C_p is the capacitance of the piezoelectric device

Y_c is the Young's modulus for the piezoelectric ceramic

d is the piezoelectric strain coefficient

t_c is the thickness of an individual piezoelectric ceramic layer

ϵ is the dielectric constant of the piezoelectric material

ω is the driving frequency

ξ_m is the mechanical damping ratio

k_{co} is the electro-mechanical coupling coefficient

A is the acceleration of the vibration

b is the distance from the centre of the shim to the centre of the piezo layers

l_b, l_e, l_m are the lengths of the beam setup

Analytical modelling has been carried out by using Matlab based on Equation (6.1) and Equation (6.2). Figure 6.5 is a comparison of the prototyping output and the simulated output power from the piezoelectric bender for a range of load resistances. All the parameters used to substitute the variables in Equation (6.1) are show in Table 6.1. All the measured variables are labelled with (M) and the rest are taken from Piezo System data catalog. Refer to Appendix D for the Matlab code.

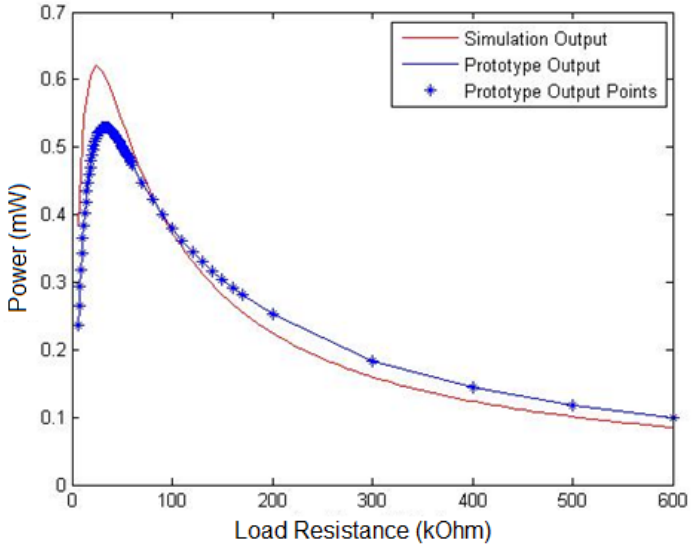

Figure 6.5 - Comparison of prototype output and simulated output for varying resistance

Variables in Equation (6.1)	Variables in Program	Values	Units
R	R	(M) 6k to 600k	Ω
C_p	C	(M) $51x10^{-9}$	F
Y_c	Y	$66x10^{9}$	N/m^{-2}
D	d	$-190x10^{-12}$	m/V
t_c	tc	$0.19x10^{-3}$	m
b*	b1	Equation (6.2)	m^{-1}
ϵ	e	$1.594x10^{-8}$	-
ω	w	(M) 2*pi*73	Hz
ξ_m	s	(M) 0.02858	-
k_{co}	k	0.29	-
A	A	(M) 4.905	ms^{-2}
b	b	$0.16x10^{-3}$	m
l_b	lb	(M) 21.5 $x10^{-3}$	m
l_e	le	(M) 31.5 $x10^{-3}$	m
l_m	lm	(M) 2 $x10^{-3}$	m

Table 6.1- Values for variables in Equation (6.1)

This experiment is basically done to find out the optimum value of the load resistance. From Figure 6.5 the result shows that the optimum value of the load resistance

for prototype output (blue) is approximately 30 kΩ in order to provide the maximum output power (approximately 0.53mW) with the driving frequency of 73Hz. On the other hand, for the simulated output (red line), the optimum value of the load resistance is approximately 25 kΩ and the optimum power at that point is approximately 0.621mW. Despite these small differences, the most important aspect of the behaviour is that both plots looked similar, indicating good agreement between the experiments and simulations, this suggests that Equation (6.1) is sufficient to use for modelling a simple piezoelectric beam.

6.3 Analytical and experimental power with varying driving frequency

For an optimum generator circuit, the environment vibration frequency needs to be matched to the system natural frequency. A similar prototype is tested in this experiment as depicted in Figure 6.6. But instead of varing the resistive output load; the driving frequency will be varied. A sinusoidal wave with acceleration amplitude of 0.5g and frequency between 50Hz to 90 Hz is used as the driving signal to the vibrator and the voltage generated from the bender is then recorded, along with the varying driving frequencies.

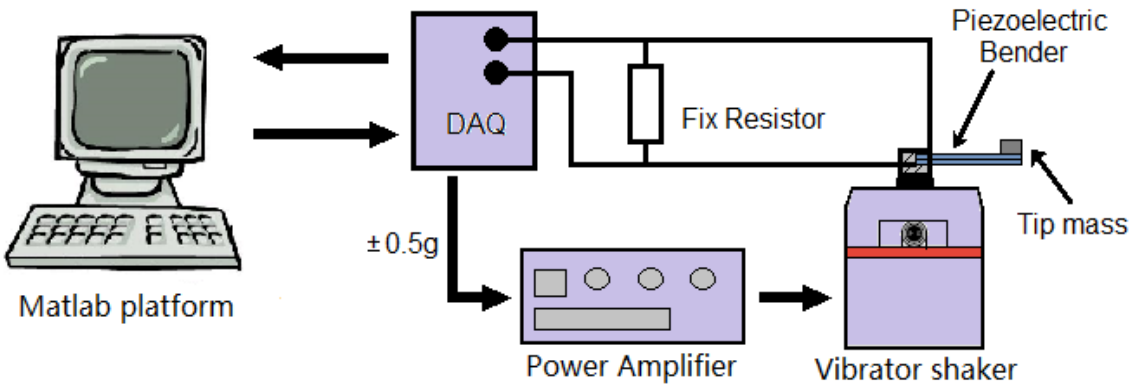

Figure 6.6 - Interface block diagram for varying driving frequency

However in order to analytically model the piezoelectric beam in varying driving frequency mode, Equation (6.1) is not sufficient to be used here. From Equation (6.4), the magnitude of the voltage transferred to the load for a piezoelectric bender can be given as Equation (6.3) [51] as below which can be simplified to Equation (6.1) if the driving frequency is matches with the system natural frequency.

$$V = \frac{-j\omega \frac{Y_c d t_c b^*}{\epsilon}}{\left[\frac{1}{RC_p}\omega_n^2 - \left(\frac{1}{RC_p} + 2\xi_m\omega_n\right)\omega^2\right] + j\omega\left[\omega_n^2(1+k_{co}^2) + \frac{2\xi_m\omega_n}{RC_p} - \omega^2\right]} A \tag{6.3}$$

where ω_n is the natural frequency for the system

and

$$P = \frac{V^2}{2R} \tag{6.4}$$

An analytical model has been developed using Matlab based on Equation (6.3) and Equation (6.4) with a set of different fixed resistive output loads. The lowest fixed resistive load is chosen as 6kΩ and gradually increases to 600kΩ. All the parameters used to substitute the variables in Equation (6.3) are as given in Table 6.1, except for the load resistance above. Figure 6.7 shows the 3D comparison between the generated power from the simulation and prototype generators followed by Figure 6.8 which shows their contour behaviour. Both 3D and the contour plots illustrate that the simulated and prototype generator are having a similar behaviour, only the overall magnitude of the generated power and rate of resonant frequency shifting are different between them.

As in Figure 6.7, the generated power from the simulated generator increases faster than the power generated from the prototype generator when the applied load is close to the measured internal matched resistance (30kΩ). From Figure 6.8, it can be seen that altering the output load will affect the natural frequency of the system. However, the

shifting which occurs in the simulated generator seems to be more orderly than the shifting that occurs in prototype generator. This may be caused by the circuitry and environment noises during the data capturing process. More details on frequency shifting by altering the output load will be discussed in the later chapter.

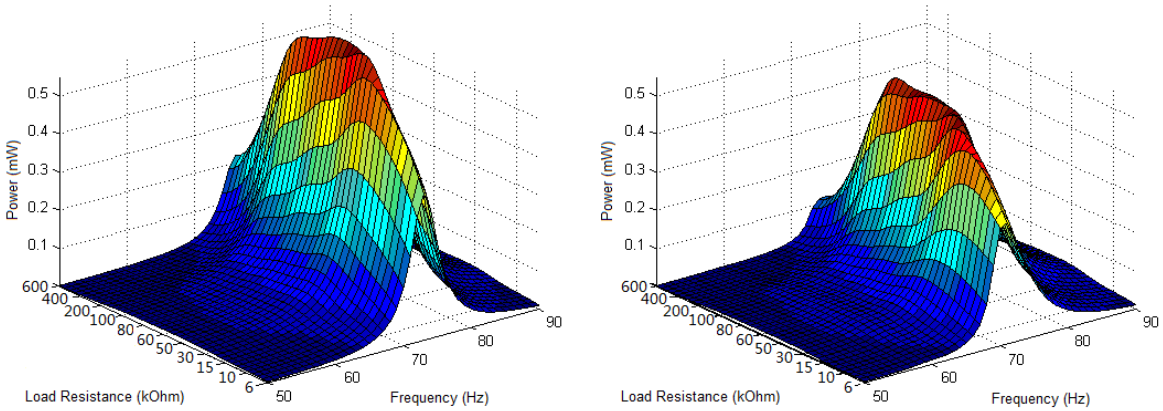

a) Simulation output b) Prototype output

Figure 6.7 – 3D comparison of simulation and prototype generated power

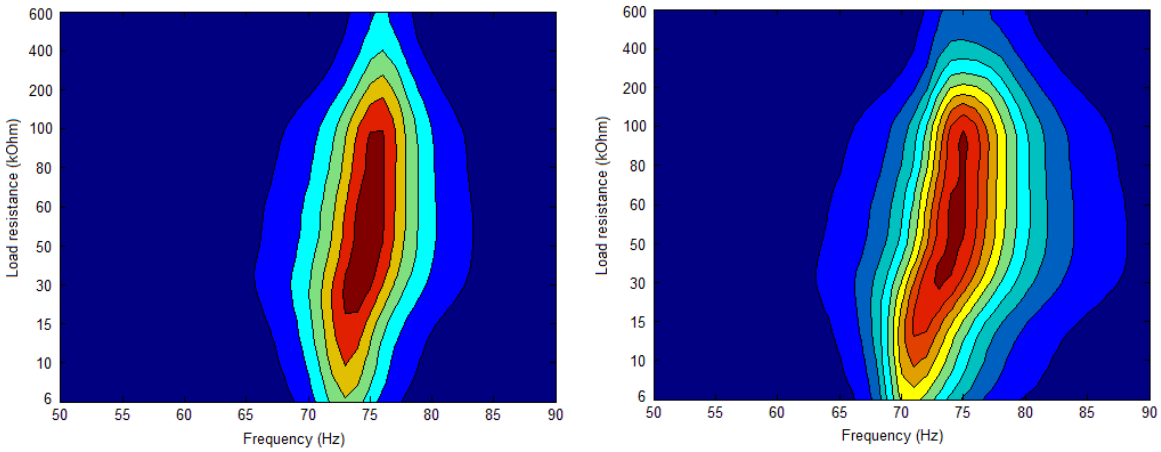

a) Simulation output b) Prototype output

Figure 6.8- Contours for the simulation and prototype 3D plots

Added to the above, to further verify the good agreement between the two, a multiple frequency response is plotted on the same axis with some modification on axis-x. In Figure 6.9, there are eleven sets of data being compared (n=1,2,3...11). All experimental results show the resonant frequency (f_{re}) at around 73 Hz. However they are

separated by an offset frequency (f_{off} = 20Hz) in order to fit into the same graph. The resultant frequencies on the axis-x for each set of data can be then express as:

$$f_n = f_{re} + f_{off} \times n \tag{6.5}$$

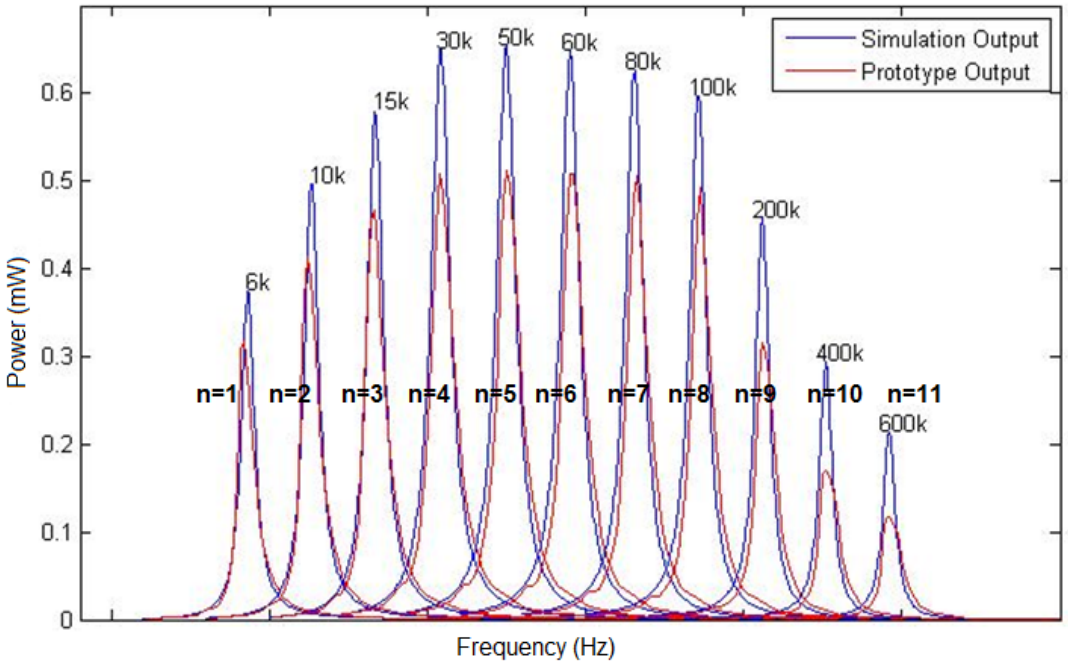

Figure 6.9 - Simulated and prototype frequency responses with a fixed resistive load

In Figure 6.9, the blue lines are the simulated output from the model and the red lines are the real practical prototype outputs. Both outputs have a similar behaviour; the output power differs slightly when the fixed resistive load is close to the measured internal matched resistance (30kΩ). However, the power drops significantly when the load resistance divergences from the matched value. Added to the above, the simulated output gives power that can be obtained only from a perfect beam. On the other hand, the prototype output shows lower output power being generated compared to the simulation, this is believed to be due to the fact the damping coefficient behave non-linearly against the load resistance. Plus there are some measurement, setup and circuitry loss during the practical experiment. Refer to Appendix E for more detail regarding the coding of the simulation.

6.4 Analytical and experimental power with varying tip mass

Williams [68] modelled a cantilever beam by a simple spring-mass system. This model was then modified by Challa [12] for the multilayered beam where the resonant frequency of the system can be expressed as:

$$\omega_{beam} = \sqrt{\frac{K_{beam}}{m_{eff}}} \tag{6.6}$$

the effective stiffness of a multilayered cantilevered beam can be written as:

$$K_{beam} = \frac{w}{4L^3}\left(\sum_{c=1}^{n_1} n_c Y_c h_c^3 + \sum_{s=1}^{n_2} n_s Y_s h_s^3\right) \tag{6.7}$$

where w is the width of the beam

L is the length of the beam

n_1 and n_2 are the numbers of ceramic and shim layers

Y_c and h_c are the Young's modulus and height of each piezo ceramic layer

Y_s and h_s are the Young's modulus and height of each shim layer

and the effective mass of a multilayered cantilever beam with a tip mass can be approximated as:

$$m_{eff} = 0.23m_{beam} + m_{tip} \tag{6.8}$$

where m_{tip} and m_{beam} are tip mass and the cantilever beam mass respectively

Equation (6.6) clearly indicates that the resonant frequency of the system will change according to the effective stiffness and the effective mass. When the stiffness of the beam increases, the natural frequency will increase. On the other hand, when the beam effective mass is increased, the natural frequency of the system will be decreased and vice

versa. A similar prototype is tested in this experiment but the fixed mass will be varied here. A sinusoidal wave with an acceleration amplitude of 0.5g is being use as the driving frequency to the vibrator and the power generated from the generator is then recorded along with the varying driving frequencies. The tip mass can be increased by increasing the number of screw attached at the free-end mass. The first initial tip mass (Mass1) is chosen as 4.1gram (single screw), followed by Mass2 = 4.87 gram (2x screws), Mass3= 5.64 gram (3x screws) and Mass4= 6.41 gram (4x screws).

$$P = \frac{m_{eff}\xi_e(\frac{\omega^2}{\omega_{beam}^3})A^2}{[1-(\frac{\omega}{\omega_{beam}})^2]^2+\left[2\xi_T\frac{\omega}{\omega_{beam}}\right]^2} \tag{6.9}$$

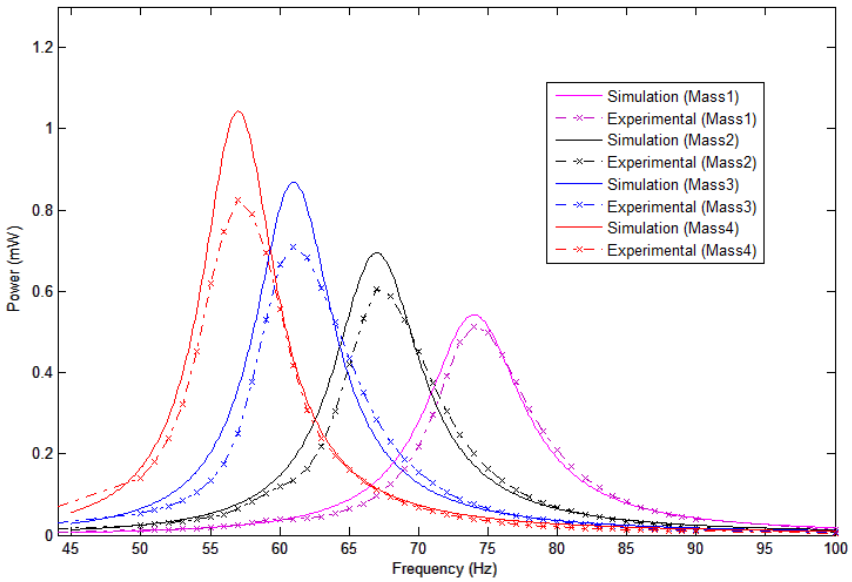

Figure 6.10 - Simulated and experimental frequency response for varying tip mass generator

Figure 6.10 illustrates the frequency response for four different tip mass generators based on the power statement in Equation (6.9) and experimental data. The dotted lines are the experimental data and smooth lines are the simulated data. By looking at both simulated and experimental data, there is a drastic change in terms of the natural

frequency of the system when the mass of the system has changed. The natural frequency increases by approximately 5.5 Hz averagely when the mass of the system decreases by 0.77 grams. This phenomenon agrees well with Equation (6.9) where the natural frequency of the system is inversely proportional to the tip mass. As a result, the mass is strongly recommended to be taken as an adjustable criterion if a system is to be designed in order to match the natural frequency of the system with the varying environment fundamental frequencies. However, it is worth noting that the system itself basically limits the maximum mass that could be applied for a given acceleration level to avoid mechanical breakage.

Chapter 7 : Alternative geometry of beam structures

A piezoelectric bender produces an electric charge through deformation of the piezoelectric material and the charge generated is proportional to the strain. Besides, the peak strain must be limited to avoid damage to the cantilever. Therefore, it means that maximizing the average strain of the beam should maximize the output energy. In order to maximize the average strain, the strain on each point on the cantilever beam must be uniform and as large as possible without exceeding the material breakage limit. In recent years, many researchers [4][23][37] have focused on the performance of a cantilever beam with alternative geometries and they found that potential design geometries can increase the performance of the scavengers in term of output power density. However, the recent research appears to assume that the strain across the width of the cantilever beam was constant, whereas the strain distribution on a real cantilever beam does not behave accordingly in practical case. In this chapter, practical behaviour of the strain distribution was studied and the outcome was compared to an analytical modelling.

In this chapter, to reduce the complexity of the task, only five single layer beams with different geometry structures will be compared in term of their strain distributions by using analytical and numerical methods. These structures consist of ordinary rectangular beam, triangular trapezoidal beam, and some elliptical beams. They were first compared by using a simple analytical model and followed by a more complex numerical model using ANSYS [3] (a general-purpose finite element analysis software). Added to the above, the feasibility of improving the energy density from the cantilever bender by changing the beam's depth (height) was assessed. This chapter will conclude with an experimental comparison of output power between the practical rectangular and triangular cantilever beams.

7.1 Analytical modelling of alternative beam structure

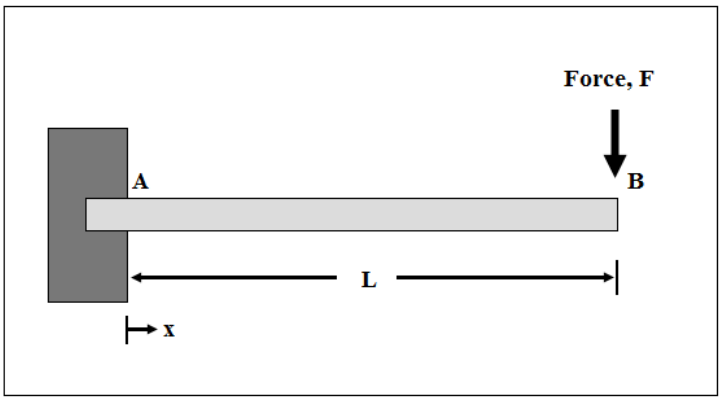

Figure 7.1– Cantilever beam carrying a concentrated load

For a massless cantilever with one end fixed and another end free as shown in Figure 7.1, the bending moment (M) at point x along the cantilever and the moment of inertia (I) of a beam from point A to point B (L) can be expressed as below [10]:

$$M = F(L - x) \tag{7.1}$$

$$I = \frac{bh^3}{12} \tag{7.2}$$

where F is the free end force

x is the position along the beam which is counted from point A to point B

b and h are the width and height dimension of the cantilever beam respectively

For this derivation, it will be assumed that the strain across the width of the cantilever is constant and that the deflection is small. From Equation (7.1), it is clear that when x=L, the bending moment, M, will become zero. This indicates that ideally there is no Bending Moment at the free end of the cantilever (point B). Generally, the tensile stress experienced by the beam can be expressed as Equation (7.3) as below:

$$\sigma = \frac{Mc}{I} = Ec\frac{\partial^2 u}{\partial x^2} \tag{7.3}$$

where c is distance from the neutral axis to a point of interest

$\frac{\partial^2 u}{\partial x^2}$ is the second derivative of the beam deflection, u.

E is the Young's Modulus for the beam material

It is known that the relationship which gives the bending strain at any locations as a function of beam curvature (R) and the distance from the neutral axis can be given as [19]:

$$\varepsilon = \frac{c}{R} \tag{7.4}$$

Substituting Equation (7.3) into the general form of material Young's Modulus, $E = \frac{\sigma}{\varepsilon}$ and comparing it to Equation (7.4) will give the axial strain above the neutral axis as:

$$\varepsilon = c\frac{\partial^2 u}{\partial x^2} = \frac{\mathrm{Mc}}{\mathrm{IE}} \tag{7.5}$$

This indicates that the second derivative of the beam deflection is given as inversion of the radius of curvature, $\frac{\partial^2 u}{\partial x^2} = \frac{1}{R}$. Refer to Appendix F for more detail of the proof. Equation (7.5) will then be used to generate the relative strain from the different structure in this analytical modelling.

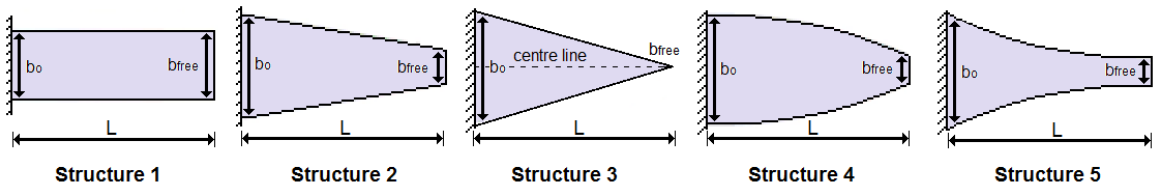

Figure 7.2 - Alternative beam geometry structures

Figure 7.2 shows the five different alternative beam structures that were used in this modelling. Structure 1 is an ordinary rectangular beam, Structure 2 is a trapezoidal beam and Structure 3 is the triangular beam (ultimate trapezoidal condition). Elliptical

beams (Structure 4 and Structure 5) were included in the modelling to further investigate the effect of beam strain while the geometry varies elliptically. Only the strain on the centre line (only shown in Structure 3 but applies to all structures in the figure) from each structure will be considered and compared. All structures are fixed on their left end and a tip force is applied on their free end. The beam length (L) and the beam height (h not shows in the figure) are fixed for all the structures as 30mm and 2mm respectively. All the fixed and free end widths are shown in Table 7.1. The manually defined curves in Structure 4 and Structure 5 together with the model algorithm are attached in Appendix G.

Structure (s)	Fixed end width, b_o (mm)	Free end width, b_{free} (mm)
1	10	10
2	15	5
3	15	very small <1
4	16	4
5	16	4

Table 7.1- Width dimensions of the alternative beam geometries

Each structure is equally split into n_L nodes (η_L=3000) along the centre line along the beam length (L). By substituting all the variables according to the geometry into Equation (7.2) and Equation (7.5), the strain may be calculated at each node. Modelling has been carried out in the Matlab workspace and the relative strain ratios against the beam length are plotted as in Figure 7.3. To normalise all the relative strain from the different structures, the obtained strain values from each node in the structures are divided by the maximum strain of that particular structure to obtain the Strain ratio (ε_{ratio}). This is to ensure that all data obtained from the different geometry structures is comparable with each other regardless of their maximum and minimum strain value.

$$\varepsilon_{ratio\,[i]} = \frac{\varepsilon_{[i]}}{\varepsilon_M} \tag{7.6}$$

where i is the index number of the node in the structure

$\varepsilon_{[i]}$ is the strain on node i

ε_M is the maximum strain of the structure

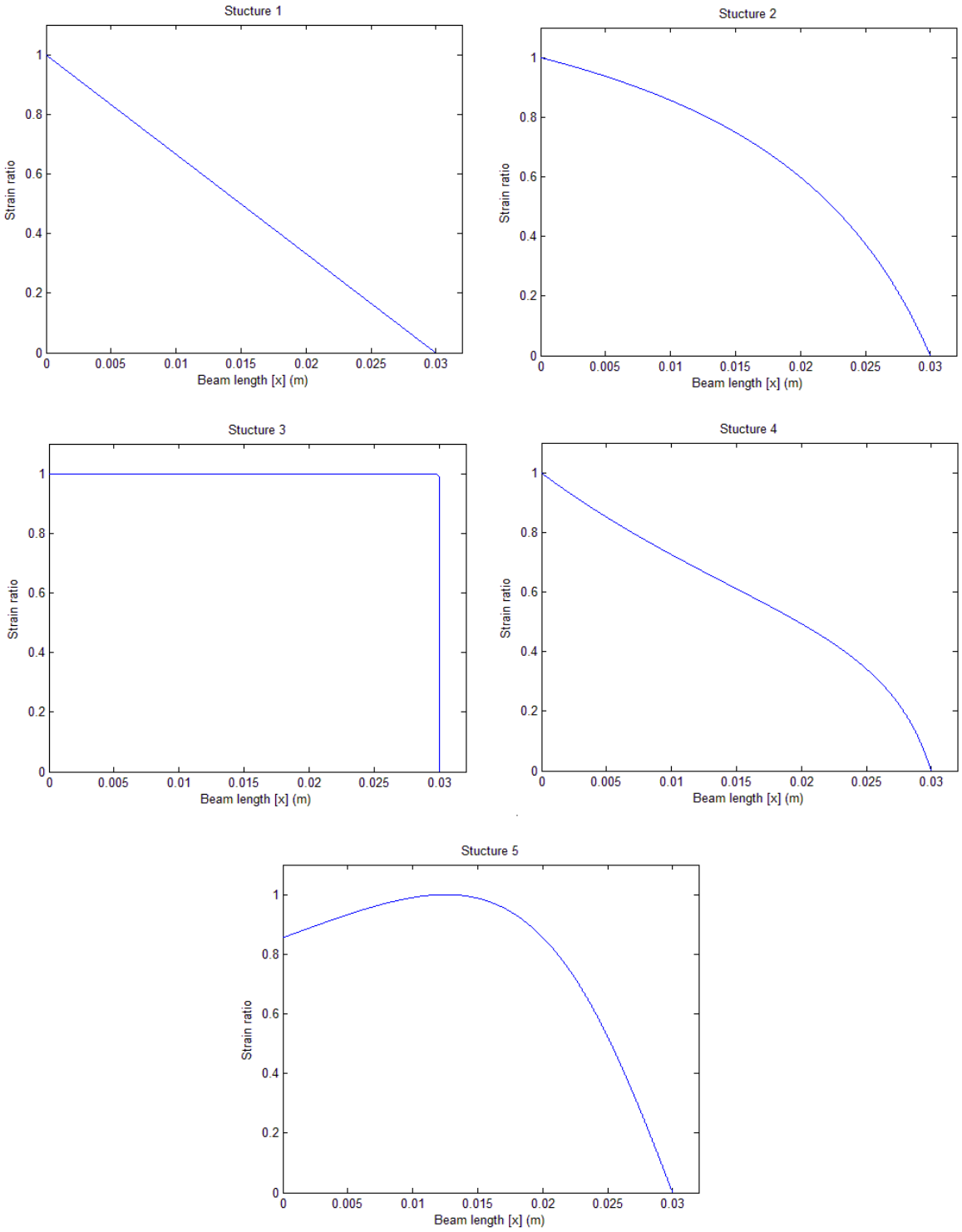

Figure 7.3 - Relative strain (analytical) along the centre of the beams

Figure 7.3 shows the normalised relative strain ratio along the centre line of the cantilever beam for the five alternative geometries. It is known that the strain needs to remain almost constant along the beam so that a constant strain distribution can exist on the beam structure. For Structure 1, an ordinary cantilever beam which exhibits a rectangular profile, a strain concentration at the clamped end where the bending moment (M) is at a maximum will be created. The strain ratio will decrease linearly from the maximum to minimum along the cantilever beam. Followed by the increasingly triangular trapezoidal profile Structure 2, the normalised strain start to decrease from the maximum and the rate of decrease is linearly increasing until it reach the minimum at the free end of the cantilever. Apart from that, for the triangular geometry in Structure 3, the strain energy curve is almost perfect, with constant strain along the beam's length and a dramatic decrease to the minimum when it reaches the free end of the beam.

Added to the above, for Structure 4, the average strain curve for this structure is above the curve provided by Structure 1. At the early stage, the strain energy starts to reduce slowly from a similar maximum value but its rate of decrease increases during the later stage before it reaches the minimum at the free end. Lastly, on Structure 5, the normalised strain does not decrease at the beginning stage; however it begins to increase from a certain value to its maximum while it proceeds to the middle stage. After the middle stage, the rate of decrease of the curve will gradually increase until the strain ratio reaches zero.

Figure 7.3 shows the relative strain ratios along the centre line of the beam. However, the volume of material experiencing a particular strain ratio is what we are interested. This can be estimated by assigning the strain ratios obtained from the centre line of the beam to the entire nodes available on each beam structure and by assuming that the strain across the width of the cantilever beam is constant. Due to the fact that the cross

section of the tested beam structures are vary along the beam, therefore the total number of available nodes across the width at every x position on each structure are assigned accordingly to their beam width at that x position. The general equation of the total nodes available across the beam width at x position for those tested structures can be given as:

$$\eta_b(x) = \left| \frac{b(x)}{b_{free(3)}} \right| \tag{7.7}$$

where the b(x) is the beam width of the tested structure at x and $b_{free(3)}$ is the free end width in the Structure 3 (smallest beam width among the structures). The value of the Strain ratio $\varepsilon_{\text{ratio}}(x)$ is then applies to the available nodes obtained from Equation (7.7) according to the x position. By taking the sum of the total nodes available across the beam width for the entire x positions along the beam, the total available nodes on the structure can be expressed as:

$$\eta_{total} = \sum_{x=0}^{L} \eta_b(x) = \eta_b(0) + \eta_b(1) + \cdots + \eta_b(L) \tag{7.8}$$

In order to make the comparison more effectively, the assigned strain ratios are plotted into a histogram according to an equally split set of bins. The data is normalised into the number of nodes in percentage by $\eta_{\%\#} = \frac{\eta_\#}{\eta_{\text{total}}} \times 100\%$ as in Figure 7.4, where the $\eta_\#$ is the number of nodes available in that particular bin (#=0, 0.05, 0.1, 0.15, ..., 1). The percentages of the nodes for the five different geometries are summarised in Table 7.2. Only the percentage of nodes, having the Strain ratio that is larger than 0.5 ($\eta_{\%>0.5}$)and 0.75 ($\eta_{\%>0.75}$)are listed. According to the data from the table, the best strain distribution structure can easily be determined.

Beam Structures	Percentage of nodes with Strain ratio > 0.5 ($\eta_{\%>0.5}$)	Percentage of nodes with Strain ratio > 0.75 ($\eta_{\%>0.75}$)
Structure 1	50.00%	25.00%
Structure 2	84.32%	62.44%
Structure 3	100.00%	100.00%
Structure 4	78.15%	38.88%
Structure 5	91.78%	85.55%

Table 7.2 - The percentage of the strain ratio (analytical) for the investigated structures

In Figure 7.4, it can be seen that the Structure 1 have almost equal amount of nodes in each level of strain ratio. Follow by Structure 2 for which the number of nodes increases when the level of the strain ratio goes from low to high. For Structure 3, it shows an almost perfect strain distribution with almost all the available nodes highly strained at the highest level of the strain ratio. For Structure 4, most of the nodes are distributed around the middle range of the level of the strain ratio. Finally, for Structure 5, though most of its available nodes are highly strained, it is still less efficient if compared to the Structure 3. In Table 7.2, it clearly indicates that Structure 3 gives the best strain distribution among the structures in Figure 7.2 according to the strain ratio percentage. It consist of 100% of the nodes that having the strain ratio which is larger than 0.5 and 0.75.

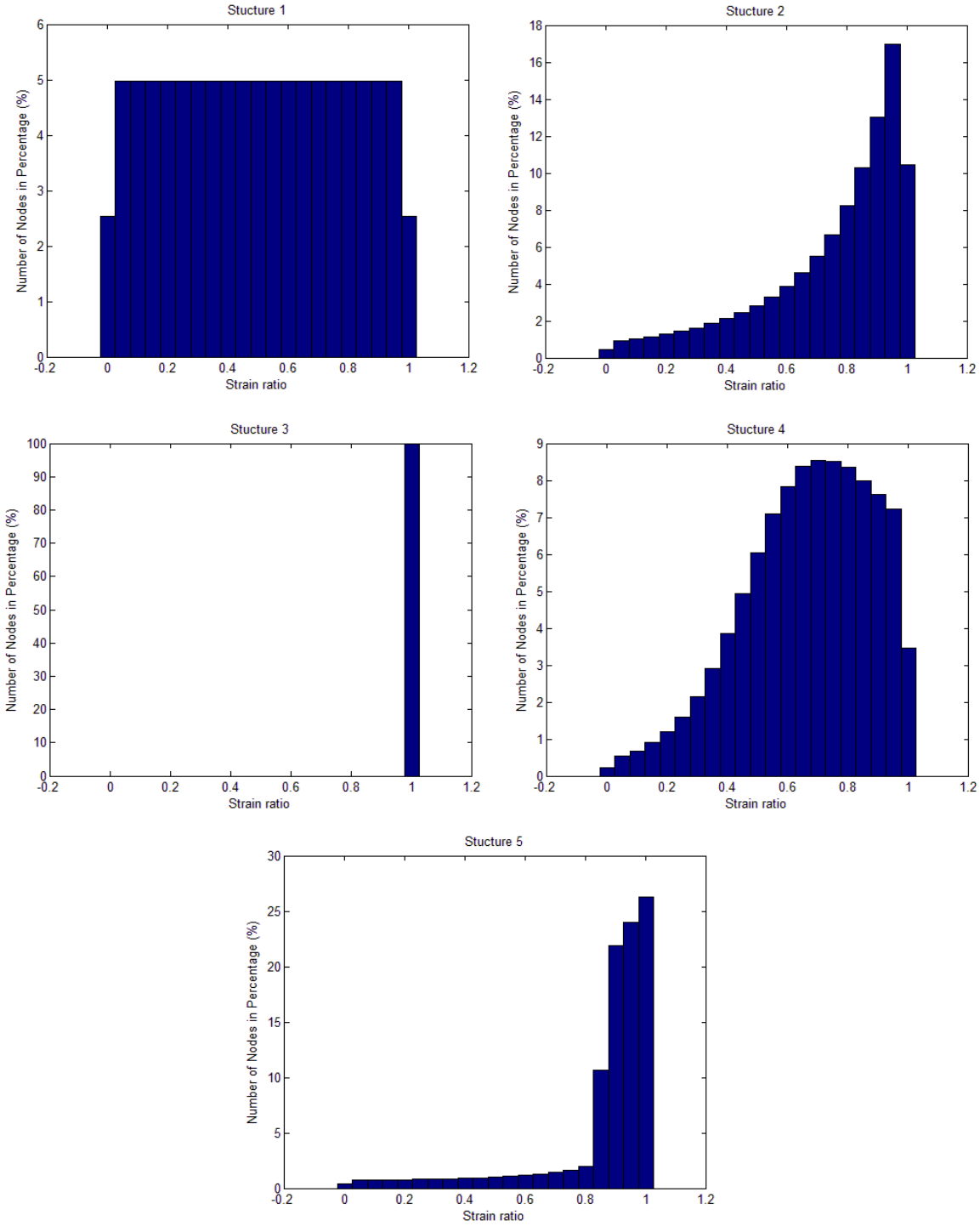

Figure 7.4 - Strain distribution (analytical) according to the number of nodes

The above analysis shows that the strain distribution in a beam can be improved by carefully altering the structure of the cantilever beam. To further this modelling, the height (depth) of the beam can be changed. Figure 7.5 shows three types of cantilever structures which have the total beam length, L=30mm. The first structure is the beam with width varying along the cantilever (similar to Structure 3 in Figure 7.2), the second structure is

the beam with height varying along the cantilever (from 6mm at the fixed end to 2mm at the free end), and lastly the third structure is the beam with both height (similar to the second structure) and width (from 15mm at the fixed end to 4mm at the free end) varying along the cantilever.

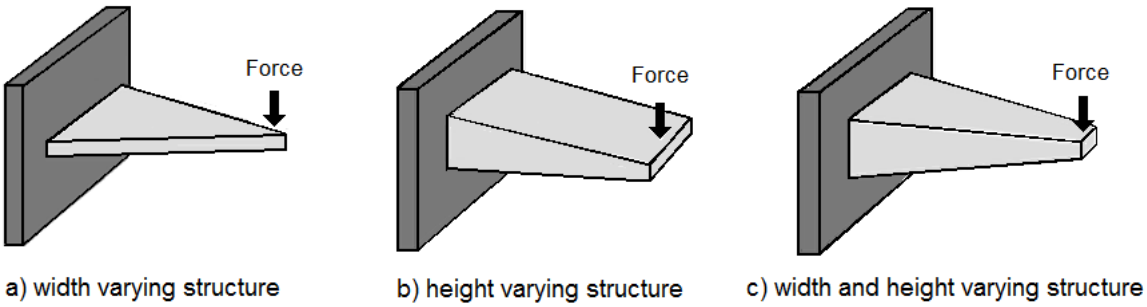

Figure 7.5 - Cantilever beams with width, height varying

By assume that the strain concentration for the material through the height (near the neutral axis line) of the beam is very low. The resultant strain ratio curves along the centre line of the cantilever beam for those structures shown in Figure 7.5 are depicted as Figure 7.6. It is clearly seen that by varying the height (depth) of the beams as in Figure 7.6b) and Figure 7.6c), the normalised strain will increase to its maximum from a certain value and drop significantly at the free end. This behaviour is similar as in the Structure 5 that was compared previously in Figure 7.3. From these analyse, it is known that height varying cantilever beam can be replaced by carefully adjusting the curvature along the cantilever beam in Structure 5, which is much easier to be manufactured if compared to the height varying structure.

Although a higher maximum strain is obtained by using height varying structures under an equal amount of input force, this will cause breakage of the beam if the average strain of the beam is pushed to the limit for optimisation purposes. By assuming that the dotted lines shown in the figures are the material breakage limit for the piezoelectric

cantilevers, both structures with varying height will fail if the averages strains of the beams are the main concern because their maximum strain will exceed the maximum limit of the material if the average strain is pushed to the limit. On the other hand, for the triangular geometry as in Figure 7.6a), the average strain can be pushed to the level just slightly below the material technical failure limit to improve the performance in terms of energy generation. Therefore, alternating the height of the beam is not a helpful way for output energy improvement.

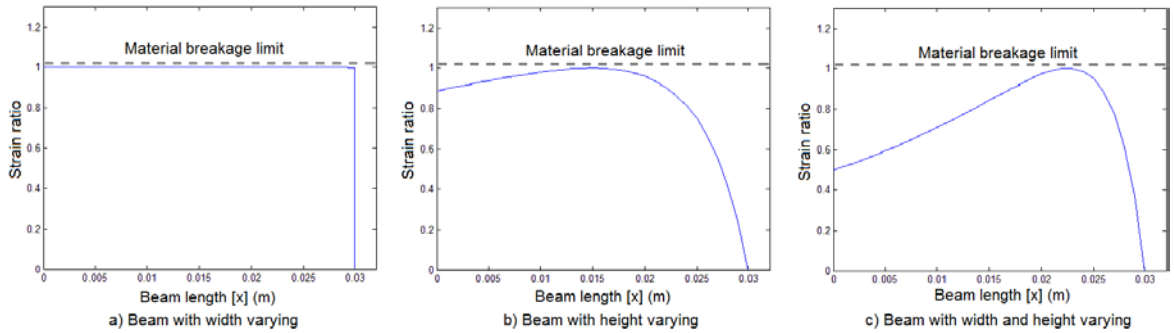

Figure 7.6 - Relative strain for width and height varying structures

7.2 Numerical modelling of alternative beam structure by ANSYS

In the previous modelling, the strain across the width of the cantilever was assumed to be constant. However, practically it is not the case. Therefore, modelling has been carried out on similar structures as shown in Figure 7.2 using ANSYS to compare the strain distribution for a single layer piezoelectric (PZT-5A4E) cantilever. The Young's Modulus and Poisson's ratio for this type of 5A4E material are $66Nm^{-2}$ and 0.31 respectively [43]. All the structures are fixed on their left end and have a block of tip mass (10×5×2mm) applied on the free end on the right. A constant force is applied on the striped surface of the block as shown in Figure 7.7. The tested structures are discretized (Meshed) with a constant element size of 1mm in length as depicted in Figure 7.8. The red dashes lines show the location where the tip mass have been placed on each structure.

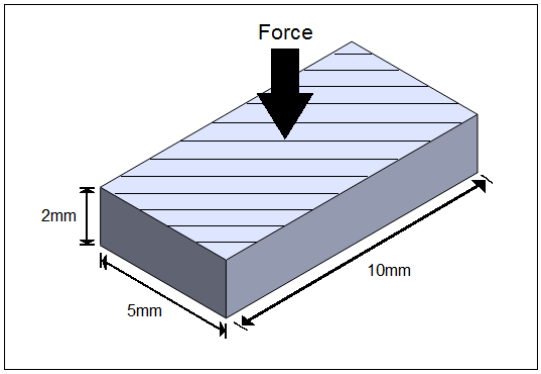

Figure 7.7 - Tip mass with a constant force applied on the striped surface

By applying an equal amount of force to all the tested structures using the tip mass which is placed at the free end of each structure, the strain distribution for these beam geometries can be calculated as illustrated in Figure 7.9. The colour zones on each structure indicate the differences of the strain level at that point. To ensure that the maximum strain for each structure is limited before the material breaking limit, take Structure 1 as an example: this structure will possess the highest strain at the left end (RED) of the structure and the strain will gradually decrease to the lowest level at the right end (BLUE) of the structure. Due to the fact that the maximum strain for every structure is

altered when the geometry has changed, it is necessary to normalised the obtained data; the Strain ratio (ε_{ratio}) from each element in the structures are determined. This normalisation is not only to ensure that all data obtained from the different geometries are comparable within this modelling, but also comparable with those obtained from the previous analytical model.

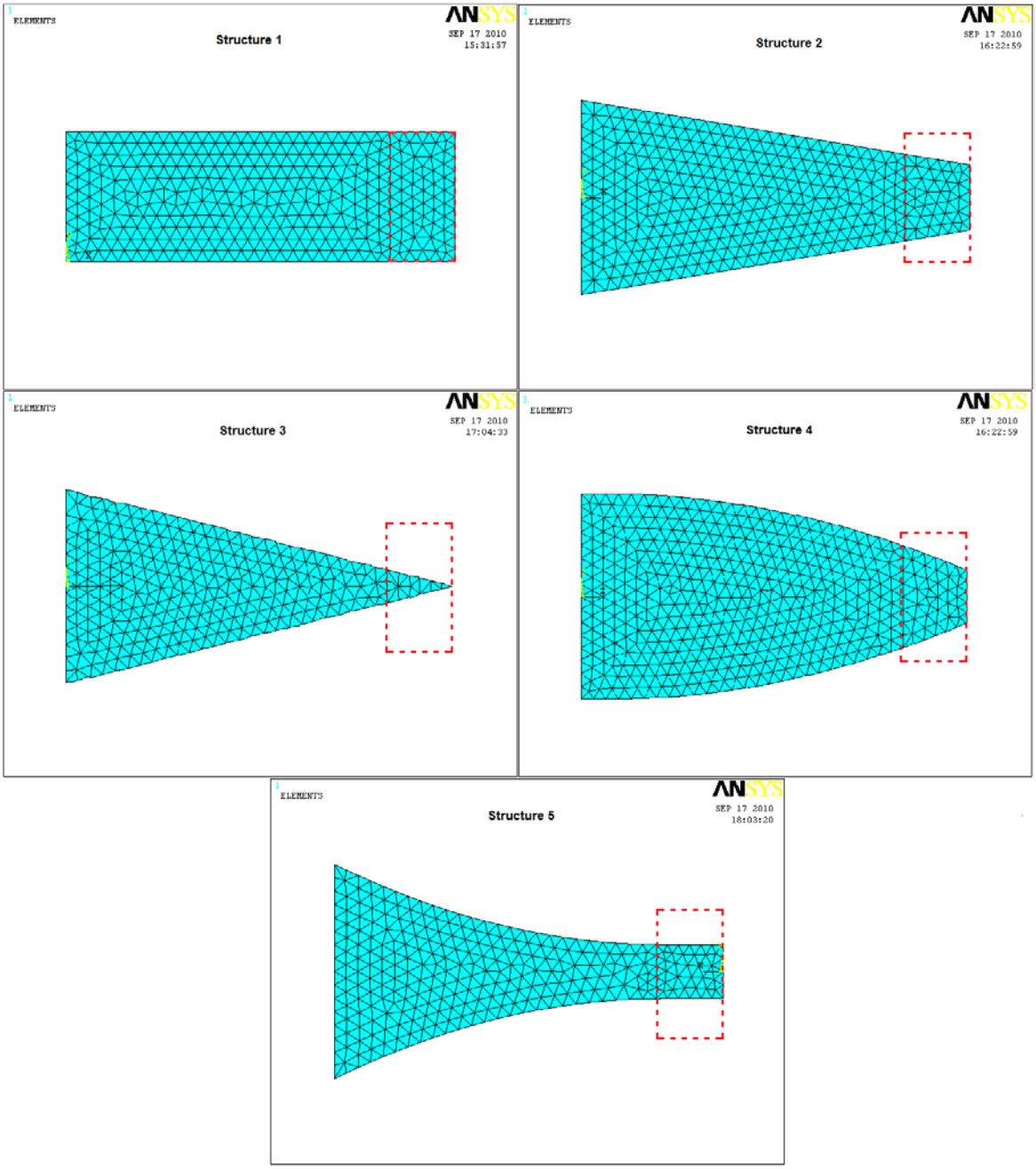

Figure 7.8 – Discretization of the alternative beam structures

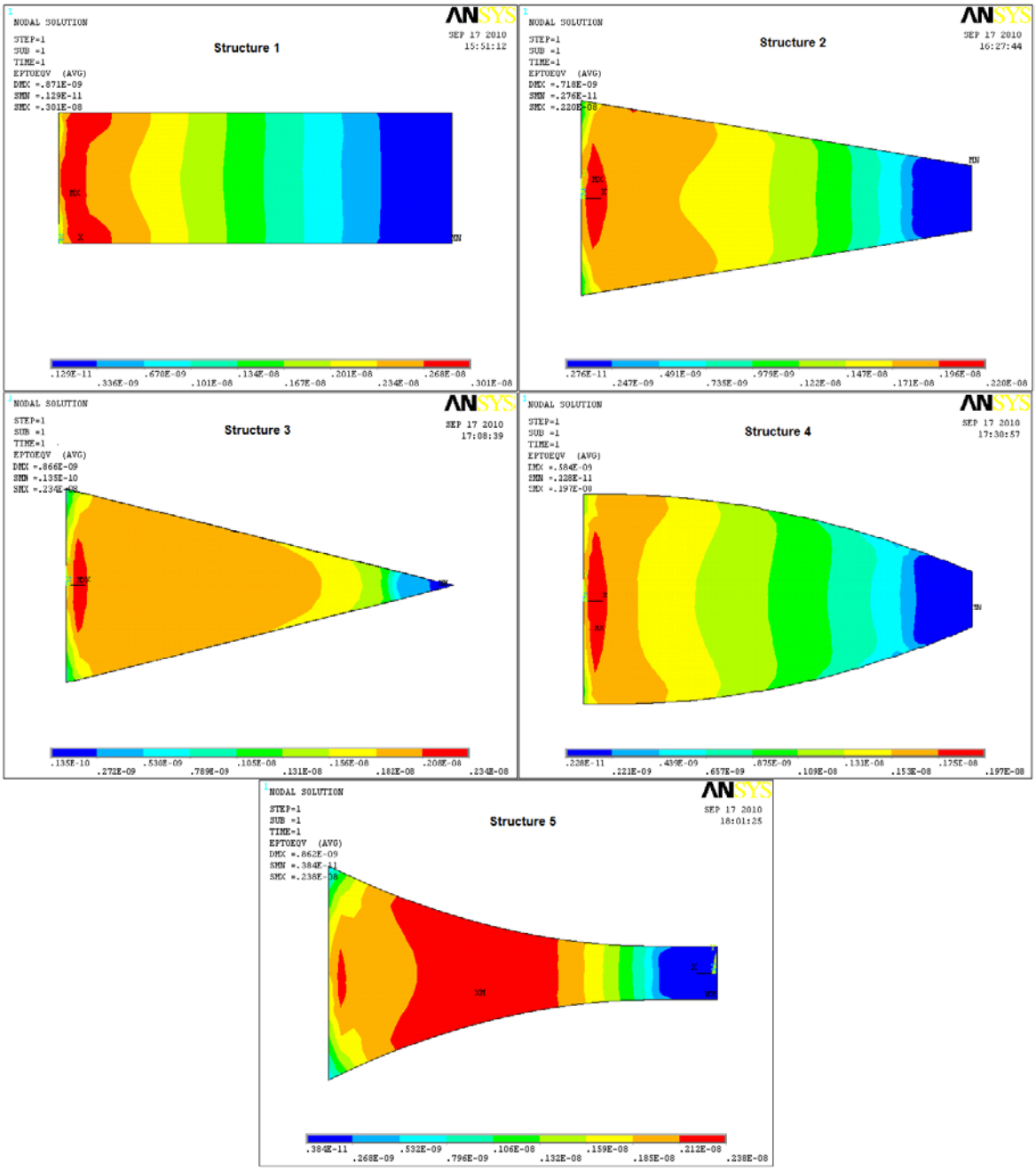

Figure 7.9 - Strain distribution (ANSYS) for alternative beam geometries

As depicted in Figure 7.9, the strain distribution on each structure differs when the beam geometry varies from Structure 1 to Structure 5 and is not uniform across the beam width. However, it is hard to determine which structure provides the most even strain distribution by just observing their colour zone. Therefore, the relative strain along the beam centre line (refer to Figure 7.2) and the histogram according to the number of nodes in percentage for each structure are plotted as in Figure 7.10 and Figure 7.11 respectively. Moreover, due to the strain across the width of the cantilever is not constant on each

geometry, therefore the data shows in Figure 7.10 and Figure 7.11 looked more disordered than those shown in Figure 7.3 and Figure 7.4. Nonetheless, they are similar in the sense of their behaviour.

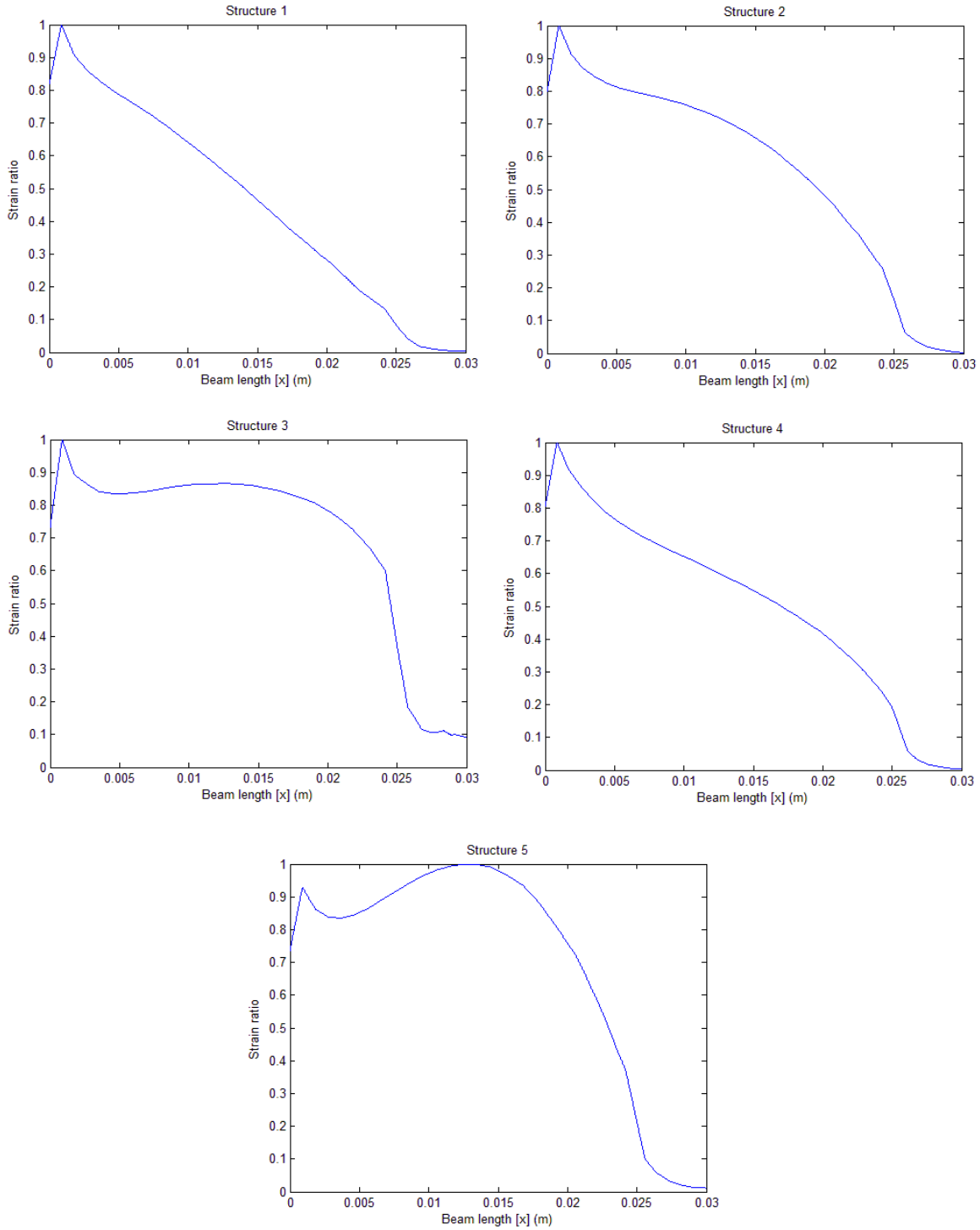

Figure 7.10 - Relative strain (numerical) along the centre of the beam

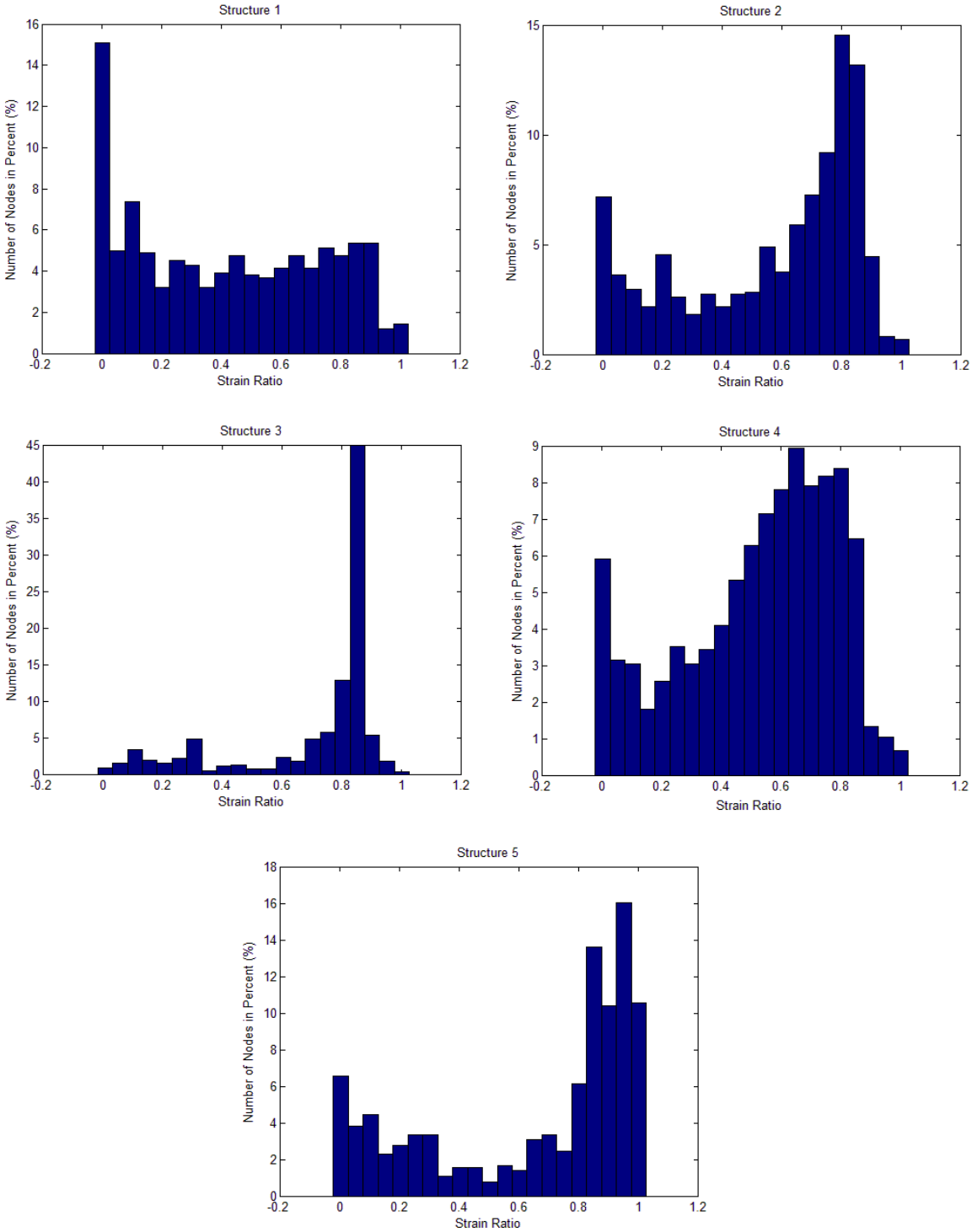

Figure 7.11- Strain distribution (numerical) according to the number of nodes

As illustrated in Figure 7.9, there is a region of material that is highly strained which is located next to the fixed end at the left end on each structure. Similarly in Figure 7.10, the relative strain plots shown that all the tested structures have a spike at approximately x=1mm, which imply a high stress concentration at that beam section.

Subsequently, this has reduced the maximum strain which allowed to be applied on each structure before the material breakage. On the contrary for Structure 5, the stress concentration at the middle part of the beam seems to be higher than the one near the fixed end. As described previously in the structures width & height varying section, this kind of strain distribution pattern will fail if the average strain of the beam is the main concern. This is because the maximum strain provided by this beam will exceed the maximum limit of the material first if the average strain is pushed to the limit.

Beam Structures	**Percentage of nodes with Strain Ratio > 0.5 ($\eta_{\%>0.5}$)**	**Percentage of nodes with Strain Ratio > 0.75 ($\eta_{\%>0.75}$)**
Structure 1	42.09%	20.45%
Structure 2	65.57%	38.75%
Structure 3	81.02%	68.22%
Structure 4	61.08%	21.98%
Structure 5	69.16%	57.86%

Table 7.3- The percentage of the strain ratio (numerical) for the investigated structures

The percentages of the nodes with a particular strain ratio for the numerical simulation are summarised in Table 7.3. Only the percentage of nodes, having the strain ratio that larger than 0.5 ($\eta_{\%>0.5}$) and 0.75 ($\eta_{\%>0.75}$) are listed. Although the overall resultant numbers shown are less than those obtained in Table 7.2, it clearly indicates that Structure 3 still gives the best strain distribution according to the nodes percentage. It consist of 81.02% of the nodes that having the strain ratio which is larger than 0.5 and 68.22% for the nodes that having the strain ratio which is larger than 0.75. Refer to Appendix H for the complete Matlab coding.

7.3 Experimental comparison of triangular and rectangular cantilevers

In this section, an experimental comparison between a triangular and rectangular beams with the same tip mass (4.1gram) was carried out and the actual output power obtained for both cases. Figure 7.12 shows a bigger rectangular bender (Q220-A4-503Y) and a bender that is carefully cut into a triangular shape from a smaller rectangular bender (T220-A4-303Y as in Chapter 6). Using a similar setup configuration as in Section 6.3, both benders are connected to their optimum matched resistances (71kΩ for triangular and 22kΩ for rectangular respectively). A sinusoidal wave with acceleration amplitude of 0.5g was used as the driving frequency to the vibrator and the power generated from the generator was then recorded for a range of driving frequencies (40Hz to 60Hz). The generated power was then calculated as $P = \frac{V^2}{R}$ where V is the peak voltage transferred to the resistive load for the system R.

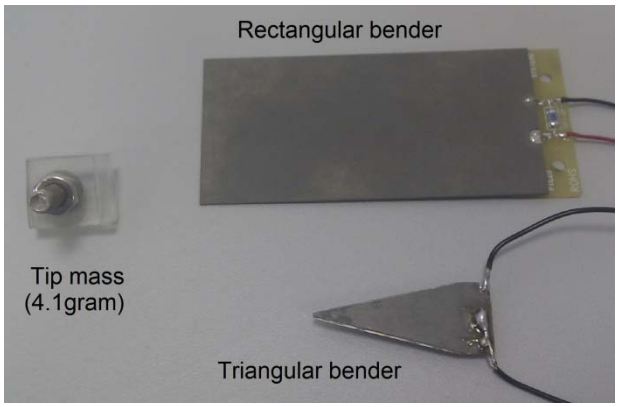

Figure 7.12 - Rectangular and triangular piezo bender

Figure 7.13 illustrates the frequency response for both triangular and rectangular beams. It can be seen that the optimum power generated by the rectangular beam is higher than the triangular beam. The rectangular beam achieved 1.581mW at 43.7 Hz and triangular beam only achieved 0.227mW 45.5Hz. However, in this case the beams volumes are different. The effective volume used for the rectangular bender is 721mm^3

(44.5×31.8×0.51mm) and on the other hand, the effective volume for the triangular beam is only 56.1mm^3 (0.5×20×11×0.51mm). Therefore, it is unfair to compare two different shapes of bender in different beam's volume. Hence, both readings are normalised to the same beam volume as depicted in Figure 7.14.

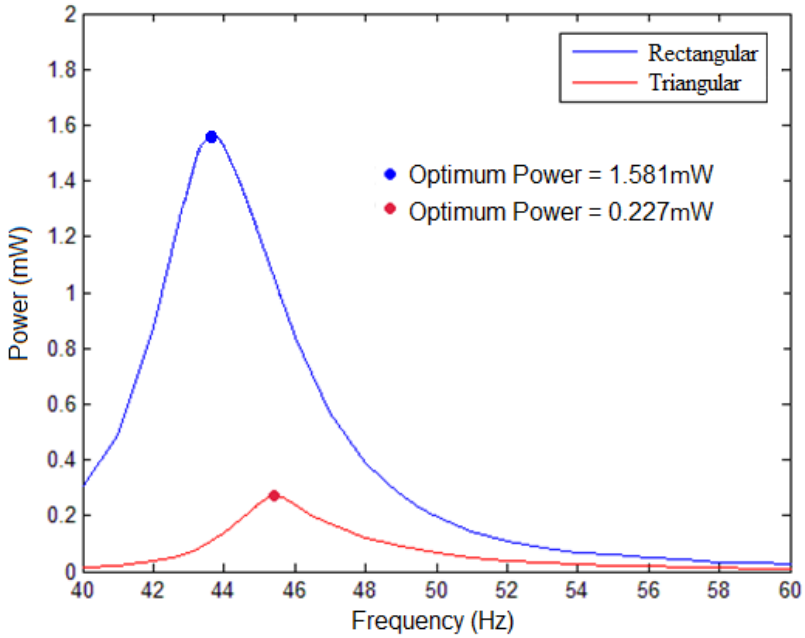

Figure 7.13 - Frequency response with different beam's volume

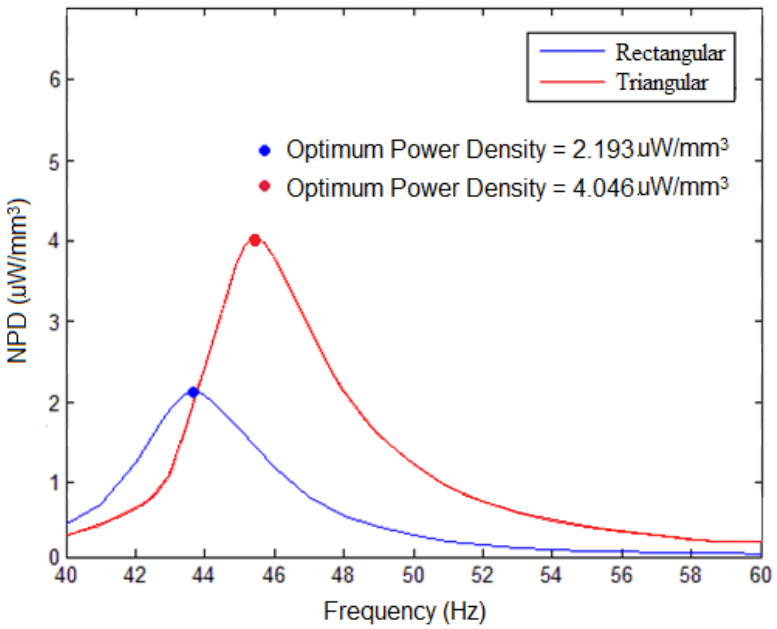

Figure 7.14- Frequency response normalised to the same beam volume

As in Figure 7.14, after normalising the data, the frequency response shows that the triangular bender can provide better power density than the rectangular bender. The Normalised Power Densities (NPD, $\mu W/mm^3$) are obtained as $2.193\mu W/mm^3$ and $4.046\mu W/mm^3$ for the rectangular and triangular bender respectively. Apart from this, it may be noticed that the optimum frequencies for both beams are different. This verifies that geometry structure can be used as an adjustable criterion for natural frequency tuning for the generator system. However, in this case, the resonance frequencies are not the main aspect to consider. In order to improve the clarity of the comparison, Table 7.4 is created to summarise the optimum powers, volume, optimum frequencies and Normalised Power Density (NPD, $\mu W/mm^3$) of the beams.

Beam's shape	**Optimum Power (mW)**	**Beam volume (mm^3)**	**Resonant Frequency (Hz)**	**NPD ($\mu W/mm^3$)**
Rectangular	1.581	721	43.7	2.193
Triangular	0.227	56.1	45.5	4.046

Table 7.4 - Comparison between Triangular and Rectangular beams

7.4 Discussion on alternative geometry of beam structures

From the analysis in the analytical modelling, it indicates that the trapezoidal geometry can definitely supply more energy than the ordinary rectangular geometry for a given volume. Besides, this analytically proved that by changing the width and height of the cantilever beam, the resultant maximum strain can be improved. However, due to the material breakage limit of the bender, alternating the height of the beam is not recommended if the average strain is the main term to be concerned. Added to the above, it is difficult to manufacture a beam with varying height (depth) due to the fact that the current practical commercial benders come in a thin sheet form. On the contrary, though

the maximum strain provided by the beam with width varying is lower than those with height varying, the width varying structure (Structure 3) can provide a better average strain that just slightly falls below the maximum material breakage limit by carefully adjusting the applied driving frequency and amplitude. Furthermore, it is much easier to produce and more cost effective than the height varying structure. Apart from that, it is also worth mentioning that for the application where the maximum strain is the main concern, Structure 5 can be used to replace those height varying cantilever benders by carefully adjusting the curvature along the structure so that the maximum strain value can be achieved. As a conclusion, a triangle width varying beam is still the preferable solution if the average strain is the main concern. On the other hand, if the maximum strain is the primary concern, Structure 5 with a proper curvature adjustment along the beam is preferable over the height varying structures.

From results shown in numerical modelling, Structure 5 provides a better strain distribution if compared to the ordinary rectangular beam (Structure 1), however it still look imperfect if compared to the Structure 3. Plus, the shape of this structure is more difficult to manufacture. For the traditional rectangular beam (Structure 1), 20.45% of its material will have the strain ratio that is more than 0.75 for a given input force. Compared with the solution Structure 3, 68.22% of its material will have the strain ratio that is larger than 0.75 for the same amount of input force. However this is 31.78% less than analytical model (100%). This imperfection is caused by the strain concentration at the fixed end and the inconsistent strain across the width of the cantilever. Nonetheless, though there is an imperfection caused by the practical material behaviour, this still clearly verifies that Structure 3 will be the best solution to improve the power output for vibration-based energy scavengers with alternative geometry structure. The triangular structure can maximize the material's average strain for a given input and improves the scavenger

robustness by reducing stress concentration. With this improvement, both the generator's size and cost can be reduced.

Added to the above, assuming that the average strain ratio is proportional to the maximum power the cantilever could generate without breaking, the comparison in Table 7.2 and Table 7.3 can be further improved by calculating the average strain ($\varepsilon_{\text{average}}$) and normalised strain ($\varepsilon_{\text{normal}}$) as in Table 7.5 and Table 7.6, in which the average strain for the structure is the division of the sum of the strain ratio (given in Equation (7.9)) by the total number of nodes in the structure (η_{total}) as expressed in Equation (7.10); and the normalised strain is the normalised average strain against the analytical structure 1 as given in Equation (7.11).

$$\varepsilon_{total} = \sum_{i=0}^{\eta_{\text{total}}} \varepsilon_{ratio}(i) = \varepsilon_{ratio}(0) + \varepsilon_{ratio}(1) + \cdots + \varepsilon_{ratio}(\eta_{\text{total}}) \tag{7.9}$$

where $\varepsilon_{\text{total}}$ the sum of the strain ratio in the structure

i is the index number of the node in the structure

$\varepsilon_{\text{ratio}}(i)$ is the strain ratio from node i

$$\varepsilon_{average} = \frac{\varepsilon_{total}}{\eta_{total}} \tag{7.10}$$

$$\varepsilon_{normal} = \frac{\varepsilon_{average}}{0.5} \tag{7.11}$$

From Table 7.5, it can be seen that the analytical Structure 3 is the best solution and twice ($\varepsilon_{\text{normal}}$ =2) as good as analytical Structure 1. Followed by Structure 5 and Structure 2 with $\varepsilon_{\text{normal}}$ =1.59 and $\varepsilon_{\text{normal}}$ =1.351 respectively. Lastly, for Structure 4, it suggested that approximately 18.7% extra power can be obtained with this structure analytically compared to Structure 1. On the other hand from, for the non uniform cross

section strain distribution (numerical) models from Table 7.6, it suggests that only 75.4% of the power that predicted by the analytical model is obtained in the numerical model of Structure 3 and only 50.8% extra power can be obtained compared to 100% as suggested by the analytical Structure 3 in Table 7.5.

Beam Structures	**Average Strain ($\varepsilon_{average}$)**	**Normalised Average Strain (against analytical structure 1) (ε_{normal})**
Structure 1	0.5	1
Structure 2	0.676	1.351
Structure 3	1	2
Structure 4	0.594	1.187
Structure 5	0.795	1.590

Table 7.5 – Average and normalised strain (analytical) for the investigated structures

Beam Structures	**Average Strain ($\varepsilon_{average}$)**	**Normalised Average Strain (against analytical structure 1) (ε_{normal})**
Structure 1	0.417	0.835
Structure 2	0.565	1.131
Structure 3	0.754	1.508
Structure 4	0.526	1.052
Structure 5	0.649	1.298

Table 7.6- Average and normalised strain (numerical) for the investigated structures

Lastly in the experimental comparison between the triangular and rectangular beam, it is clearly proved that the trapezoidal geometry can definitely supply more energy (per unit volume) than the ordinary rectangular geometry due the varying of the damping factor and the strain distribution of the beam. Roundy [48] found that with the same volume of lead zirconium titanate (PZT) and an increasingly triangular trapezoidal profile, the strain distribution can be made more even. A trapezoidal geometry can supply twice

the energy (per unit volume PZT) than the rectangular geometry. However in this experiment, less than twice energy was obtained from the triangular profile structure ($\frac{4.046\mu W/mm^3}{2.193\mu W/mm^3} = 1.845$). This may be caused by the imperfectness of the triangular profile of the structure during the shearing process. Apart from the energy varying, it may also be noticed that the geometry of the structure can be used as an adjustable criterion for the natural frequency tuning on a generator system. More resonant frequency shifting methods will be discussed next.

Chapter 8 : Load switching frequency tuning generator

As commonly known, vibration-based energy generator devices will provide the optimum power when their resonant frequency matches the ambient driving frequency. Under many circumstances, the driving frequency is known before the actually energy-scavenging device has been designed. However, in other situations the frequencies present in a particular location may not be well known or may vary over time. For instance, the dominant vibration frequency on a domestic fan changes when the air flow is partially or fully obstructed by an object. Therefore, it would clearly be advantageous to have a single design that operates effectively over a range of vibration frequencies.

Many groups of people are currently working on altering the effective stiffness or effective mass on the vibrating beam to shift the dominant frequency of the system. However, it is worthwhile considering whether changing the effective electrical damping during the oscillation cycle will change the behaviour of the system. In this chapter, a novel load switching method is proposed to switch the electrical damping coefficient at different points during the oscillating cycle. First of all, some overview of load switching frequency tuning will be discussed. This is followed by the design, simulation and experimental works of a load switching electromagnetic generator. Simulation will first be discussed and the models are then developed and validated by comparing the experimental outcomes with the simulated outcomes.

8.1 Overview of load switching frequency tuning

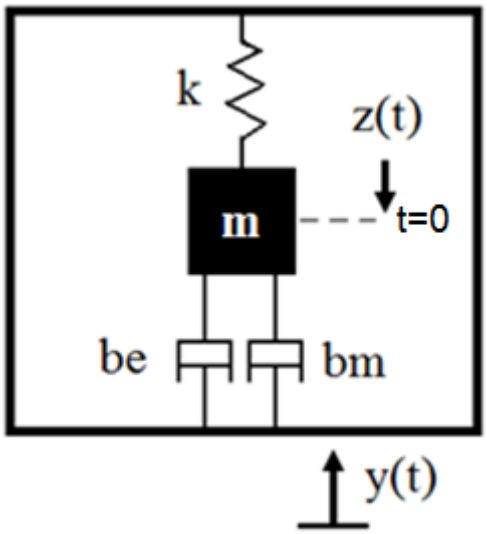

Figure 8.1- Schematic diagram of vibration generator (with electrical damping)

As mentioned previously, a vibration based energy harvester device can be modelled as mass, spring, damper systems of the type illustrated in Figure 8.1. The equations of motion may be then written as:

$$m\ddot{z} + (b_e + b_m)\dot{z} + kz = -m\ddot{y} \tag{8.1}$$

where z is the spring deflection

y is the input displacement

m is the mass

b_e is the electrical induced damping coefficient

b_m is the mechanical damping coefficient

k is the spring constant.

In order to simplify this experiment, an electromagnetic conversion is chosen instead of piezoelectric conversion due to its unsophisticated practical and modelling setup. Figure 8.2 shows a schematic of an electromagnetic generator that will be used in this experiment. One end of the cantilever beam is fixed to the base and copper coils are attached at the other end. Magnets are attached on both side of the panel to create an

electromagnetic effect when the coil in between the magnets oscillates up and down while a driving vibration is applied to the generator.

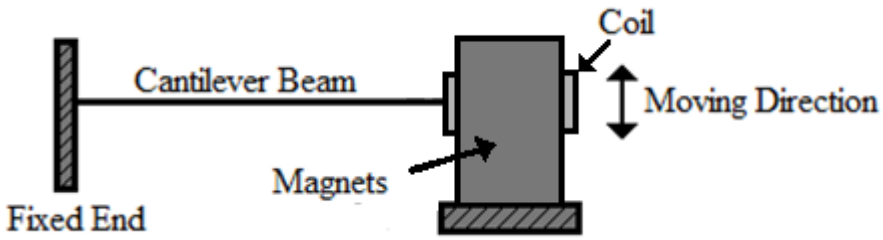

Figure 8.2– Schematic of an electromagnetic energy scavenging device

For electromagnetic conversion device, the voltage generated in a coil due to its motion through the magnetic field (B) may be written as Equation (8.2).

$$v_g = k_e \dot{z} \tag{8.2}$$

$$k_e = BL \tag{8.3}$$

where v_g is the induced open-circuit emf voltage

k_e is the emf constant

B is the magnetic field produced by the magnets

L is the practical coil length

Assuming that the electromagnetic conversion device is connected to a load resistance R_L with the internal coil resistance R_C, and then the voltage drop across the load resistance will become:

$$v_L = \frac{R_L}{R_C + R_L} v_g \tag{8.4}$$

and by simply applying Ohm Law, the current flowing through the coil and load is then:

$$i_{load} = \frac{v_g}{R_C + R_L} \tag{8.5}$$

This current will causes a reaction force in the spring mass system which is equal to $F_e=k_ti$ where k_t is the force constant and $k_t = k_e$. By substituting Equation (8.2) and (8.5) into $F_e=k_ti$, electrical induced damping coefficient b_e can be derived as:

$$b_e = \frac{{k_e}^2}{R_C+R_L} \tag{8.6}$$

From Equation (8.1), the electrical power can be written as Equation (8.7) where A is the amplitude of the acceleration. Where the element ξ_e representing the energy converted to electrical energy and element ξ_m representing the mechanical & parasitic losses and the total damping ratio $\xi_T = \xi_e + \xi_m$. When the vibrating frequency (ω) matches with the resonant frequency (ω_n), the power equation can be further reduced to Equation (8.8).

$$P_{generated} = \frac{m\xi_e A^2(\frac{\omega^2}{\omega_n^3})}{[1-(\frac{\omega}{\omega_n})^2]^2+\left[2\xi_T\frac{\omega}{\omega_n}\right]^2} \tag{8.7}$$

$$\left|P_{generated}\right| = \frac{m\xi_e A^2}{4\omega{\xi_T}^2} \tag{8.8}$$

Total damping coefficient for this model can be derived as $b_T = 2m\omega_n\xi_T$ where $b_T=b_e+b_m$. Therefore, the electrical damping ratio can be written as Equation (8.9). This clearly indicates that changes in damping can be simply accomplished by altering the load resistance R_L.

$$\xi_e = \frac{{k_e}^2}{2m\omega_n(R_C+R_L)} \tag{8.9}$$

After analysing the electrically induced damping ratio term, the switching regimes need to be determined. A number of switching regimes may be considered but because the nonlinear system analysis becomes complex, only a simple case will initially be investigated. Consider the case where the damping is switched according to:

$$b_e = \begin{cases} b_{e1}, & z\dot{z} < 0 \\ b_{e2}, & z\dot{z} \geq 0 \end{cases}$$

where b_{e1} is the electrical damping coefficient for Quadrant I and III

b_{e2} is the electrical damping coefficient for Quadrant II and IV

z is the displacement of the beam

$\dot{z}$ is the velocity of the beam

As depicted in Figure 8.3, when the cantilever is moving downward from its initial resting point, this process is happening in Quadrant II. Follow by Quadrant III when the cantilever moves upward back to the initial resting point from the lowest position. Quadrant IV will then take place when the cantilever moving upward to the highest position and this is followed by Quadrant I when the beam moving back to the initial resting point. This process will keep repeating itself until the vibration source is taken away from the generator device.

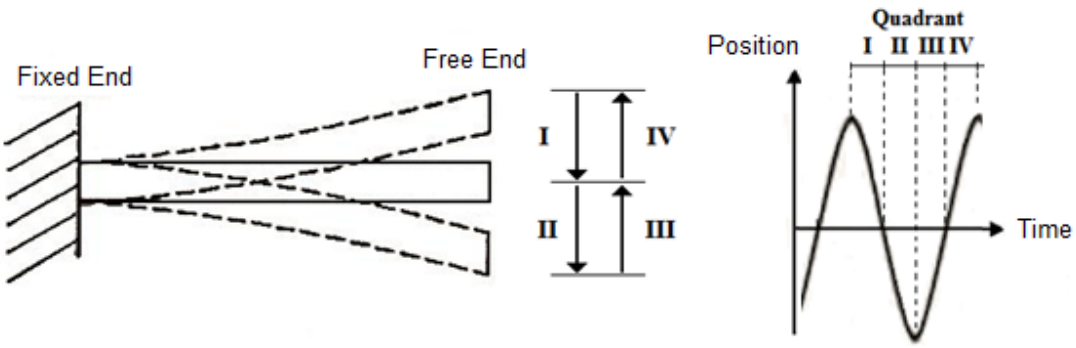

Figure 8.3 - Movement directions of the cantilever beam accordingly to Quadrant number

The quadrants I to IV are illustrated in the motion of the cantilever beam in Figure 8.3. However, this may also conveniently be visualised as phase plane plots as in Figure 8.4.These phase plane plots shows the differences between higher damping, lower damping and switching damping systems for the case where $b_{e1}>b_{e2}$.

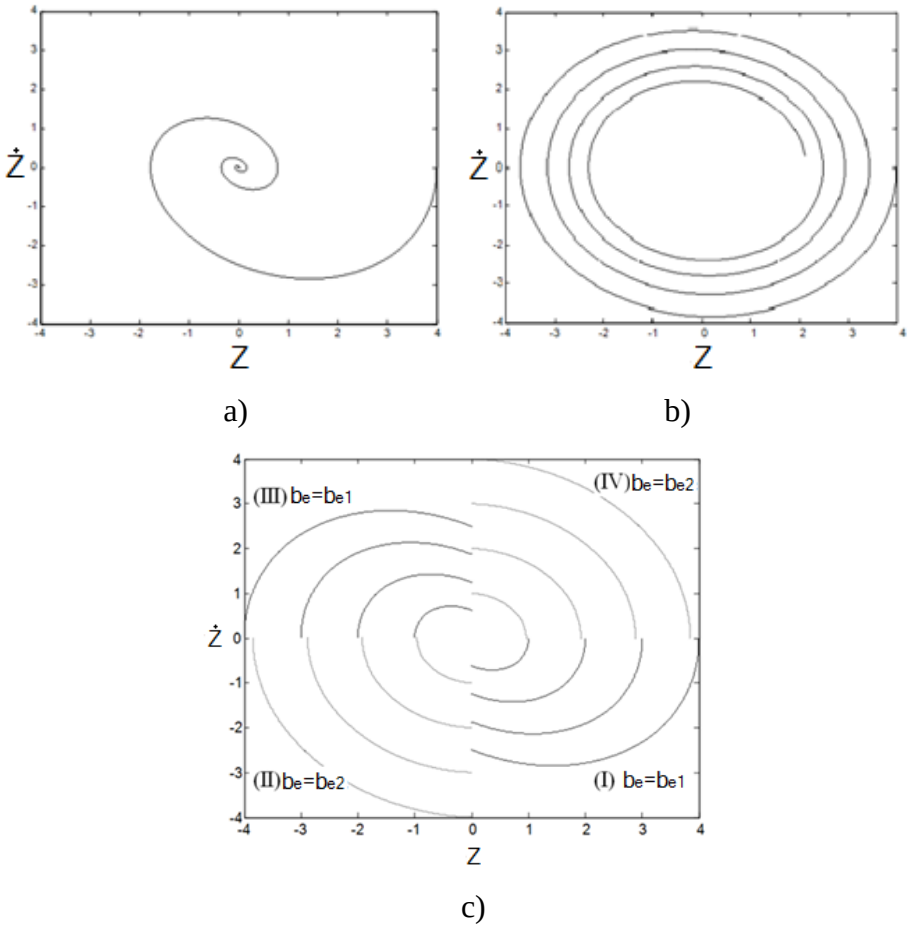

Figure 8.4- Phase plots for switched damping system a) higher damping, b) lower damping, c) switched damping

The feasibility of shifting the natural frequency of the system by changing the effective load of the system during the oscillation cycle can be proved analytically. In order to calculate the natural frequency of this system, the time to complete each quadrant may be calculated in the absence of a driving input. Since the behaviour is the same in quadrants I and III and in II and IV it is only necessary to consider quadrant I $(z > 0, \dot{z} < 0)$ and quadrant II $(z < 0, \dot{z} < 0)$.

Quadrant I

The equations of motion in the absence of an input vibration may be then written as:

$$m\ddot{z}(t) + (b_m + b_{e1})\dot{z}(t) + kz(t) = 0 \tag{8.10}$$

with initial conditions $z(0) = z_0$ and $\dot{z}(0) = 0$ which may solved to give

$$z(t) = z_0 e^{-\omega_n \xi_1 t} \left[\frac{\xi_1}{\sqrt{1-\xi_1^2}} \sin\left(t\omega_n\sqrt{1-\xi_1^2}\right) + \cos\left(t\omega_n\sqrt{1-\xi_1^2}\right) \right] \tag{8.11}$$

where $\omega_n = \sqrt{\frac{k}{m}}$ and $\xi_1 = \frac{b_m + b_{e1}}{2\omega_n m}$

The trajectory leaves quadrant I when z(t)=0 which occurs at a time:

$$t_1 = t|_{z(t)=0} = \frac{\pi - \tan^{-1}\left(\frac{\sqrt{1-\xi_1^2}}{\xi_1}\right)}{\omega_n\sqrt{1-\xi_1^2}} \tag{8.12}$$

Quadrant II

The behaviour in this case may be treated in a similar manner except that b_{e1} in Equation (8.10) is replaced by b_{e2}. The initial conditions are $z(0) = 0,\ \dot{z}(0) = \dot{z}_0$. When the time is starting from zero, the solution for $\dot{z}(t)$ is:

$$\dot{z}(t) = \dot{z}_0 e^{-\omega_n \xi_2 t} \left[\cos\left(t\omega_n\sqrt{1-\xi_2^2}\right) - \frac{\xi_2}{\sqrt{1-\xi_2^2}} \sin\left(t\omega_n\sqrt{1-\xi_2^2}\right) \right] \tag{8.13}$$

where $\xi_2 = \frac{b_m + b_{e2}}{2\omega_n m}$

The trajectory leaves quadrant II when $\dot{z}(t) = 0$ which occurs at the time:

$$t_2 = t|_{\dot{z}(t)=0} = \frac{\tan^{-1}\left(\frac{\sqrt{1-\xi_2^2}}{\xi_2}\right)}{\omega_n\sqrt{1-\xi_2^2}} \tag{8.14}$$

The period, T, for a complete cycle through the four quadrants is:

$$T = 2(t_1 + t_2) = \frac{2}{\omega_n}\left[\frac{\pi - \tan^{-1}\left(\frac{\sqrt{1-\xi_1^2}}{\xi_1}\right)}{\sqrt{1-\xi_1^2}} + \frac{\tan^{-1}\left(\frac{\sqrt{1-\xi_2^2}}{\xi_2}\right)}{\sqrt{1-\xi_2^2}}\right] \tag{8.15}$$

It may be noted that if $\xi_1 = \xi_2 = \xi$ then this simplifies to $T = \frac{2\pi}{\omega_n\sqrt{1-\xi^2}}$ which is the period for a system with fixed damping or $\omega_d = \omega_n\sqrt{1-\xi^2}$ which is the damped natural frequency.

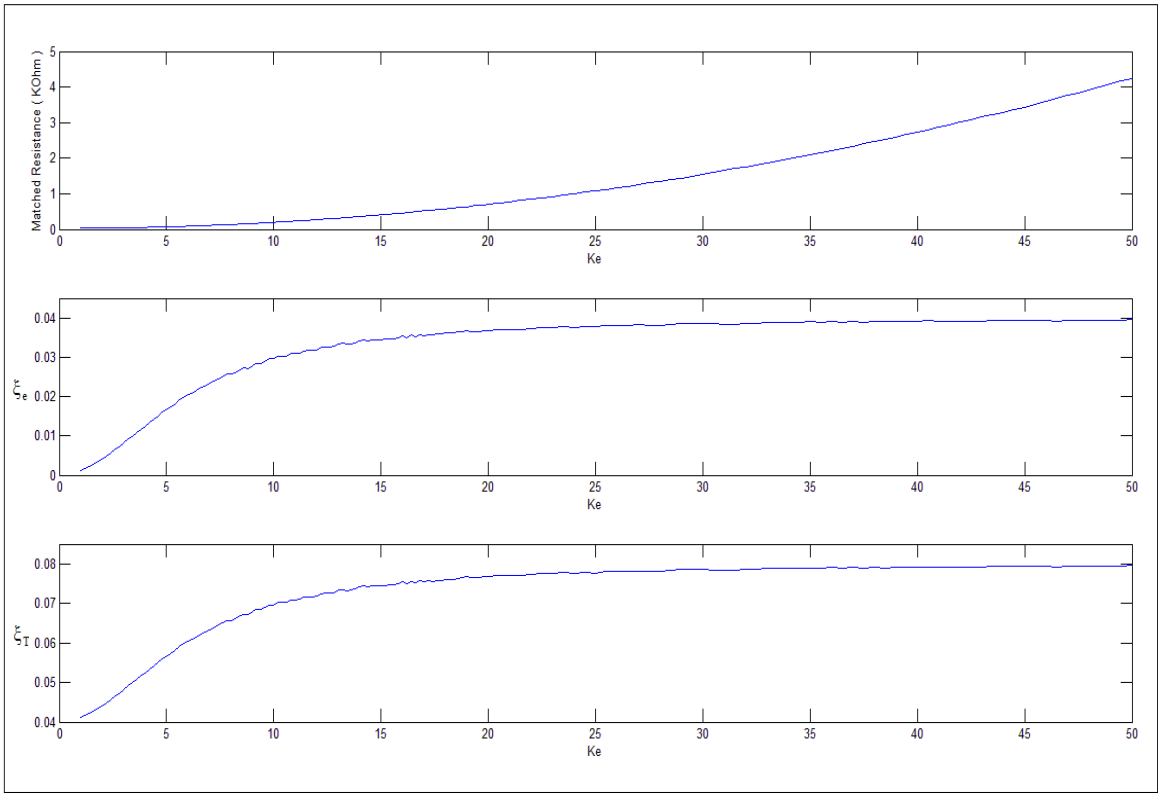

Figure 8.5– Simulated Electro Motive Force constant (k_e) response with a fixed damping

The values for ξ_1 and ξ_2 may be selected in a number of ways. In order to avoid some complex analysis, only a simple case like percentage varying on system matched resistance will initially be considered. However, to do this, the optimum electrical damping ratio (ξ_e) for the fixed damping system need to be determined in advance. A

Simulink model based on Equation (8.1) is used to simulate the system matched resistance ($R_{matched}$) for a given emf constant (k_e) within the range of 1 to 50 N.s/C and a fix constant $\xi_m = 0.04$. This simulation is repeated for a range of values of $R_{matched}$ and the value which give the peak output power identified. The electrical damping ratio (ξ_e) and the system total damping ratio (ξ_T) are then calculated and recorded along with the different k_e. According to the simulated outcome from this designed electromagnetic generator as depicted in Figure 8.5, the electrical damping ratio (ξ_e) will match with the mechanical damping ratio ($\xi_m = \xi_T - \xi_e$) when the system emf constant (k_e) reaches a certain significant level. This effect was fully supported by Roundy [51] as described in Section 2.2 which stated that generated power will be optimum when $\xi_m = \xi_e$. To ensure this happen, the emf constant is assumed relatively high in this case (k_e = 45 N.s/C). However, due to some environment limitations in the practical situation, the pragmatic emf constant will eventually bring the electrical damping ratio down and gives $\xi_{e1} \& \xi_{e2} < \xi_m$. This will be further explained later in this chapter.

By making some slight modifications to Equation (8.9) gives

$$\xi_{e1} = \frac{{k_e}^2}{2m\omega_n(R_C+R_{L1})} \text{ and } \xi_{e2} = \frac{{k_e}^2}{2m\omega_n(R_C+R_{L2})}$$

where R_{L1} is the load resistance to produce ξ_{e1}

R_{L2} is the load resistance to produce ξ_{e2}

R_{L1} and R_{L2} can be then categorized into three cases by properly adjusting the system matched resistance ($R_{matched}$) according to the percentage varying factor (K_R). To further simplify the analysis, the percentage varying factor K_R is chosen as 0%,10%, 20%,30%.....90%.

Case 1 is when $R_{L1} > R_{L2}$, this can be achieved by adding the varying matched resistance to $R_{matched}$ for R_{L1} and deducting it from $R_{matched}$ for R_{L2} as:

$$\text{Load resistances for Case 1} \begin{cases} R_{L1} = R_{matched} + [R_{matched} \times K_R] \\ R_{L2} = R_{matched} - [R_{matched} \times K_R] \end{cases} \quad (8.16)$$

this lead to:

$$\xi_{e1} = \frac{{k_e}^2}{2m\omega_n[R_C + R_{matched} + (R_{matched} \times K_R)]} \quad (8.17)$$

$$\xi_{e2} = \frac{{k_e}^2}{2m\omega_n[R_C + R_{matched} - (R_{matched} \times K_R)]} \quad (8.18)$$

Case 2 is when $R_{L1} < R_{L2}$, this can be achieved by deducting the varying matched resistance from $R_{matched}$ for R_{L1} and adding it to $R_{matched}$ for R_{L2} as:

$$\text{Load resistances for Case 2} \begin{cases} \mathrm{R_{L1}} = \mathrm{R_{matched}} - [\mathrm{R_{matched}} \times \mathrm{K_R}] \\ \mathrm{R_{L2}} = \mathrm{R_{matched}} + [\mathrm{R_{matched}} \times \mathrm{K_R}] \end{cases} \quad (8.19)$$

this lead to:

$$\xi_{e1} = \frac{{k_e}^2}{2m\omega_n[R_C + R_{matched} - (R_{matched} \times K_R)]} \quad (8.20)$$

$$\xi_{e2} = \frac{{k_e}^2}{2m\omega_n[R_C + R_{matched} + (R_{matched} \times K_R)]} \quad (8.21)$$

and finally Case 3 is when K_R=0% and $R_{L1} = R_{L2} = R_{matched}$,

$$\xi_{e1} = \xi_{e2} = \frac{{k_e}^2}{2m\omega_n[R_C + R_{matched}]} \quad (8.22)$$

If the emf constant is assumed relatively high then in Case 3 when $R_L = R_{matched}$, this will lead to $\xi_{e1} = \xi_{e2} = \xi_m$. After deciding the proper way to determine the shifting electrical damping ratios (ξ_{e1} & ξ_{e2}) , the values for ξ_1 and ξ_2 can be then easily obtained by:

$$\xi_1 = \xi_m + \xi_{e1} \tag{8.23}$$

$$\xi_2 = \xi_m + \xi_{e2} \tag{8.24}$$

and the natural frequency for the load switching device will be:

$$\omega = \frac{2\pi}{T} \tag{8.25}$$

The natural frequency derived from Equation (8.15) as a function of R_{L1} and R_{L2} for $\xi_m = 0.04$ is as shown in Figure 8.6. The normalized natural frequency, $\omega_N = \frac{\omega}{\omega_n}$ where ω is the shifted natural frequency and ω_n is the initial natural frequency of the system. All relevant simulated and assumed variables are shown in Table 8.1.

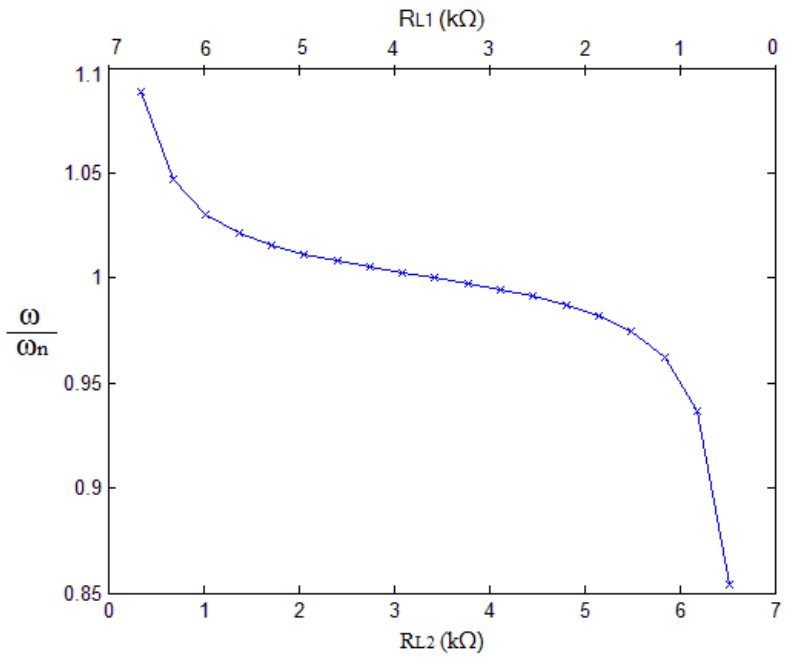

Figure 8.6 - Effect of relative load resistances R_{L1} & R_{L2} on natural frequency

Descriptions	Variables	Simulated* & Assumed values	Units
Load resistance for ξ_{e1}	R_{L1}	343.5 to 6526.5 (*)	Ω
Load resistance for ξ_{e2}	R_{L2}	6526.5 to 343.5 (*)	Ω
Internal coil resistance	R_C	29.2	Ω
System Matched resistance	$R_{matched}$	3435 (*)	Ω
Percentage varying factor	K_R	0 to 90 (step of 10)	%
System mechanical damping ratio	ξ_m	0.04	-
Total damping ratio for load one	ξ_1	0.0608 to 0.4064 (*)	-
Total damping ratio for load two	ξ_2	0.4064 to 0.068 (*)	-
Initial natural frequency	ω_n	248.8	rad/sec
Electro Motive Force Constant	k_e	45(*)	Vs/m
System Spring Constant	k	$4.8x10^{-7}$	Vs/m
System effective mass	m	0.0297	Kg

Table 8.1- Simulated and assumed variables used in the simulation

It may be seen that the natural frequency may be adjusted above or below the natural frequency for the fixed damping system and that a reasonably large range of frequencies can be achieved. To further explain this frequency altering method descriptively, Figure 8.7 shows the phase plots for switched damping system for Case 1(left figure) in which $b_{e1}<b_{e2}$ and Case 2 (right figure) in which $b_{e1}>b_{e2}$. Where d is the distance between point A and point B. Assume that the beam cantilever is moving from point A to point B for both cases. In Case 1, the system will goes into the lower damping quadrant first and then goes into a higher damping quadrant later. On the other hand, in Case 2, the system does it oppositely by going into higher damping quadrant before the lower damping quadrant. It can be seen that although the distance travelled by both system are the same, the average velocity ($\dot{z}$) of Case 1 is higher than the one in Case 2. Therefore, Case 1 required lesser time for the cantilever to travel from point A to point B, meaning that the natural frequency is shifted above the initial natural frequency. On the contrary, for system Case 2, it required a longer time for the cantilever to move from point A to

point B, so the natural frequency is adjusted below the initial natural frequency for the fixed damping system.

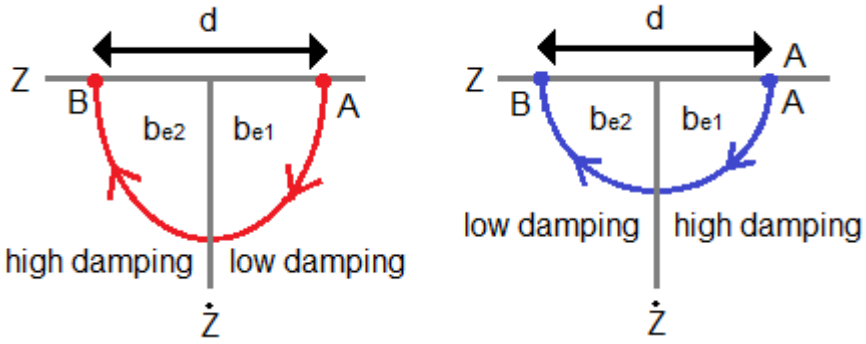

Figure 8.7 - Phase plots for switched damping system Case 1(Left) and Case 2 (Right)

It should however be noted that altering the damping may affect the peak output power as well as the natural frequency. In order to calculate the average power of this system, the energy for each quadrant may be calculated. Similar to the time derivation previously, only quadrants I and quadrant II will be considered here.

Quadrant I

The constitutive equation for the voltage drop across the load resistance was presented as Equation (8.4) in the last section. However, it will be repeated here as Equation (8.26) with R_{L1} as the load resistance for convenience.

$$v_{\mathrm{L}} = \frac{R_{L1}}{R_C + R_{L1}} v_g \tag{8.26}$$

where $v_g = k_e \dot{z}$, is the voltage generated in a coil

For the given v_{L}, the instantaneous power for Quadrant I can be derived as

$$p_{Q1}(t) = \frac{{v_{\mathrm{L}}}^2}{R_{L1}} = \frac{R_{L1}}{(R_C + R_{L1})^2} (k_e \dot{z})^2 \tag{8.27}$$

The displacement solution $z(t)$ was given in Equation (8.11). By differentiating $z(t)$ with respect to *t* gives the $\dot{z}(t)$ solution as:

$$\dot{z}(t) = -\omega_n z_0 e^{-\omega_n \xi_1 t}\left[\frac{\sin\left(t\omega_n\sqrt{1-\xi_1^2}\right)}{\sqrt{1-\xi_1^2}}\right] \tag{8.28}$$

By substituting the $\dot{z}(t)$ into Equation (8.27) gives $p_{Q1}(t)$ as:

$$p_{Q1}(t) = {k_e}^2{\omega_n}^2{z_0}^2 e^{-2\omega_n\xi_1 t}\left[\frac{\mathrm{R_{L1}}}{(\mathrm{R_C}+\mathrm{R_{L1}})^2}\right]\left[\frac{\sin^2\left(\mathrm{t}\omega_\mathrm{n}\sqrt{1-\xi_1^2}\right)}{1-\xi_1^2}\right] \tag{8.29}$$

By integrating Equation (8.29) from *0* to t_1, the energy delivered to the load in this quadrant can be obtained as:

$$E_{Q1} = \int_0^{t_1} p_{Q1}(t)dt = \omega_n {k_e}^2 {z_0}^2\left[\frac{\mathrm{R_{L1}}}{(\mathrm{R_C}+\mathrm{R_{L1}})^2}\right]\left[\frac{1-e^{-\propto_1}}{4\xi_1}\right] \tag{8.30}$$

where $\propto_1 = \frac{2\xi_1(\beta)}{\sqrt{1-\xi_1^2}}$ and $\beta = \pi - \tan^{-1}\left(\frac{\sqrt{1-\xi_1^2}}{\xi_1}\right)$

Quadrant II

Similar to Quadrant I except that $\mathrm{R_{L1}}$ in Equation (8.27) is replaced by $\mathrm{R_{L2}}$ and the solution of $\dot{z}(t)$ from Equation (8.13) is used instead of Equation (8.28). The instantaneous power for Quadrant II can be derived as:

$$p_{Q2}(t) = {k_e}^2{\dot{z}_0}^2 e^{-2\omega_n\xi_2 t}\left[\frac{\mathrm{R_{L2}}}{(\mathrm{R_C}+\mathrm{R_{L2}})^2}\right]\left[\cos\left(t\omega_n\sqrt{1-\xi_2^2}\right) - \frac{\xi_2}{\sqrt{1-\xi_2^2}}\sin\left(t\omega_n\sqrt{1-\xi_2^2}\right)\right]^2 \tag{8.31}$$

By integrating Equation (8.31) from *0* to t_2, the energy in this quadrant can be obtained as:

$$E_{Q2} = \int_0^{t_2} p_{Q2}(t)dt = {k_e}^2 {\dot{z}_0}^2 \left[\frac{\mathrm{R_{L2}}}{(\mathrm{R_C}+\mathrm{R_{L2}})^2}\right]\left[\frac{1-e^{-\propto_2}}{4\xi_2\omega_n}\right] \tag{8.32}$$

where $\propto_2 = \frac{2\xi_2\gamma}{\sqrt{1-\xi_2^2}}$ and $\gamma = \tan^{-1}\left(\frac{\sqrt{1-\xi_2^2}}{\xi_2}\right)$

The total energy, E_T, for a complete cycle through the four quadrants is :

$$E_T = 2(E_{Q1} + E_{Q2}) = \frac{{k_e}^2}{2}\left[\frac{\omega_n {z_0}^2(1-e^{-\propto_1})\mathrm{R_{L1}}}{\xi_1(\mathrm{R_C}+\mathrm{R_{L1}})^2} + \frac{{\dot{z}_0}^2(1-e^{-\propto_2})\mathrm{R_{L2}}}{\xi_2\omega_n(\mathrm{R_C}+\mathrm{R_{L2}})^2}\right] \tag{8.33}$$

And the average power for a complete cycle can be given as:

$$P_T = \frac{E_T}{T} = \frac{\omega_n {k_e}^2}{4}\left[\frac{\frac{\omega_n {z_0}^2(1-e^{-\propto_1})\mathrm{R_{L1}}}{\xi_1(\mathrm{R_C}+\mathrm{R_{L1}})^2} + \frac{{\dot{z}_0}^2(1-e^{-\propto_2})\mathrm{R_{L2}}}{\xi_2\omega_n(\mathrm{R_C}+\mathrm{R_{L2}})^2}}{\frac{\beta}{\sqrt{1-\xi_1^2}}+\frac{\gamma}{\sqrt{1-\xi_2^2}}}\right] \tag{8.34}$$

where the period, *T*, from Equation (8.15) is restructured as Equation (8.35).

$$T = \frac{2}{\omega_n}\left[\frac{\beta}{\sqrt{1-\xi_1^2}} + \frac{\gamma}{\sqrt{1-\xi_2^2}}\right] \tag{8.35}$$

From discussion, Equation (8.34) gives the average power for a complete cycle for a switching system. However, it was derived in the absence of a driving input. With a driving input force, the equation of motion may be then written as:

$$\ddot{z}(t) + 2\omega_n\xi_1\dot{z}(t) + \omega_n^2 z(t) = \mathrm{Y}\sin(\omega t + \phi) \tag{8.36}$$

where ϕ is the phase of oscillation relative to the driving force.

However, it has not proved possible to derive a closed form expression for the power generated using Equation (8.36) due to the complexity of the mathematical solutions. Therefore, it is necessary to resort to numerical simulation (Matlab Simulink) for particular device parameters. The results of these numerical simulations will be discussed later.

8.2 Design, Simulation and Experiment of Electromagnetic Generator

An electromagnetic prototype has been designed using SolidWork CAD software as illustrated in Figure 8.8. The main body of this generator is made up of aluminium to reduce the total weight. The spring steel cantilever beam (53×19×0.9mm) attached has a copper coil as the free end mass. The attached coil is made up by two separate spirals, the first spiral or generating coil (1000 turns) will generate the voltage υ_G for the switching device and the second spiral or sensing coil (1000 turns) will generate another signal (υ_S) for sensing purpose. Groups of Neodymium permanent magnets (25×10×3mm) are fixed at the common base where they can be shifted inward or outward relatively to the coils by altering the distance between the two magnet holders.

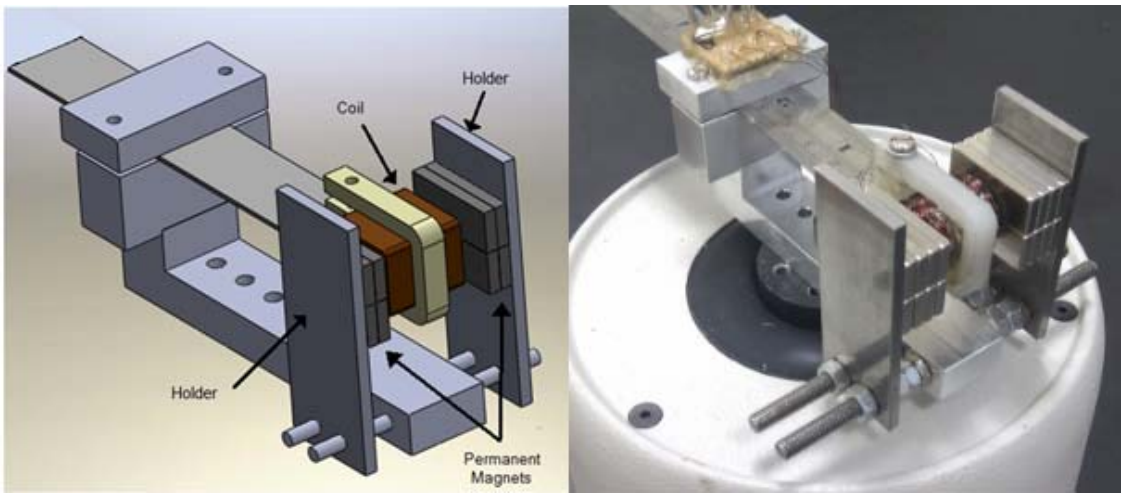

Figure 8.8 - CAD design and the real prototype of an electromagnetic generator

This prototype has a natural frequency of 39.6 Hz and was mounted on the vibrator and driven by magnitude of 0.5g signal within the range of frequencies from 35 Hz (220 rad/sec) to 45 Hz (282 rad/sec). The generated output voltage was measured using a range of different load resistances to determine the matched resistance for the system. The output power was then determined by the general power equation, $P=V^2/R$. Where V is the generated RMS voltage and R is the output load resistance applied to the system. The measured and simulated output power versus load resistance is plotted in Figure 8.9.

The good agreement between experiments and simulations results in Figure 8.9 verifies that the simulation modelling is sufficiently accurate to model the electromagnetic generator. From the plot, it may be seen that the experimental and simulated matched resistance is 74.43Ω and 69.5Ω respectively. By referring to the emf constant (k_e) response in Figure 8.10, the simulated emf constant and electrical damping ratio can be obtained as k_e = 5.2 Vs/m and ξ_e = 0.01761.

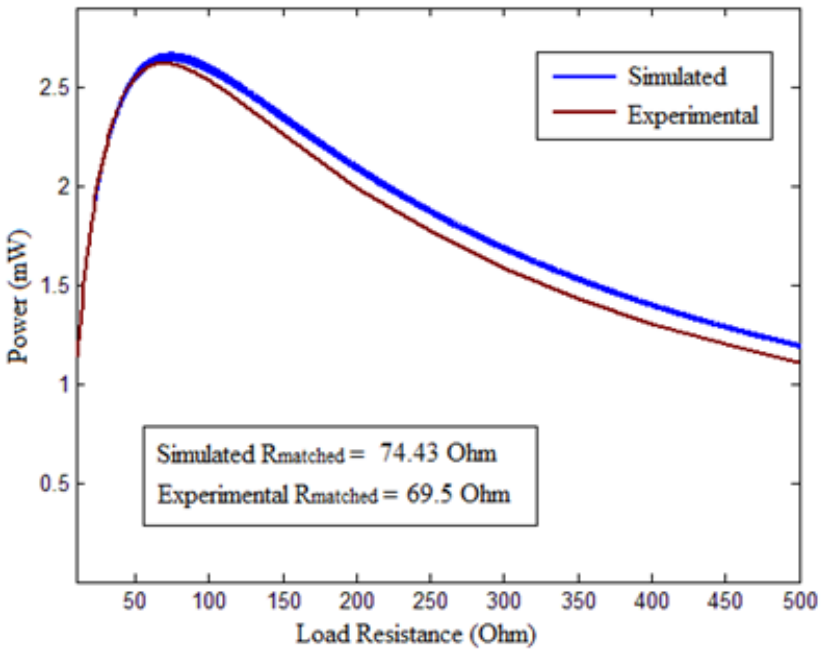

Figure 8.9 – Simulated and experimental output power against resistive load

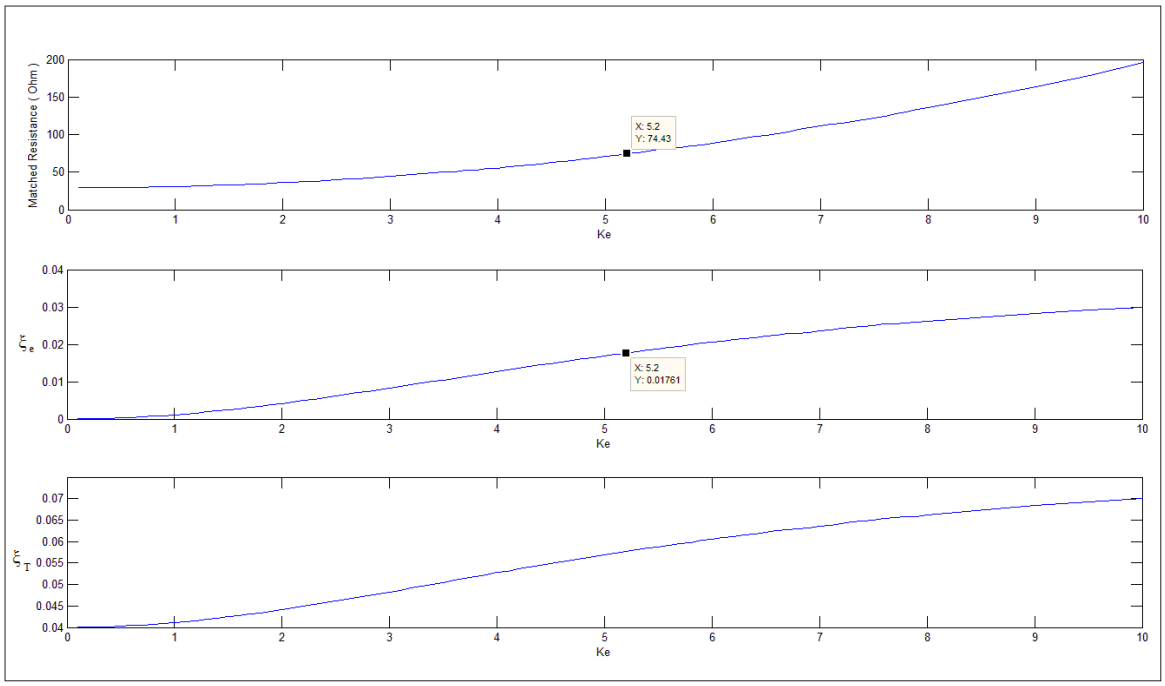

Figure 8.10 - Simulated Electro Motive Force constant (k_e) response with a Fixed damping

The total damping ratio ξ_T and mechanical damping ratio ξ_m were measured as 0.057 and 0.04 respectively with the resistive load resistance of 69.5Ω ($R_{matched}$) for the system. Therefore, the measured electrical damping ratio can be calculated as 0.017 from Equation (8.37). By replacing those values in Table 8.1 into Equation (8.38) except the $R_{matched}$ and ξ_e, the measured k_e is then obtained as 4.988 Vs/m. It indicates that practically the electrical damping ratio will be always less than the mechanical damping ratio ($\xi_e < \xi_m$). This condition is due to the imperfection of the coil having internal resistance (R_c) and the magnetic flux density (B) provided by the permanent magnets. In order to achieve the domain matching condition ($\xi_e = \xi_m$), R_c should be as small as possible ($R_c \rightarrow 0$) and k_e should tend to be very large ($k_e \rightarrow \infty$), which was noted by Stephen [64].

$$\xi_e = \xi_T - \xi_m \tag{8.37}$$

$$k_e = \sqrt{2m\omega_n(\xi_e)(R_C + R_{matched})} \tag{8.38}$$

In order to achieve the quadrants switching practically, an external loads switching device is required along with a switching control system. As depicted in Figure 8.11, a switching device may be constructed by combining two MOSFETs which act as switches. The status of Switch 1 will be controlled by the signal from Drive 1 and the status of Switch 2 will be managed by the signal from Drive 2.

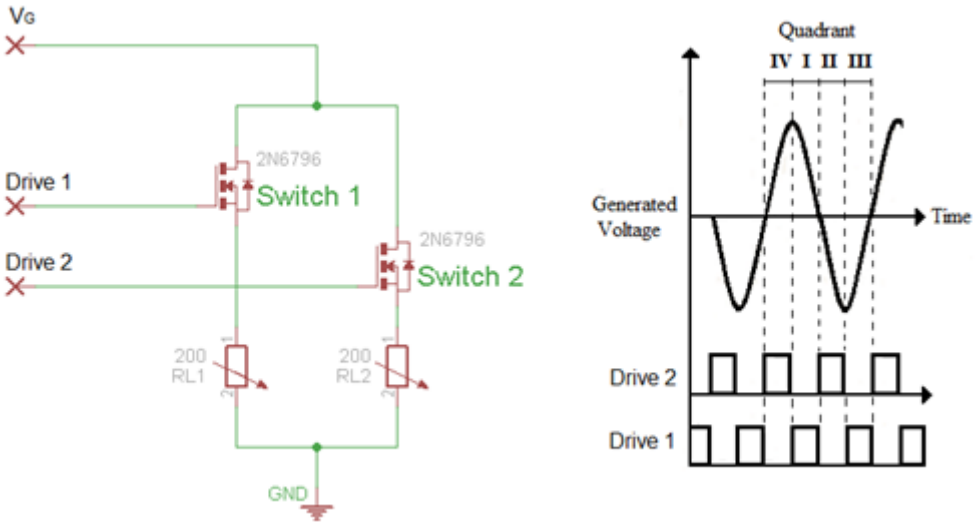

Figure 8.11- Designed switching device

The waveforms on the right hand side illustrate the status of the load resistance during the oscillating cycle. Switch 1 will be turned ON when the signal from Drive 1 is triggered from low to high and this will make the R_{L1} to become the load resistance for Quadrant I and III. On the other hand, the signal from Drive 1 will go low and deactivates Switch 1 at Quadrant II and IV. However, at these quadrants, Drive 2 will then activate the Switch 2 and make R_{L2} as their load resistance. The voltage υ_G (shown as V_G in the figure) is the output voltage generated directly from the generating coil. However, it is worthwhile to mention that a simple resistive load is not a very good approximation of a real electrical load. In reality, the R_{L1} and R_{L2} are needed to be replaced by some power conditioning circuits which provide a constant output voltage. Yet, it is beneficial to begin the modelling in a simple and less complex form before the simulation gets more and more complicated.

As described previously, the load switching device is controlled by two square wave signals (Drive 1 and Drive 2). Therefore, another device is required to provide a real time square wave signal accordingly to the generated voltage from the generator. Figure 8.13 shows the design of real time sinusoidal to square wave's convertor device. This device will take the input from the generator's sensing coil directly as υ_S (shown as V_S in the figure) and converts it into two identical square waves (Drive 1 and Drive 2) that have a 90 degree phase difference. Note that the oscillation of the sensing coil is used rather than the generating coil because the voltage produced by the generating coil varies due to the load switching. These outputs drive the switching device in Figure 8.11 for the purpose of load switching. The fixed voltage supplies device (Figure 8.12) is designed to provide a constant voltage (± 15V, +5V) to ensure that the real time convertor is taking stable power supplies during the conversion processes. The power rating for the voltage supplies device was measured to be 1.35W. Although it seem to be not a good practice to propose an energy harvester that taking more power in the frequency tuning mechanism than the available output power from the generator, at this stage only the feasibility of the concept will be tested. The concept of load switching need to be validated in advance or else a more extensive round of tests would seem to be fruitless. More solutions on this issue will be proposed in the Chapter 9.

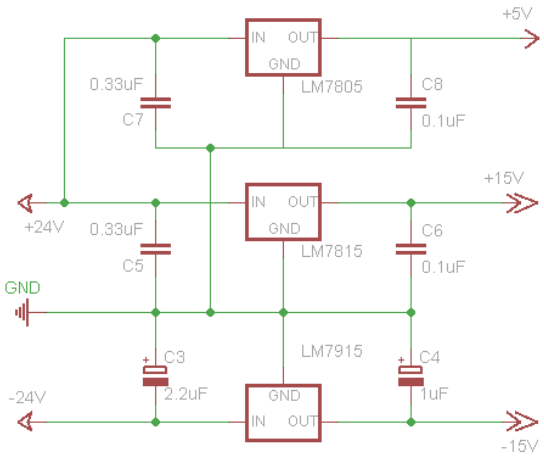

Figure 8.12- Fixed voltage sources supply

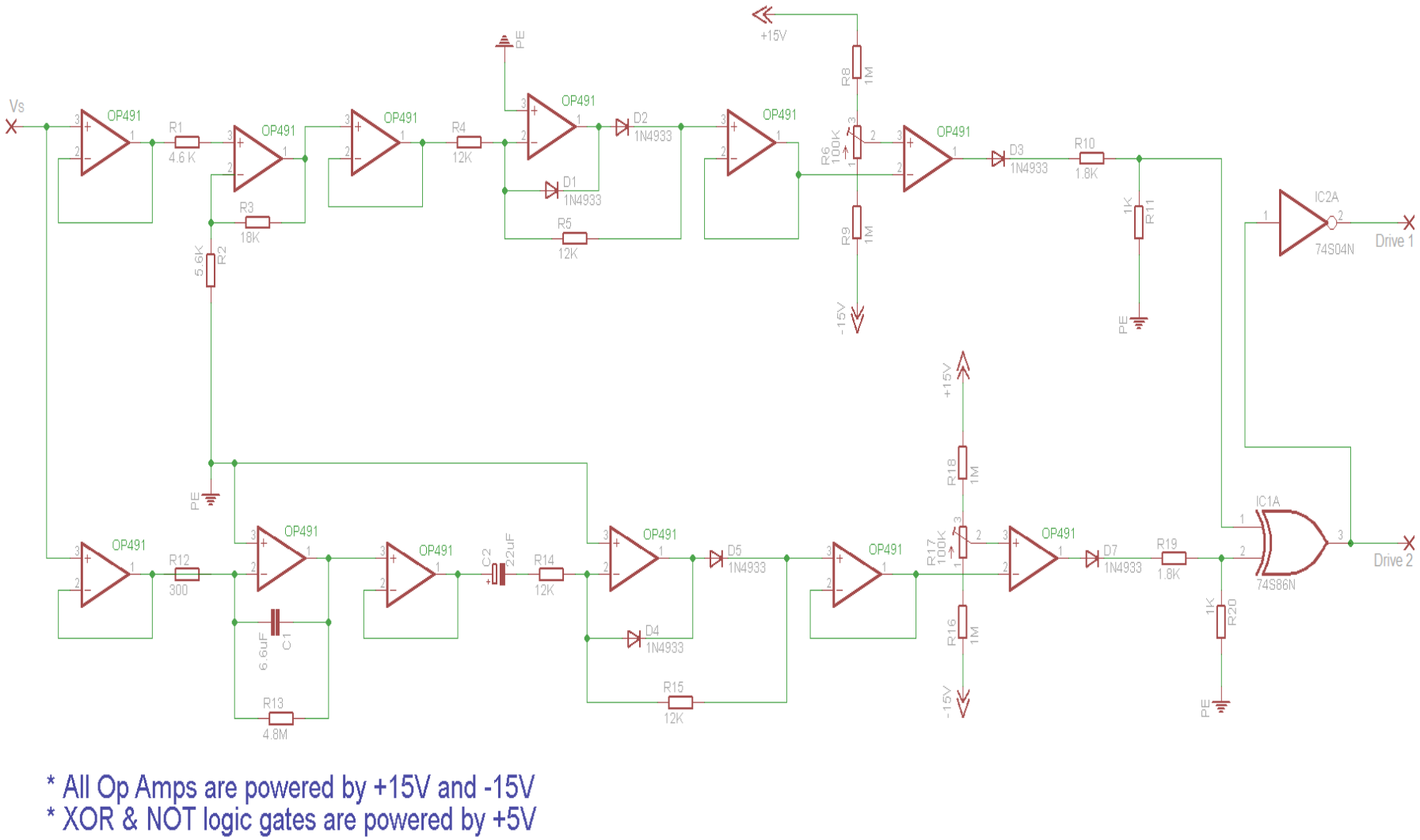

Figure 8.13- Real time sinusoidal to square waves converter device

Figure 8.14 shows the block diagram of the real time sinusoidal to square wave convertor device. As mentioned, it will convert a sinusoidal signal captured from the electromagnetic generator into two identical square waves but with 90 degree phase difference. Therefore in this design, it consists of two convertors. The first one will convert the sinusoidal wave directly into a square wave and the second one will shift the original input signal by 90 degree using an integrator before the square wave conversion. For both cases, the input signal will be amplifier in advance before the precision half wave rectifier to ensure that those signals are rectified accurately. After the rectification, both signals will then be converted to a square wave by a Schmitt Trigger. Lastly, both of them will drive an Exclusive OR logic gate and inverter to create a proper square wave for each quadrant during the oscillating cycle.

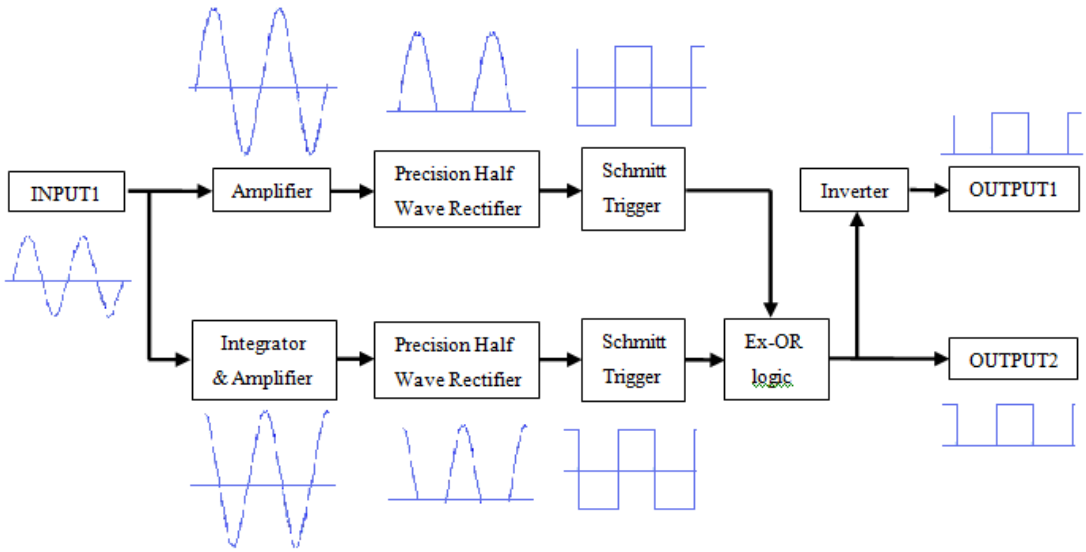

Figure 8.14 – Block diagram for real time sinusoidal to square wave convertor device

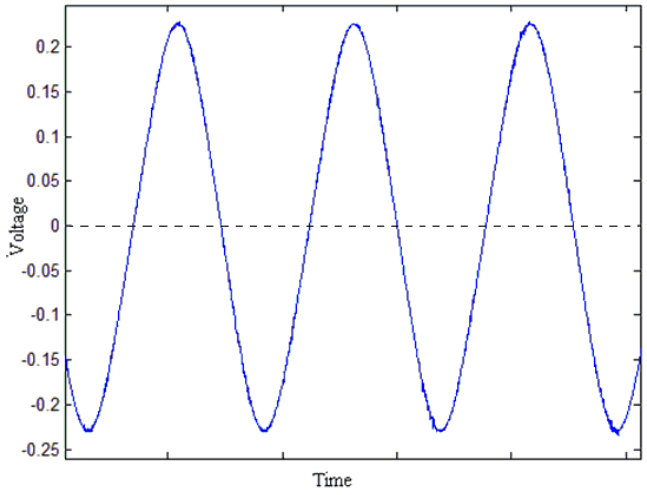

a)Generated voltage for fixed resistive load, R_{L1}=R_{L2} (Case 3)

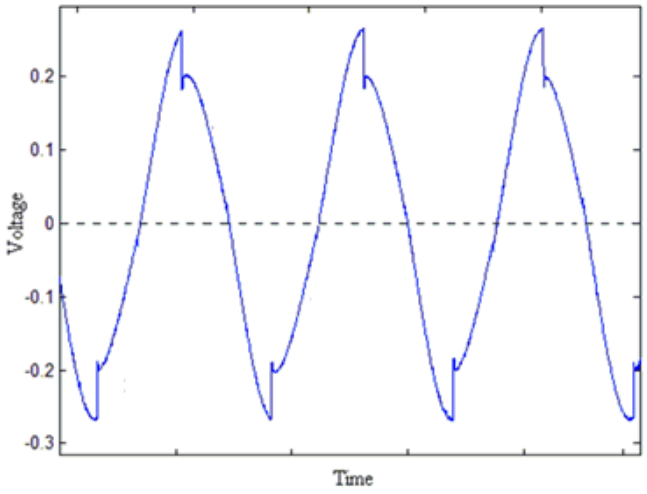

b)Generated voltage for resistive load when R_{L1} < R_{L2} (Case 2)

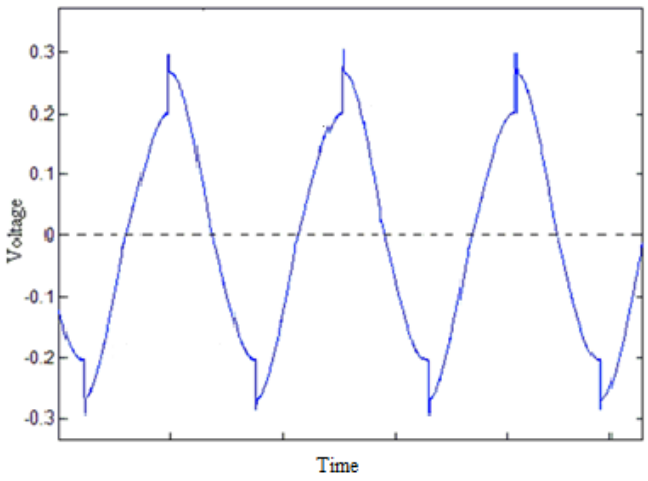

c) Generated voltage for resistive load when R_{L1} > R_{L2} (Case 1)

Figure 8.15 -Generated voltage with different resistive loads

Figure 8.15 represents the voltage generated by the electromagnetic generator for a range of different resistive loads. Figure a) shows the ordinary induced voltage generated from the device if the load resistance is fixed, $R_{L1}=R_{L2}$ (Case 3). For the fixed load, a pure sinusoidal wave is obtained. On the other hand, if the load resistance is switching according to the quadrants, different induced voltage will be obtained as depicted in figure b) when $R_{L1} < R_{L2}$ (Case 2) and Figure c) when the $R_{L1} > R_{L2}$ (Case 1).

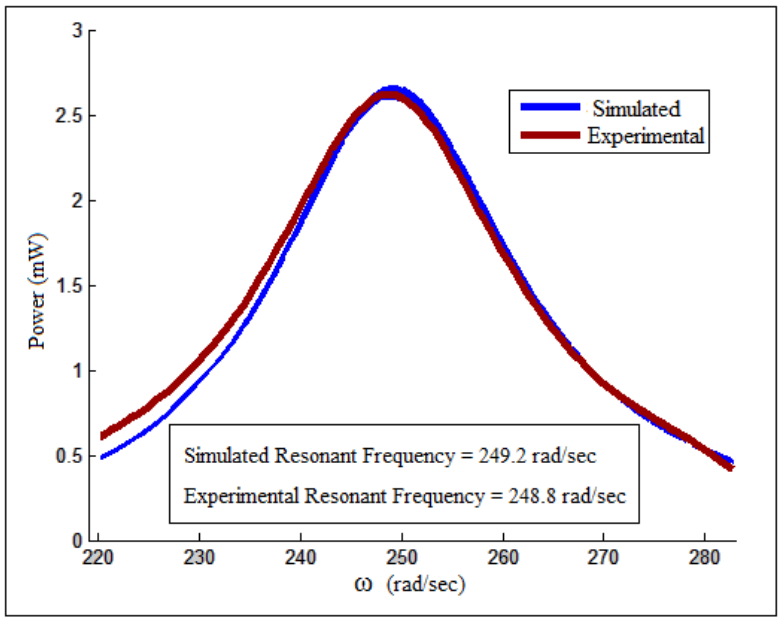

Figure 8.16 – Frequency response with a constant load of 69.5 Ω

In Figure 8.16, it showed the frequency response of the simulated and experimental electromagnetic generator with a constant resistive load of 69.5 Ω (Case 3). The resonant frequency was determined by driving the generator into resonance over a wide range of frequency (220 rad/sec to 282 rad/sec) and the natural frequency for the system was found to be 249.2 rad/sec and 248.8 rad/sec for simulated and experimental respectively. It also indicates that the generated power at frequencies far away from the resonance is significantly lower than the power at the resonant mode. The recorded powers at the resonant mode were 2.67 mW for simulated response and 2.623 mW for the experimental response.

Apart from that, the resonant frequencies and optimum powers for different loads combination in Case 1 and Case 2 is what this experiment concern most. By taking the system matched resistance ($R_{matched}$) as 69.5 Ω, each loads combination in Case 1 and Case 2 can be determined from Equation (8.16) and Equation (8.19) as attached in Table 8.2 . The resonant frequency and optimal power for each different load combination in Case 1 and Case 2 were determined by using the same process as in Case 3 and were recorded for further comparison with the simulated outcome.

K_R (%)	Case 1 ($R_{L1} > R_{L2}$)		Case 2 ($R_{L1} < R_{L2}$)	
	R_{L1} (Ω)	R_{L2} (Ω)	R_{L1} (Ω)	R_{L2} (Ω)
10	76.45	62.55	62.55	76.45
20	83.4	55.6	55.6	83.4
30	90.35	48.65	48.65	90.35
40	97.3	41.7	41.7	97.3
50	104.25	34.75	34.75	104.25
60	111.2	27.8	27.8	111.2
70	118.15	20.85	20.85	118.15
80	125.1	13.9	13.9	125.1
90	132.05	6.95	6.95	132.05
0 (Case 3)	69.5	69.5	69.5	69.5

Table 8.2 – Suggested load resistance for R_{L1} and R_{L2} with different weight on percentage varying factor (K_R)

The comparison of simulation and experimental natural frequency as a function of R_{L1} and R_{L2} is depicted in Figure 8.17. This clearly indicates that both simulation and experimental outcomes have the same behaviour. However it shows that the shifting rate for the resonant frequency is reduced as compared to the previous simulation in Figure 8.6 as a smaller emf constant (k_e) is used in this system. The natural frequency of the system is shifted to a higher value in Case 1 when $R_{L1} > R_{L2}$ and on the contrary the system's resonance is shifted to a lower value in Case 2 when $R_{L1} < R_{L2}$. However, due to the

practical limitation on the resolution of the driving frequency (smallest step = ±0.1Hz), some of the experimental points are obtained at the same frequency. Therefore, to solve this problem, Polynomial curve fitting method is used. Few different order of Polynomial curve fitting has been tested and 3rd order seems to give the best fit for all the points.

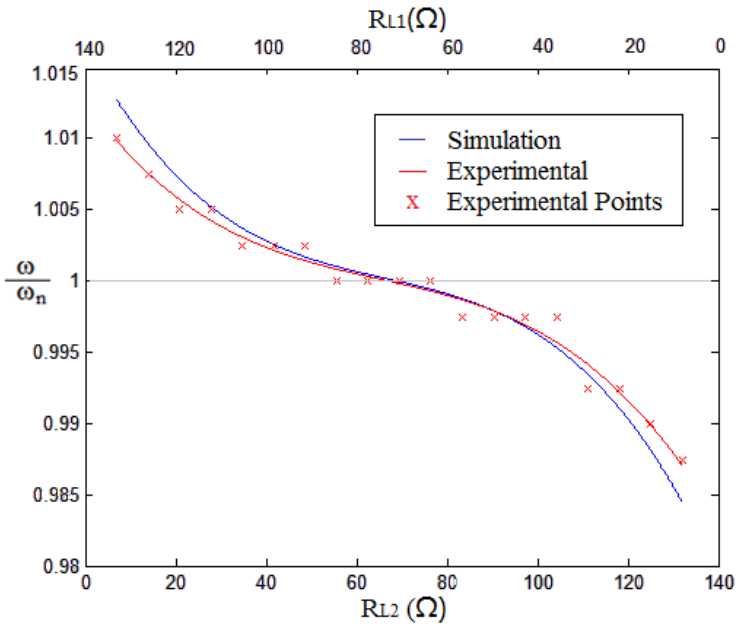

Figure 8.17 –Effect of relative loads resistance R_{L1} & R_{L2} on natural frequency

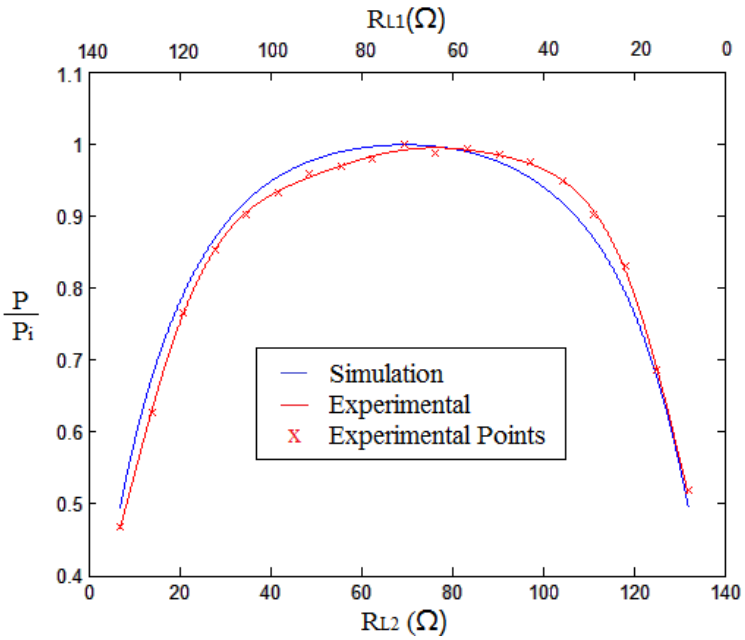

Figure 8.18 – Comparison of the effect of relative load resistance R_{L1} & R_{L2} on output power

It should however be noted that altering the damping will affect the peak output power as well as the natural frequency. In Figure 8.18, it shows the effect of the relative load resistance on the output power for both simulation and experimental. The normalized optimum power, $P_N = \frac{P}{P_i}$ where P is the shifted optimum power and P_i is the initial optimum power of the system. All relevant variables used in this simulation are shown in Table 8.3. In addition, there are practical limitations on the range of values of R_{L1} and R_{L2} which may be used. For instance, the maximum electrical damping is limited by the resistance of the pick-up coil.

Descriptions	Variables	Practical values	Units
Load resistance for ξ_{e1}	R_{L1}	6.95 to 132.05	Ω
Load resistance for ξ_{e2}	R_{L2}	132.05 to 6.95	Ω
Internal coil resistance	R_C	29.2	Ω
System Matched resistance	$R_{matched}$	69.5	Ω
Percentage varying factor	K_R	0 to 90 (step of 10)	%
System mechanical damping ratio	ξ_m	0.04	-
Total damping ratio for load one	ξ_1	0.0504 to 0.0864	-
Total damping ratio for load two	ξ_2	0.0864 to 0.0504	-
Initial natural frequency	ω_n	248.8	rad/sec
Electro Motive Force Constant	k_e	4.988	Vs/m
System Spring Constant	k	4.8×10^{-7}	N/m
System effective mass	m	0.0297	Kg

Table 8.3 – Practical variables used in the simulation

The good agreement between the experiment and simulation outcome verify that the simulation model (based on Equation (8.1)) shown in Figure 8.19 is sufficiently accurate to use for design and optimization purposes. Furthermore, the model can also be used to obtain relatively accurate estimates of the shifted resonant frequency and power generation. For a more details of the Matlab coding and Simulink simulation, consult to Appendix I.

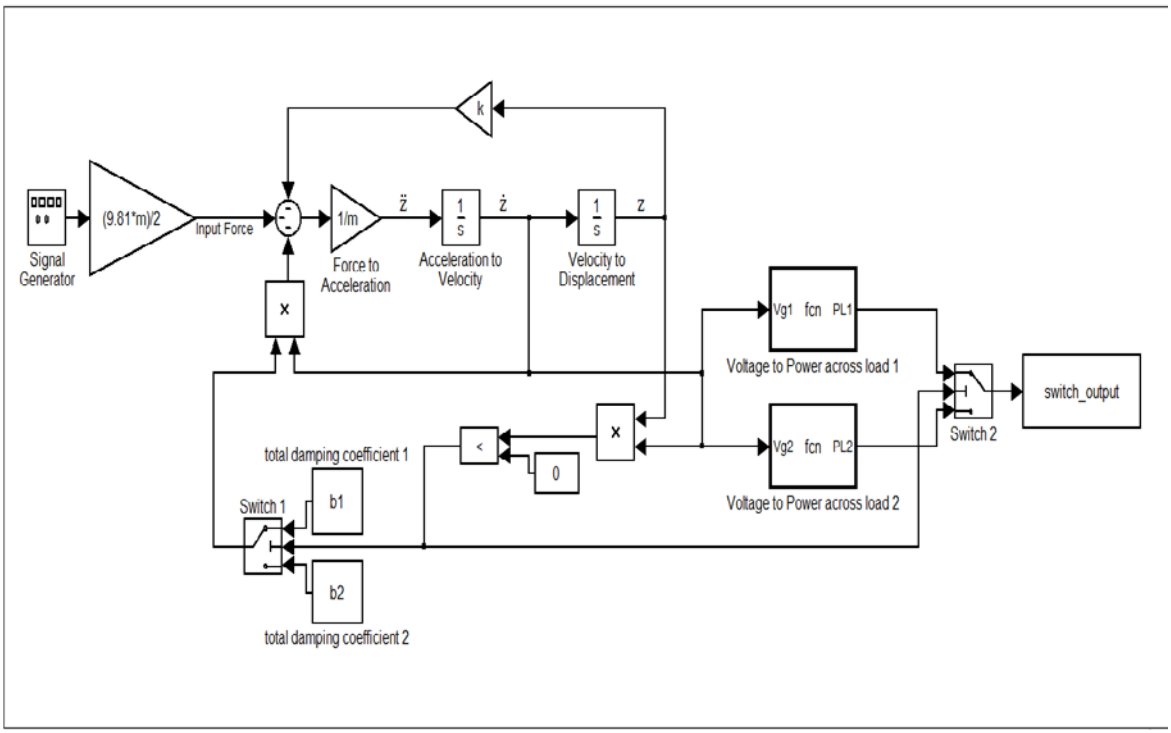

Figure 8.19 – Simulink model for Electromagnetic loads switching generator

8.3 Discussion of Load Switching Frequency Tuning Generator

As mentioned in this chapter, it has been demonstrated that by changing the effective electrical damping during the oscillation cycle it is possible to change the behaviour of the whole system. It may be seen that the natural frequency of the system may be adjusted above or below the initial natural frequency for a fixed damping system. From the simulated plot in Figure 8.20, it can be seen that the range of shifted resonant frequency is related to the emf constant (k_e) and also the percentage varying factor (K_R). Yet, to improve the readability, this plotting only shows the emf constant up to a value of 20Vs/m. This simulated plot clearly shows that the percentage of shifted resonance is dependent to the k_e and K_R, the range of shifted resonant frequency can be improved by increasing the k_e and K_R to theirs practical limit. This indicates that a reasonably large range of shifted resonant frequencies can be achieved by using the load switching frequency tuning method.

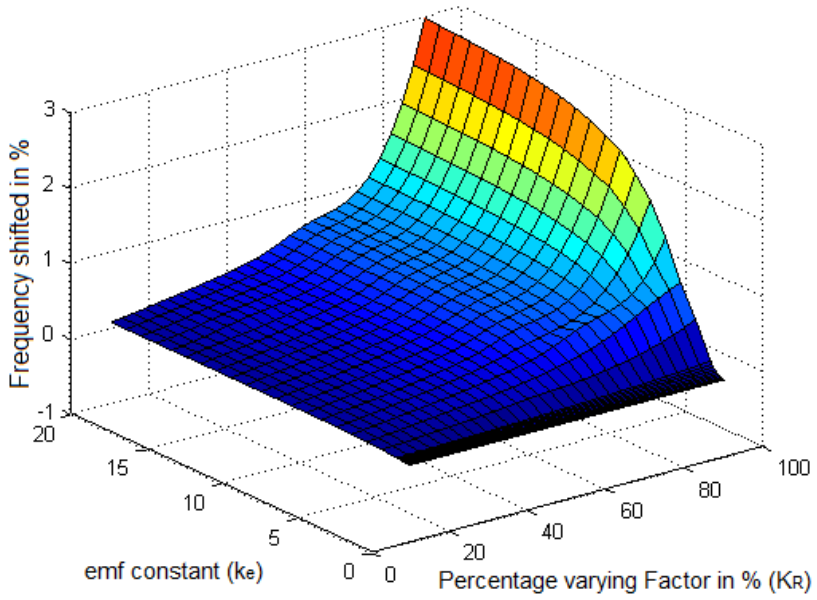

Figure 8.20 - Simulated shifted resonant frequency vs emf constant (k_e) and percentage varying factor (K_R)

Nevertheless, as commented previously, the peak output power will be affected as well as the natural frequency by altering the electrical damping of the system. Figure 8.21 indicates the power loss in percentage versus emf constant (k_e) and percentage varying factor (K_R). Unfortunately, by increase the K_R of the system the power loss for the system will rise as the end effect. However, the percentage of the power loss will be fixed for each step of the K_R regardless of k_e when the latter exceeds a certain value. This implies that there is a maximum limitation for the power loss in this system. As a result, by altering the electrical damping of the system a reasonably large range (±1%) of resonant frequency can be achieved with a fixed maximum power loss on the condition that a greater value of k_e is achievable practically.

There are always some practical limitations on the emf constant k_e. As stated in Equation 8.3, k_e is limited by the coil length and the permanent magnetic field strength. The magnetic field can be increased by using multiple-layer of permanent magnets, as in this experiment there are 3 layers of permanent magnets used on both side of the pick-up coil. On the other hand, the coil length can be practically increased by increasing the

number of turn of the pick-up coil. However, this will eventually increase the coil resistance for the circuit which will reduce the maximum limitation for the electrical damping. Added to the above, increasing the number of turn of the coil will eventually increase the area of coil as the end result. This will require a bigger magnet to be used in the generator and the generator will become less cost efficient. Therefore, to increase the k_e, a thinner super-conductor is suggested to be used in the pick-up coil instead of increasing the number of turn of the coil.

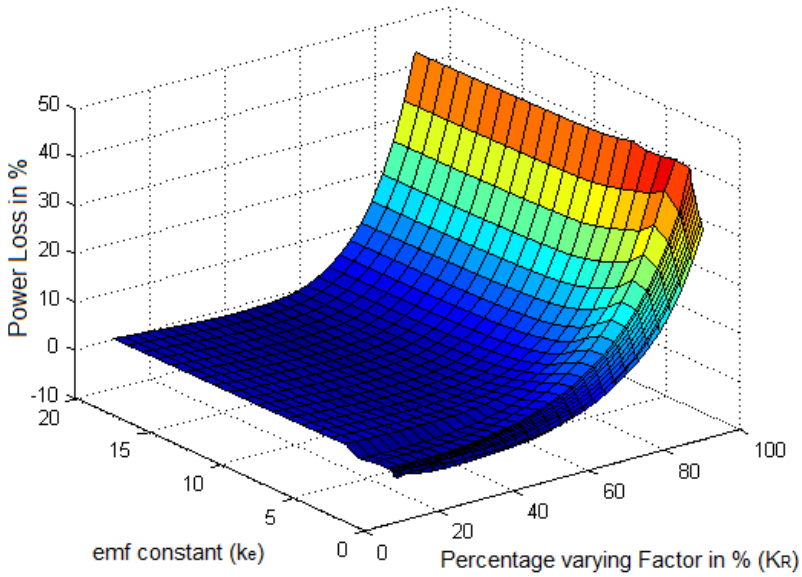

Figure 8.21- Simulated power loss vs emf constant (k_e) and percentage varying factor (K_R)

Chapter 9 : Conclusions and Future work

This work mainly aimed to assess the feasibility of changing the system natural frequency by applying different effective electrical damping to the system in different quadrants of the oscillation cycle. Some reviews of possible energy sources were performed and vibration-based energy was chosen as the main focus area for this research. Three main vibration-based conversion mechanisms were reviewed, but only piezoelectric and electromagnetic were selected for further consideration. Brief histories of piezoelectric materials and electromagnetic harvesters were given, followed by the fundamental information on the conversion mechanism in term of vibration-to-electricity energy. Literature reviews of research done in both piezoelectric and electromagnetic harvesters were presented. Previous achievements and methods of capturing or harvesting the vibration energy for both conversion mechanisms were presented separately, followed by some discussions on other methods of tuning the natural frequency of the energy harvesters by some others research groups in recent years.

Next, two methods to capture the ambient vibration information from various domestic appliances were presented. The behaviour of the ambient vibration was studied and the obtained information was then converted into a useful form. That information was then used to generate replica signals for further use in subsequent simulation and experiments. These two methods were Oscilloscope capturing and DAQ capturing. The earlier was method seen to be more flexible and mobilizable and the latter method seen to be more straight forward in term of the capturing process and programming algorithm.

Some of the piezoelectric bimorph tests had been carried out to validate the effect of the frequency response when the load resistance, frequency and mass placed at the free end were changed respectively. With the varying resistance experiment, the optimum

power will be obtained when the load resistance matched with the impedance of the piezoelectric bender. An analytical model (Equation (6.1)) suggested by Roundy[51] was used as the basic for simulation and the result was experimentally validated by the author. The optimum load resistance was obtained as 25kΩ from analytical model with 0.621mW generated power and 33kΩ from the author's experiments with 0.53mW generated power. In the frequency varying tests, results showed that maximum output power will be generated by the beam when the driving frequency of the vibrator matches the natural frequency of the energy harvester device. The generated power at the dominant frequency was significantly higher than the power generated when the frequency falls further away from the natural frequency of the device. Some frequency responses obtained from the analytical model (Equation (6.3) & (6.4)) were experimentally validated and compared. The results showed the good agreement between the simulation and experimental model. Apart from that, it is worth mentioning that the natural frequency can be tuned by altering the output load, which will eventually change the effective damping coefficient of the system. Finally, the end mass changing method was experimentally validated. With different masses place at the free end of the bender, there is a change in the resonance frequency for the system. Results confirmed that with an increase in the weight of the end mass (from 4.1gram to 6.41gram), the resonance frequency of the system will decrease approximately 5.5Hz when the weight was increased by around 0.77gram and vice versa. Added to the above, it can be seen that the generated power can be improved by increasing the effective mass (m_{eff}) of the system, which was well model by Equation (2.8) in Chapter 2.

The alternative geometry structures of the cantilever bender were next introduced to improve the generated power density from the harvester. All experimental structures were compared in both analytical and numerical methods. The models created by ANSYS

showed that the strain across the width of the cantilever was not constant as assumed in the analytical modelling. However, it showed that there was always a region of material that was highly strained located next to the fixed end of the cantilever beam structure. Furthermore, this concentration will limit the allowable maximum strain applied on the cantilever, reducing the allowable average strain produced by the beam. The resultant data from both platforms demonstrated that the triangular structure provided the best strain distribution (most evenly distributed form) on the cantilever beam and this will lead to a higher output power for a given input force. Besides, a test on finding out the feasibility of improving the energy density from the cantilever bender by changing the beam's depth (height) was carried out analytically. It was found that varying the beam's depth was not the best way to improve the mechanical strain distribution if the average strain from the beam was the main term to be concerned. Added to the above, it was less cost efficient to produce a depth varying beam than the width varying beam structure. Therefore, the triangle width varying beam was still the preferable solution if the average strain was the main concern. Lastly, outputs from a real rectangular and triangular piezoelectric bender were compared to verify the outcome. It revealed that a triangular beam provided a higher energy density (NPD=4.046$\mu W/mm^3$) than the ordinary rectangular beam (NPD=2.193$\mu W/mm^3$).

Finally, novel load switching methods were proposed to verify the feasibility of tuning the dominant frequency of the energy harvester device using a fast load switching concept. The concept of applying a different effective electrical damping into the system at different oscillating quadrant was discussed and the feasibility of tuning the resonant frequency by applying a different load during different quadrants of the oscillating cycle was analytically proved in Figure 8.6. A prototype electromagnetic load switching generator has been developed and the analytically simulated results are verified

experimentally. Both analytical and experimental results confirmed that this method can adjust the system's natural frequency above or below the initial natural frequency for a fixed damping system. The experimental results from Figure 8.17 showed the resonant frequency can be shifted around 1% above or below the initial resonance dependant on the system percentage varying factor (R_v) at the emf constant k_e=4.988Vs/m. . However the range of the shifted frequency was highly related to the emf constant (k_e) which can only be increased to certain level of value due to practical limitations. It should however be noted that altering the load during the oscillation may affect the peak output power as well as the natural frequency but it has not proved possible to derive a closed form expression for the power generated using an input driven motion equation for this switched damping system. Therefore, it is necessary to resort to numerical simulation for particular device parameters. The lack of an analytical solution means that there is limited insight into methods which might make it is possible to tune the frequency using load switching without sacrificing output power.

9.1 Recommendations for future work

From the experience of this research, several suggestions for future work can be recommended.

- In the piezoelectric converter modelling, many variables were assumed and taken from the product datasheet directly. To more accurately describe the models, those variables could be measured experimentally.
- In the alternative geometry test, in order to simplify the modelling, a single layer piezoelectric (5A4E) was chosen as the property for the simulation. However, a bimorph piezoelectric material could behave differently due to the difference of their

Poisson's ratio. In order to improve the resultant outcome, a multi-layer piezoelectric beam property can be included into the simulation.

- As discussed in Chapter 8, the power required to perform the tuning mechanism, P_{tuning}, is reported as 1.35W which is not suitable for any energy harvester device. It is commonly known that for any adaptive/frequency tuning energy harvester, the power required to perform the tuning mechanism (P_{tuning}) must be less than the available power from the generator which results in a net output power. However as mentioned; only the feasibility of this concept has been investigated by the author. As the modelling and experiment presented here do validate that this concept is feasible, therefore further extensive tests are required in order to minimise the P_{tuning}. Some suggestion proposed by the author are as below:
    1) Replace the load tuning device as in Figure 8.13 with a more efficient CMOS circuitry device (typical power consumption only up few milliWatt).
    2) Or replace it with an extreme low power microcontrollers (up to few nanoWatt)
- As in the fast load switching device, the loads on both switches were controlled by two manually tuned variable resistors. Therefore, the resultant resistive load could be less precise. To improve the flexibility and precision of the resistive loads, a digital potentiometer could be used. A microcontroller could be then programmed to control the digital potentiometer in order to provide a desired resistive value to the device while the switching process takes place. Apart from that, a microcontroller can be also used to control the switching process.

$$b_e = \begin{cases} b_{e1}, & z\dot{z} < 0 \\ b_{e2}, & z\dot{z} \geq 0 \end{cases}$$

Instead of switch the damping according to the simple form, a more complicated switching function could be performed by the microcontroller switching controller. One of the examples is depicted as in Figure 9.1. A number of variations on these switching regimes may be envisaged, but it is not clear how these would offset the resonant frequency or the generated power. Nevertheless, the above analysis is based on a simple resistive load which is no very realistic approximation of a real electrical load. In reality, the electrical system would be something like a DC-DC converter or capacitor storage which acts like a variable resistance. Yet, it is beneficial to start up modelling in a simple and less complex form before carry out a more sophisticated model.

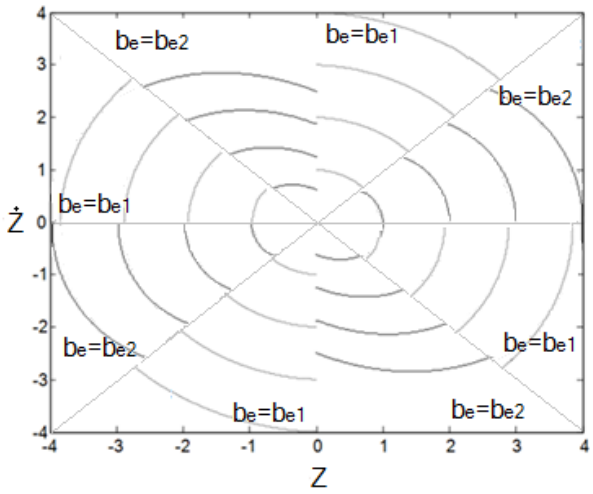

Figure 9.1- Suggested switching phase plane

- After verifying the behaviour of the pure resistance circuit in the load switching device, it is worthwhile to investigate the behaviour of the system when an inductor (L) and/or a capacitor (C) have been added as the load, as in the circuit illustrated in Figure 9.2. In this case, the effective inductance (X_L) and capacitance (X_C) of the system will be switched accordingly to the oscillating cycle instead of the resistive load. It is believed that different kinds of frequency response will be obtained from this switching system because of the behaviour provided by the capacitor and inductor components. In a

capacitor, the current is 90 degrees ahead of the voltage in phase; on the other hand, the current through an inductor lags behind the voltage by a phase angle of 90 degrees. Both impedances are also frequency dependent as the impedance of the capacitor, $X_C = \frac{1}{\omega C}$, and impedance of the inductor is $X_L = \omega L$, where ω = 2πf.

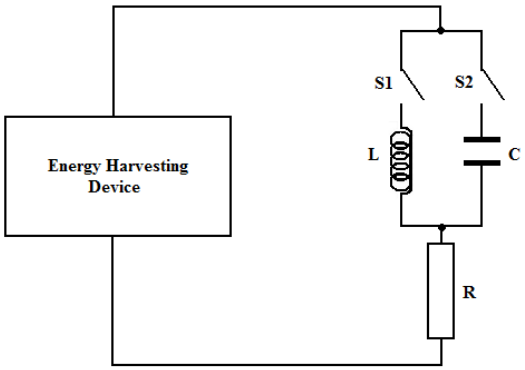

Figure 9.2- Concept of LRC circuit connected to the energy harvesting device

- After the load switching system has been verified using the improved method mentioning above, this idea can be then implemented in a piezoelectric converter and the behaviour of the circuit could be investigated in minute detail. The behaviour of these piezo based system are more complex since the piezo material itself is modelled as a 3rd order system and so it cannot be visualised in the 2D phase planes used in Figure 9.1. Similarly, the LC fast switching design too could be applied to the piezoelectric converter if it performs outstandingly in the electromagnetic converter and is proven that it is worthwhile to do so.

Chapter 10 References

[1] **Agah M, Baek k and Potkay J A** Design and Analysis of a Piezoelectric Vibration Powered Microgenerator System [Article] // ME 553 University of Michigan. - 2002.

[2] **Amirtharajah R and Chandrakasan A P** Self-powered signal processing using vibration-based power generation [Article] // IEEE J. Solid-State Circuits. - 1998. - 33. - 687-695.

[3] ANSYS,Inc [Online]. - http://www.ansys.com/.

[4] **Baker J, Roundy S and Wright P** Alternative Geometries for increasing power density in vibration energy scavenging for wireless sensor networks [Article] // Porc. 3rd Int. Energy Conversion Engineering Conf. (San Fancisco). - 2005. - p959-70.

[5] **Bedekar Vishwas, Oliver Josiah and Priya Shashank** Pen harvester for powering a pulse rate sensor [Article] // Journal of Physics D: Applied Physics. - 2009. - 9pp : Vol. 42.

[6] **Beeby S P [et al.]** A micro electromagnetic generator for vibration energy harvesting [Article] // Journal of Micromechanics and Microengineering. - 2007. - 7. - 1257 : Vol. 17.

[7] **Beeby S P [et al.]** Design and performance of a microelectromagnetic vibration-powered generator [Article] // Actuators and Microsystems. - 2005. - pp780-783 : Vol. 1.

[8] **Beeby S P [et al.]** Micromachined silicon Generator for Harvesting Power from Vibrations [Journal]. - Seoul,Korea : Proc. Transducers, 2005. - pp 780-3.

[9] **Beeby S P, Tudor M J and White N M** Review Article-Energy harvesting vibration source for microsystems applications [Article]. - 2006. - R175-R195 : Vol. 17.

[10] **Benham P P, Crawford R J and Armstrong C G** Mechanics of Enginering Materials [Book]. - [s.l.] : Prentice Hall, 1997. - Vols. [ISBN: 0-582-25164-8].

[11] **Bin Yang [et al.]** Electromagnetic energy harvesting from vibrations of multiple frequencies [Article] // Journal of Micromechanics and Microengineering. - 2009. - 8pp : Vol. 19.

[12] **Challa V R [et al.]** A vibration energy harvesting device with bidirectional resonance frequency tunability [Article] // Smart Materials and structures. - 2007. - 015035 (10pp) : Vol. 17.

[13] **Cho J [et al.]** Optimization of electromechanical coupling for a thin-film PZT membrane: I Modeling [Article] // J. Micromech. Microeng.. - 2005. - 1797-1803 : Vol. 15.

[14] **Cho J [et al.]** Optimization of electromechanical coupling for a thin-film PZT membrane: II Experiment [Article] // J. Micromech. Microeng. - 2005. - 1804-1809 : Vol. 15.

[15] **Cottone F, Vocca H and Gammaitoni L** Nonlinear Energy Harvesting [Article] // Phys. Rev. Lett.. - 2009. - 8 : Vol. 102.

[16] **Donelan J M [et al.]** Biomechanical Energy Harvesting: Generating Electricity During Walking with Minimal User Effort [Article] // Science. - 2008. - pp807-810 : Vol. 319.

[17] **Eichhorn C, Goldschmidtboeing F and Woias P** Bidirectional frequency tuning of a piezoelectric energy converter based on a cantilever beam [Article] // J. Micromechanics and microengineering. - 2009. - 6pp : Vol. 19.

[18] **El-hami M [et al.]** Design and fabrication of a new vibration-based electromechanical power generator [Article] // Sensors and Actuators. - 2001. - A92. - 335-342.

[19] Engineering Mechanics [Online] // Pure Bending. - 25 July 2010. - http://emweb.unl.edu/negahban/em325/11-Bending/Bending.htm.

[20] **Ferrari M [et al.]** Improved energy harvesting from wideband vibrations by nonlinear piezelectric converters [Article] // Procedia Chemistry. - 2009. - 1. - pages 1203-1206 : Vol. 1.

[21] **Gilbert J M and Balouchi F** Comparison of Energy Harvesting Systembs for Wireless Sensor Netowrks [Article] // International Journal of Automation and computing. - 2008. - 4. - 334-347 : Vol. 5.

[22] **Glynne-Jone P [et al.]** An electromagnetic, vibration-powered generator for intelligent sensor systems [Article] // Sensors Actuators. - 2004. - A110. - 344-9.

[23] **Goldschmidtboeing F and Woias P** Characterization of different beam shapes for piezoelectric energy harvesting [Article] // Journal of micromechanics and microengineering. - 2008. - 7pp : Vol. 18.

[24] **Gonzalez J L, Rubio A and Moll F** Human Powered Piezoelectric Batteries to Supply Power to Wearable Electronic Devices [Article] // International Journal of Society of Materials Engineering for Resources. - 2001. - 1. - p34-40 : Vol. 10.

[25] **Jiang S [et al.]** Performance of a piezoelectric bimorph for scavenging vibration energy [Article] // Smart Materials and Structures. - 2005. - 769-774 : Vol. 14.

[26] **John Walko** EETimes.com [Online] // Nokia working on energy-harvesting handset. - 6 November 2009. - 18 June 2010. - http://www.eetimes.com/electronics-news/4195530/Nokia-working-on-energy-harvesting-handset.

[27] **Kymissis J [et al.]** Parasitic Power Harvesting in Shoes [Article] // Proceedings of the 2nd IEEE International Symposium on Wearable Computers, Pittsburgh,PA. - 1998. - 132-139.

[28] **Lee S and White R M** Self-excited Piezoelectric Cantilever Oscillators [Article] // Solid-State Sensors and Actuators. - 1995. - p417-420 : Vol. 1.

[29] **Leland E S and Wright P K** Resonance tuning of piezoelectric vibration energy scavenging generators using compressive axial preload [Article] // Smart Material Structure. - 2006. - 15. - p1413-1420.

[30] **Leland E S, Lai E M and Wright P K** A self-powered wireless sensor for indoor environmental monitoring [Article]. - University of Carlifornia Berkeley : [s.n.], 2007.

[31] **Liu J Q [et al.]** A MEMS-based piezoelectric power generator array for vibration energy harvesting [Article] // Microelectronics Journal. - 2007. - 5 p802-806 : Vol. 39.

[32] **Mansour M O, Arafa M H and Megahed S M** Resonator with magnetically adjustable natural frequency for vibration energy harvesting [Article] // Sensors and Actuators A: Physical. - 2010. - Corrected Proof : Vol. In Press.

[33] **Marzencki M** Vibration energy scavenging [Article] // European Commission research Project VIBES of the 6th STREP Framework Program. - 2005.

[34] **Mateu L and Moll F** Optimum piezoelectric bending beam structures for energy harvesting using shoe inserts [Article] // J. Intell. Material System Structure. - 2005. - p835-45 : Vol. 16.

[35] **Mateu L and Moll F** Review of energy Harvesting Techniques and Applications for Microelectronics [Article] // In Proceedings of SPIE- The International Society for Optical Engineering, VLSI Circuits and Systems II, SPIE Press. - 2005. - pp. 359-373 : Vol. 5837.

[36] **Meninger S [et al.]** Vibration-to-electric energy conversion [Article] // Very Large Scale Integration (VLSI) Systems, IEEE Transactions on . - 2001. - 1. - 64-76 : Vol. 9.

[37] **Miller L M [et al.]** Strain Enhancement within cantilevered, Piezoelectric MEMS Vibrational Energy Scanveging Devices [Article] // Advances in Science and Technology. - 2008. - 54. - pp405-410 : Vol. Smart Materials &Mico/Nanosystems.

[38] **Minazara E [et al.]** Piezoelectric diaphragm for vibration energy harvesting [Article] // Ultrasonics. - 2006. - Supplement 1. - e699-e703 : Vol. 44.

[39] **Miyazak M [et al.]** Electric-energy generation using variable-capacitive resonator for power-free LSI: efficiency analysis and fundamental experiment [Article] // Low Power Electronics and

Design, 2003. ISLPED '03. Proceedings of the 2003 International Symposium on . - Tokyo Japan : [s.n.], 2003. - 193-198.

[40] **Morgan Electro Ceramics** Technical Publication TP-245 [Online] // Morgan Electro Ceramics Web Site. - Morgan Electro Ceramics. - 28 July 2010. - www.morgan-electroceramics.com.

[41] **Ng T H and Liao W H** Sensitivity Analysis and Energy Harvesting for a Self-Powered Piezoelectric Sensor [Article] // Journal of Intelligent Material Systems and Structures. - 2005. - 10. - 785-797 : Vol. 16.

[42] **Paradiso J A and Starner T** Energy Scavenging for Mobile and Wireless Electronics [Article] // IEEE Pervasive Computing. - 2005. - 1. - pp. 18-27 : Vol. 4.

[43] **Piezo System Inc** [Online] // CATALOG 2007. - Piezo System, Inc, 2007. - 25 August 2008. - http://www.piezo.com/catalog.html.

[44] Piezoelectricity [Online] // Hot Topics. - 4 Feb 2007. - http://www.discoverchemistry.com.

[45] Piezoelectricity [Online] // MaterialsWorld. - 29 June 2008. - http://www.materialsworldmodules.org/..

[46] **Qi S [et al.]** Design of a multiresonant beam for broadband piezoelectric energy harvesting [Article] // Smart Material and Structure. - 2010. - pp10 : Vol. 19.

[47] **Randall J F** On ambient energy sources for powering indoor electronic devices // PhD thesis. - [s.l.] : Ecole Polytechnique Federale de Lausanne, Switzerland, 2003.

[48] **Roundy S [et al.]** Improving power output for vibration-based energy scavengers [Article] // IEEE pervasive Computing. - 2005. - 4. - 28-36.

[49] **Roundy S [et al.]** Power Sources for Wireless Sensor Networks [Article] // Lecture Notes in Computer Science, Springer-Verlag. - 2004. - pp1-17 : Vol. 2920.

[50] **Roundy S and Zhang Y** Toward self-tuning adaptive vibration-based microgenerators [Article] // Smart Structures, Devices, and Systems II. - 2005. - 373-384.

[51] **Roundy S** Energy Scavenging for wireless sensor nodes with a focus on Vibration to electricity conversion // PhD Thesis. - [s.l.] : University of California Berkely, 2003.

[52] **Roundy S** On the effectiveness of vibration-based energy harvesting [Article] // Journal Intell. Material System Structure. - 2005. - p809-23 : Vol. 16.

[53] **Roundy S, Wright P K and Rabaey J A** A study of low level vibrations as a power source for wireless sensor nodes [Article] // Computer Communications. - 2003. - 1131-1144 : Vol. 26.

[54] **Sari I, Balkan T and Kulah H** A electromagnetic micro power generator for wideband environmental vibrations [Article] // Sensors and Actuators. - 2008. - 405-13 : Vol. A145.

[55] **Shahruz S M** Design of mechanical band-pass filters for energy scavenging [Article] // Journal of sound and vibration Volume. - 2006. - p987-998 : Vol. 292.

[56] **Shahruz S M.** Limits of performance of mechanical band-pass filters used in energy scavenging [Article] // Journal of sound and vibration. - 2006. - p449-461 : Vol. 293.

[57] **Shen D [et al.]** Micromachined PZT cantilever based on SOI structure for low frequency vibration energy harvesting [Article] // Sensors and Actuators. - 2009. - p103-108 : Vol. A154.

[58] **Shen D [et al.]** The design, fabrication and evaluation of a MEMS PZT cantilever with an integrated Si proof mass for vibration energy harvesting [Article] // J. Micromech. & Microeng.. - 2008. - Number 5. - Vol. 18.

[59] **Shenck J S and Paradiso J A** Energy scavenging with shoe-mounted piezoelectrics [Article] // IEEE Micro.. - 2001. - 30-42 : Vol. 21.

[60] **Sodano H A, Inman D J and Park G** Comparison of piezoelectric energy harvesting devices for recharging batteries [Article] // J. Intell. Mater. Syst. Structure. - 2005. - 799-807 : Vol. 16.

[61] **Sodano H A, Lloyd J and Inman D J** An Experiment comparison between several active composite actuators for power generation [Article] // Smart material Structure. - 2004. - 1211-1216 : Vol. 15.

[62] **Starner T E** Powerful Change Part1: Batteries and Possible Alternatives for the Mobile Markat [Article] // IEEE Pervasive Computing. - 2003. - 4. - pp86-88 : Vol. 2.

[63] **Starner T** Human-Powered wearable computing [Article] // IBM Systems Journal. - 1996. - 35. - 618-629 : Vol. 3.

[64] **Stephen N G** On erngy harvesting from ambient vibration [Article] // Journal of Sound and Vibration. - 2006. - 193. - p409-425.

[65] **Stordeur and Stark M** Low power Thermoelectric Generator- Self-sufficient energy supply for micro systems. [Article] // 16th International Conference on Thermoelectrics. - 1997. - p575-577.

[66] **Sunghwan K** Lower Power Energy Harvesting with Piezoelectric generators // PhD Thesis. - [s.l.] : University of Pittsburgh, 2002.

[67] **Wang P [et al.]** A micro electromagnetic low level vibration energy harvester [Article] // Microsyst Technol. - 2009. - 941-951 : Vol. 15.

[68] **Williams C B and Yates R B** Analysis of a micro- electric generator for microsystem [Article] // Sensor & Actuators. - 1996. - A52. - 8-11.

[69] **Wu wen-Jong [et al.]** Tunable resonant frequency power harvesting devices [Article] // Smart Structures and Materials 2006: Damping and Isolation.. - 2006. - pp 55-62 : Vol. 6169.

[70] **Zhou Yu, Paul S and Bhunia S** Harvesting Wasted Heat in a Microprocessor Using Thermoelectric Generators: Modelling, Analysia and Measurement [Article] // Design, Automation and Test in Europe. - 2008. - 10-14.

[71] **Zhu D [et al.]** closed loop frequency tuning of a vibration-based micro-generator [Article] // Proc. PowerMEMS 2008+ micro EMS2008. - Sendai, Japan : [s.n.], 2008. - pp229-32.

[72] **Zhu D, Tudor M J and Beeby S** Strategies for increasing the operating frequency range of vibration enegy harvester: a review [Article] // Measurement Science and Technology. - 2010. - pp29 : Vol. 21.

Appendix A Source code for Oscilloscope Capturing

```
%%%%%%%%%%%%%%%%%%%%%%%%%%%%%%%%%%%%%%%%%%%%%%%%%%%%%%%%%%%%%%%%%%%%%%%%%%%%
% This is the function created by Agilent Technologies for model
% MSO- 6054A. This function will import the binary data from the USB
% drive and transfer it into Matlab for further process.
% This function can be downloaded from
% http://www.home.agilent.com/agilent
%%%%%%%%%%%%%%%%%%%%%%%%%%%%%%%%%%%%%%%%%%%%%%%%%%%%%%%%%%%%%%%%%%%%%%%%%%%%

function [timeVector, voltageVector] = importAgilentBin(inputFilename,
varargin)
% ImportAgilentBin reads the Agilent Binary Waveform filetype.
% [timeVector, voltageVector] = importAgilentBin(inputFilename)
% [timeVector, voltageVector] = importAgilentBin(inputFilename,
waveform_index)
% if waveformIndex is not provided, the first waveform will be read
% voltageVector may contain two columns [MIN, MAX]

 if (~exist(inputFilename))
    error('inputFilename missing.');
end

fileId = fopen(inputFilename, 'r');

fileCookie = fread(fileId, 2, 'char');      % read file header
fileVersion = fread(fileId, 2, 'char');
fileSize = fread(fileId, 1, 'int32');
nWaveforms = fread(fileId, 1, 'int32');

fileCookie = char(fileCookie');         % verify cookie
if (~strcmp(fileCookie, 'AG'))
    fclose(fileId);
    error('Unrecognized file format.');
end

waveformSelect = 1;                 % determine which waveform to read
if (size(varargin) == 1 & varargin{1} <= nWaveforms)
    waveformSelect = varargin{1};
end

for waveformIndex = 1:nWaveforms        % read waveform header
    headerSize = fread(fileId, 1, 'int32'); bytesLeft = headerSize - 4;
    waveformType = fread(fileId, 1, 'int32'); bytesLeft = bytesLeft - 4;
    nWaveformBuffers = fread(fileId, 1, 'int32'); bytesLeft = bytesLeft
- 4;
    nPoints = fread(fileId, 1, 'int32'); bytesLeft = bytesLeft - 4;
    count = fread(fileId, 1, 'int32');  bytesLeft = bytesLeft - 4;
    xDisplayRange = fread(fileId, 1, 'float32');  bytesLeft = bytesLeft
- 4;
    xDisplayOrigin = fread(fileId, 1, 'double');  bytesLeft = bytesLeft
- 8;
    xIncrement = fread(fileId, 1, 'double');  bytesLeft = bytesLeft - 8;
    xOrigin = fread(fileId, 1, 'double');  bytesLeft = bytesLeft - 8;
    xUnits = fread(fileId, 1, 'int32');  bytesLeft = bytesLeft - 4;
    yUnits = fread(fileId, 1, 'int32');  bytesLeft = bytesLeft - 4;
    dateString = fread(fileId, 16, 'char'); bytesLeft = bytesLeft - 16;
    timeString = fread(fileId, 16, 'char'); bytesLeft = bytesLeft - 16;
    frameString = fread(fileId, 24, 'char'); bytesLeft = bytesLeft - 24;
    waveformString = fread(fileId, 16, 'char'); bytesLeft = bytesLeft -
16;
```

```
    timeTag = fread(fileId, 1, 'double'); bytesLeft = bytesLeft - 8;
    segmentIndex = fread(fileId, 1, 'uint32'); bytesLeft = bytesLeft - 4;

    % skip over any remaining data in the header
    fseek(fileId, bytesLeft, 'cof');

    % generate time vector from xIncrement and xOrigin values
    if (waveformIndex == waveformSelect)
        timeVector = (xIncrement * [0:(nPoints-1)]') + xOrigin;
    end

   for bufferIndex = 1:nWaveformBuffers
     % read waveform buffer header
    headerSize = fread(fileId, 1, 'int32'); bytesLeft = headerSize - 4;
    bufferType = fread(fileId, 1, 'int16'); bytesLeft = bytesLeft - 2;
    bytesPerPoint = fread(fileId, 1, 'int16'); bytesLeft = bytesLeft - 2;
    bufferSize = fread(fileId, 1, 'int32'); bytesLeft = bytesLeft - 4;

        % skip over any remaining data in the header
        fseek(fileId, bytesLeft, 'cof');

      if (waveformIndex == waveformSelect)
        if ((bufferType == 1) | (bufferType == 2) | (bufferType == 3))
     % bufferType is PB_DATA_NORMAL, PB_DATA_MIN, or PB_DATA_MAX (float)
        voltageVector(:, bufferIndex) = fread(fileId, nPoints, 'float');
        elseif (bufferType == 4)
            % bufferType is PB_DATA_COUNTS (int32)
        voltageVector(:, bufferIndex) = fread(fileId, nPoints, '*int32');
        elseif (bufferType == 5)
            % bufferType is PB_DATA_LOGIC (int8)
        voltageVector(:, bufferIndex) = fread(fileId, nPoints, '*uint8');
        else
            % unrecognized bufferType read as unformated bytes
     voltageVector(:, bufferIndex) = fread(fileId, bufferSize, '*uint8');
            end
        else
            fseek(fileId, bufferSize, 'cof');
        end
    end
end
fclose(fileId);


%%%%%%%%%%%%%%%%%%%%%%%%%%%%%%%%%%%%%%%%%%%%%%%%%%%%%%%%%%%%%%%%%%%%%%%%%%%%
% This program will read the data out the USB drive and work out the
% the FFT with frequency spectrum plotting
%%%%%%%%%%%%%%%%%%%%%%%%%%%%%%%%%%%%%%%%%%%%%%%%%%%%%%%%%%%%%%%%%%%%%%%%%%%%

[xX,yX]=importAgilentBin('print_07.bin',1);
% import data from the USB drive
sample_frequencyX=1/abs(xX(1)-xX(2));
% calculate the sampling frequency by getting the period between two
sampling points
dtX=1/sample_frequencyX;            % calculate the sampling period
g=9.81;                             % g= 9.81 m/s^2
k=0.9915;                           % accelerometer output voltage:
991.5mV/g
AX=(yX-mean(yX))*g/k;               % convert the output voltage to
acceleration
magAX=abs(fft(AX-mean(AX),length(AX)))/length(AX);
% get the FFT for the Acceleration
frX=(0:length(AX)-1)/(length(AX)*dtX);
```

```
% create the freqeuncy axis
magAX(1:5)=0;
magAX(length(magAX))=0;
% make the first 5 values and last value of magA become 0 to avoid the
value divide by zero for displacement

dX=magAX./((2*pi).*frX').^2;
% find the displacement from Acceleration (A/w^2), w=2*pi*f

n=1:round(length(magAX)/2);
Half_Maximum_AccelerationX=max(magAX(n));
Maximum_AccelerationX=2*Half_Maximum_AccelerationX;
indiceX=min(find(Half_Maximum_AccelerationX==magAX));
MaximumY_AFrequencyX=indiceX/length(magAX)*sample_frequencyX ;
%find the Frequency value on Maximum Y value

n=1:round(length(dX)/2);
Half_Maximum_DisplacementX=max(dX(n));
Maximum_DisplacementX=2*Half_Maximum_DisplacementX;
indiceX=min(find(Half_Maximum_DisplacementX==dX));
MaximumY_dFrequencyX=indiceX/length(dX)*sample_frequencyX;
%find the Displacement value on Maximum Y value

semilogy(frX (1:1000),2*dX(1:1000))
% plot the semilogy for y axis
title('Displacement over Frequency (X)')
xlabel('Frequency (Hz)')
ylabel('Displacement (m)')
axis([0 500 1e-10 1e-4])
grid
figure

semilogy(frX (1:1000),2*magAX(1:1000))      % plot the semilog for y
axis
axis([0 500 0 10])                          % set the scale axis
title('Acceleration over Frequency (X)')
xlabel('Frequency (Hz)')
ylabel('Acceleration (m/s^2)')
grid
```

Appendix B Source Code for Data Acquisition Toolbox Adapter Capturing

```
%%%%%%%%%%%%%%%%%%%%%%%%%%%%%%%%%%%%%%%%%%%%%%%%%%%%%%%%%%%%%%%%%%%%%%%%%%%%%%%
% This code will take the data directly from the DAQ2205 card and the
% the matlab is then work out the fft of the data and a frequency
% spectrum is plotted.
%%%%%%%%%%%%%%%%%%%%%%%%%%%%%%%%%%%%%%%%%%%%%%%%%%%%%%%%%%%%%%%%%%%%%%%%%%%%%%%

ai_device=analoginput('mwadlink',0)     % set the analogue device
ai1=addchannel(ai_device, 0)            % add a channel for the device
set(ai_device, 'InputType','Differential')
% chose the differential mode for the measurement

%%%%%%%%%%%%%%%%%%%%%%%%%%%%%%%%%%%%%%%%%%%%%%%%%%%%%%%%%%%%%%%%%%%%%%%%%%%%%%%
% General setting for the DAQ-2205
%%%%%%%%%%%%%%%%%%%%%%%%%%%%%%%%%%%%%%%%%%%%%%%%%%%%%%%%%%%%%%%%%%%%%%%%%%%%%%%
duration =1;
% set the duration of data
set(ai_device, 'SampleRate', 10000)             % set the sample rate
per second
ActualRate= get(ai_device,'SampleRate');
set(ai_device, 'SamplesPerTrigger',duration*ActualRate)
set (ai_device, 'TriggerType', 'Manual')            % set trigger as
manual mode
blocksize=get (ai_device, 'SamplesPerTrigger');
Fs= ActualRate;
start(ai_device)                    % start the capturing process
trigger(ai_device)                  % trigger the channel
wait(ai_device,duration+2)
% wait for duration + 2seconds
olddata = getdata(ai_device);           % get the data from the DAQ card
delete (ai_device)                      % delete the device
clear ai_device
%%%%%%%%%%%%%%%%%%%%%%%%%%%%%%%%%%%%%%%%%%%%%%%%%%%%%%%%%%%%%%%%%%%%%%%%%%%%%%%

g=9.81;                     % gravity = 9.81 m/s^2
k=0.9915;                   % accelerometer output voltage: 991.5mV/g
data=(olddata-mean(olddata))*g/k;
% convert the output voltage to acceleration
xfft=abs(fft(data-mean(data),length(data)))/length(data);
% get the fft of the data
xfft(1:5)=0;
xfft(length(xfft))=0;
mag = xfft;
mag=mag(1:floor(blocksize/2));
f= (0:length(mag)-1)*Fs/blocksize;      % get the frequency scale
f=f(:);
semilogy(f,2*mag)
% plot the graph, mag*2 because second harmonic
grid on
ylabel ('Acceleration (m/s^2)')
xlabel ('Frequency (Hz)')
title ('Vibration Spectrum')
axis ( [0 500 0 10])
[ymax,maxindex]=max (mag);
maxfreq = f(maxindex)
ymaximum=ymax*2
```

Appendix C Vibration source generating code

```
%%%%%%%%%%%%%%%%%%%%%%%%%%%%%%%%%%%%%%%%%%%%%%%%%%%%%%%%%%%%%%%%%%%%%%%%%%%%
% This coding will generate the sine wave with particular frequency and
% acceleration according to the user input.
%%%%%%%%%%%%%%%%%%%%%%%%%%%%%%%%%%%%%%%%%%%%%%%%%%%%%%%%%%%%%%%%%%%%%%%%%%%%

close all;
clc;
clear all;
format short;
Vrms=1;
SampleRateValue=20000;              %Sampling Rate (DON CHANGE)
output_duration=20;                 %Output duration in second
Acceleration =9.81/2;               %Acceleration in ms-2
Output_Frequency =40;               %Output Frequency in Hz

%%%%%%%%%%%%%%%%%%%%%%%%%%%%%%%%%%%%%%%%%%%%%%%%%%%%%%%%%%%%%%%%%%%%%%%%%%%%
% General setting for DAQ-2205
%%%%%%%%%%%%%%%%%%%%%%%%%%%%%%%%%%%%%%%%%%%%%%%%%%%%%%%%%%%%%%%%%%%%%%%%%%%%
ao_device = analogoutput('mwadlink',0);
ao=addchannel(ao_device,0);
set(ao_device,'SampleRate',SampleRateValue);
set(ao_device,'TriggerType','Manual');
ActualRate_ao=get(ao_device,'SampleRate');
AO_Rate=ActualRate_ao;
set(ao_device,'RepeatOutput',0);
%%%%%%%%%%%%%%%%%%%%%%%%%%%%%%%%%%%%%%%%%%%%%%%%%%%%%%%%%%%%%%%%%%%%%%%%%%%%

%%%%%%%%%%%%%%%%%%%%%%%%%%%%%%%%%%%%%%%%%%%%%%%%%%%%%%%%%%%%%%%%%%%%%%%%%%%%
% System calibration
%%%%%%%%%%%%%%%%%%%%%%%%%%%%%%%%%%%%%%%%%%%%%%%%%%%%%%%%%%%%%%%%%%%%%%%%%%%%
Data_Matrix=xlsread('Calibrate.xls');
Frequency= Data_Matrix(:,1);
Scale=Data_Matrix(:,2);
Frequency_Interp = 20:0.1:200;
Scale_Interp = interp1(Frequency,Scale,Frequency_Interp,'spline');
Frequency_Interp=(round(Frequency_Interp*10))/10;
n=find(Frequency_Interp==Output_Frequency);
Vibrator_Scale=Scale_Interp(1,n);
%%%%%%%%%%%%%%%%%%%%%%%%%%%%%%%%%%%%%%%%%%%%%%%%%%%%%%%%%%%%%%%%%%%%%%%%%%%%

%%%%%%%%%%%%%%%%%%%%%%%%%%%%%%%%%%%%%%%%%%%%%%%%%%%%%%%%%%%%%%%%%%%%%%%%%%%%
% Signal generation
%%%%%%%%%%%%%%%%%%%%%%%%%%%%%%%%%%%%%%%%%%%%%%%%%%%%%%%%%%%%%%%%%%%%%%%%%%%%
Vpp=Acceleration*2/(9.81);
Vpeak=Vibrator_Scale*(Vpp/2);
repeat=output_duration-1;
data=Vpeak*sin(linspace(0,2*pi*Output_Frequency,AO_Rate));
oris=data;
full=length(data);
control=Output_Frequency-floor(Output_Frequency);
if (control>0 && control<0.5)
    ind=find(data<0);
    lastnegative=ind(1,end);
    offset=full-lastnegative;
    data=data(1:lastnegative);
    oris=circshift(oris,[1,offset]);
    coun=[1:1:offset];
    oris(1,coun)=0;
elseif (control>0.4)
    ind=find(data>0);
```

```
    lastpositive=ind(1,end);
    offset=full-lastpositive;
    data=data(1:lastpositive);
    ind=find(data<0);
    lastnegative=ind(1,end);
    offset=offset+(lastpositive-lastnegative);
    data=data(1:lastnegative);
    oris=circshift(oris,[1,offset]);
    coun=[1:1:offset];
    oris(1,coun)=0;
else
    offset=0;
    coun=[1:1:offset];
end

if (output_duration >1)
    for mt=1:repeat
    zeroarray=zeros(1,offset);
    oris=cat(2,zeroarray,oris);
    oris=cat(2,oris,data);
    end
end
%%%%
putdata(ao_device,oris');

start(ao_device);
trigger(ao_device);
wait(ao_device,output_duration+2);
%%%%%%%%%%%%%%%%%%%%%%%%%%%%%%%%%%%%%%%%%%%%%%%%

delete(ao_device) % clear the device
clear ao_device;
```

Appendix D Analytical modelling for varying load resistance

```
%%%%%%%%%%%%%%%%%%%%%%%%%%%%%%%%%%%%%%%%%%%%%%%%%%%%%%%%%%%%%%%%%%%%%%%%%%%%
% This program creating an analytical modelling of the piezo generator
% with varying load resistance.
%%%%%%%%%%%%%%%%%%%%%%%%%%%%%%%%%%%%%%%%%%%%%%%%%%%%%%%%%%%%%%%%%%%%%%%%%%%%

close all
syms w R C Y d tc b1 e s k A b lb lm le lc width
C=51e-9;        % set the capacitance of the beam
b1=(3*b*(2*lb+lm-le))/(lb^2*(2*lb+(3*lm/2)));
P=1/(2*w^2)*(A^2*R*C^2*(Y*d*tc*b1/e)^2)/((4*s^2+k^4)*(R*C*w)^2+4*s*k^2*R
*C*w+4*s^2);
% Power equation
A=4.905;        % driving acceleration
w=2*pi*73;      % driving frequency
d=-190e-12;     % piezoelectric strain coefficient
e=1.594e-8;     % dielectric constant of the piezoelectric material
Y=66e9;         % material Young's Modulus
k=0.29;         % coupling coefficient
width=12.7e-3;  % beam width
lb=21.5e-3;
lm=2e-3;
le=31.5e-3;
tc=0.19e-3;
tsh=0.13e-3;
b=0.16e-3;
s=0.02858;      % damping ratio
C=subs(C);
b1=subs(b1);

Rv=6000:600000/100:600000;
P=subs(P);
se=subs(se);
Pv=subs(P,R,Rv);
sev=subs(se,R,Rv);
Data_Matrix=xlsread('PowerVsResistanceRec');

xlabel('Resistance Ohm')
ylabel('Power (watt)')
plot(Rv/1000,Pv*1000,'r',Data_Matrix(:,3)/1000,Data_Matrix(:,4)*1000,'b'
,Data_Matrix(:,3)/1000,Data_Matrix(:,4)*1000,'*')
legend('Simulation Output','Prototype Output','Prototype Output Points')
xlabel('Resistance (KOhm)')
ylabel('Power (miliwatt)')
```

Appendix E Analytical modelling for varying driving frequency

```
%%%%%%%%%%%%%%%%%%%%%%%%%%%%%%%%%%%%%%%%%%%%%%%%%%%%%%%%%%%%%%%%%%%%%%%%%%%%%%%%
% This program creating an analytical modelling of piezo generator with
% of varying driving frequency.
%%%%%%%%%%%%%%%%%%%%%%%%%%%%%%%%%%%%%%%%%%%%%%%%%%%%%%%%%%%%%%%%%%%%%%%%%%%%%%%%

clear all
hold off
RR=[6 10 15 30 50 60 80 100 200 400 600];

for i=1:length(RR)
syms w wn R C Y d tc b1 e s k A b lb lm le lc width real
V1=(A*Y*w*d*tc*b1/e)*-j;
V2=((wn^2/(R*C)-(1/(R*C)+2*s*wn)*w^2))^2+(w*(wn^2*(1+k^2)+2*s*wn/(R*C)-
w^2))^2;
V3=sqrt(((wn^2/(R*C)-(1/(R*C)+2*s*wn)*w^2))^2+(w*(wn^2*(1+k^2)+
2*s*wn/(R*C)-w^2))^2);
V=(V1*V3)/V2;
P=V^2/(2*R);    % Power Equation
Data=xlsread(['Resistance' num2str(RR(i)) 'K']);
Prms=Data(:,4);
Fre=Data(:,1);
ind=find(Prms==max(Prms));
optf=Fre(ind,1);
optf=73;
R=RR(i)*1000;
C=51e-9;        % set the beam capacitance
b1=(3*b*(2*lb+lm-le))/(lb^2*(2*lb+(3*lm/2)));
P=abs(P);
A=4.905;        % driving acceleration
wn=2*pi*optf;   % driving frequency
d=-190e-12;     % strain coefficient
e=1.594e-8;     % dielectric constant
Y=66e9;         % material Young's Modulus
k=0.29;         % coupling coefficient
width=12.7e-3;  % beam width
lb=21.5e-3;
lm=2e-3;
le=31.5e-3;
tc=0.19e-3;
tsh=0.13e-3;
b=0.16e-3;
b1=subs(b1);
fv=40:0.3:200;
wv=fv.*pi*2;
s=0.029;        % damping ratio
P10k=subs(P);
P10k=subs(P10k,w,wv);
plot(fv+20*i,P10k*1000,'b',Fre+20*i+1,Prms*1000,'r')
xlabel('Xscale')
ylabel('Power (miliwatt)')
text(optf+20*i,max(P10k*1000)+0.01,[num2str(RR(i)) 'k'])
axis([40 350 0 0.7])
drawnow
legend('Simulation Output','Prototype Output')
hold on
end
```

Appendix F Analyzing the relationship for radius of curvature

Chapter 7 indicates that the second derivative of the beam deflection is given as inversion of the radius of curvature, $\frac{\partial^2 u}{\partial x^2} = \frac{1}{R}$. However to improve the readability in that chapter, many of details were left out. The objective for this appendix is to provide the full details of the all the derivation of the analytical proofs.

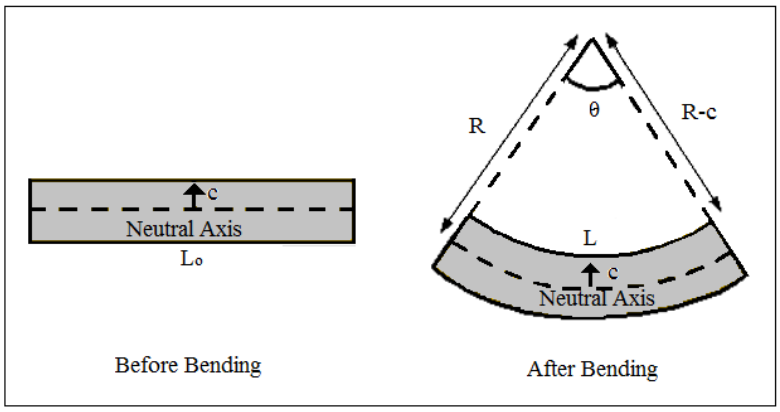

Figure F1- Small section of beam in bending

Figure F1 shows a small section of beam in initial and bent configuration. Recall the basic definition of normal strain is:

$$\varepsilon = \frac{Change\ in\ the\ length}{Original\ length} = \frac{L - L_o}{L_o} \qquad \text{Equation F1}$$

Therefore, the magnitude of axial strain above the neutral axis is given by:

$$|\varepsilon| = \frac{\theta(R-c) - \theta R}{\theta R} = \frac{c}{R} \qquad \text{Equation F2}$$

where R is the radius to the neutral axis

θ is the bending angle

c is the distance from the neutral axis to a point of interest

The strain can be converted into stress by using Hooke's law where the bending stress is the product of the material Young's Modulus (E) and the beam strain (ε). This gives the bending stress as:

$$|\sigma| = \frac{Ec}{R}$$ Equation F3

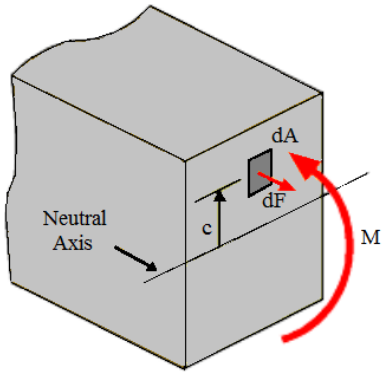

Figure F2- Section cut of a beam

To find out the relationship of the beam bending moment (M) and the radius of curvature (R), equating the moment due to the normal stresses on an arbitrary beam cross section area as depicted in Figure F2:

$$M = \int c\, dF = \int c\sigma\, dA$$ Equation F4

Substituting Equation F3 into Equation F4 gives:

$$M = \frac{E}{R}\int c^2\, dA$$ Equation F5

Recalling that the integral in this relation is the area moment of inertial (I) about the neutral axis, therefore the relation between the bending moment and the radius of curvature of the neutral axis of the beam becomes:

$$M = \frac{EI}{R}$$ Equation F6

Generally, the tensile stress experienced by the beam can be expressed as Equation F7 where $\frac{\partial^2 u}{\partial x^2}$ is the second derivative of the beam deflection.

$$\sigma = \frac{Mc}{I} = Ec\frac{\partial^2 u}{\partial x^2}$$ Equation F7

by carefully comparing both Equation F6 and Equation F7, it proves that the second derivative of the beam deflection is given as inversion of the radius of curvature.

$$\frac{\partial^2 u}{\partial x^2} = \frac{1}{R}$$ Equation F8

Appendix G Analytical modelling for different beam structure

```
%%%%%%%%%%%%%%%%%%%%%%%%%%%%%%%%%%%%%%%%%%%%%%%%%%%%%%%%%%%%%%%%%%%%%%%%%%%%
% A supported cantilever beam which a concentrated load at the free end
% will be analytically modeled, 5 different structure will be considered.
% This program will define the strain equation analytically, then all
% others terms will be substitute into this equation according to their
% beam shape, the resultant strain will then be normalized and plotted.
%%%%%%%%%%%%%%%%%%%%%%%%%%%%%%%%%%%%%%%%%%%%%%%%%%%%%%%%%%%%%%%%%%%%%%%%%%%%

clear all
syms x W E I b b0 b1 h u L M U y h0

structure=5;        % structure to be simulated
M=W*(L-x);

if (structure<4)            % Use for Structure 1,2,3
   b=b0+(b1*(x*1000));

elseif (structure<5)        % use for structure 4
   p1 = -5.1112e-005;
   p2 = -0.011261;
   p3 = 0.011548;
   p4 = 15.972;
   b=p1*(x*1000+1).^3+p2*(x*1000+1).^2+p3*(x*1000+1)+p4;
   % manually defined curved for structure 4
else                        % use for structure 5
   p1 = -5.1112e-005;
   p2 = 0.016168;
   p3 = -0.86617;
   p4 = 16.85;
   b=p1*(x*1000+1).^3+p2*(x*1000+1).^2+p3*(x*1000+1)+p4;
   % manually defined curved for structure 5
end

h=h0;
y=h;
I=(b*h^3)/12;               % moment of Inertia
d2u=(W*L-W*x)/(E*I);
% General equation for cantilever beam for concentration load at the end
strain=d2u*y;       % Strain on bending beam
y=0.001;            % a distance from the neutral axis
L=0.03;             % set the dimension of the beam

if (structure<2)
  b0=0.01;           % Original width for case 1
  b1=0;              % variable width for Structure 1
elseif (structure<4)
  b0=0.015;          % Original width for case 2 & 3
  if (structure==2)
     b1=-3.33e-4;    % variable width for Structure 2
  else
     b1=-4.9999e-4;  % variable width for Structure 3
  end
else
  b0=0.016;          % Original width for case 4 & 5
end

h0=0.0002;          % depth of the beam
W=1;                % ending force (newton)
E=200e9;            % material young's modulus (304 Stainless Steel)
```

```
b=subs(b);
I=subs(I);
y=subs(y);
h=subs(h);
M=subs(M);
d2uv=subs(d2u);
xv=0:0.00001:L;

strain=subs(strain);
strainv=subs(strain,x,xv);
ratio=strainv./max(strainv);
bv=subs(b,x,xv);
tempo=ones(1,length(xv));
tempo(1,1:length(xv))=bv;
bv=tempo;

plot(xv,ratio)
% plot the normalized strain
title(['Stucture ' num2str(structure) ''])
ylabel('Normalised Strain')
xlabel('Beam length [x] (m)')
axis([0 0.032 0 1.1])

display('Average of the total of strain ratio')
Average=sum(ratio)/length(ratio)   %Average of strain ratio

% plot the histogram for strain distribution
bin=linspace(0,1,21);
if(structure==1)
    bc=1e-6;      % Structure 1
elseif (structure==2)
    bc=0.5e-6;    % Structure 2
elseif (structure==3)
   bc=3e-7;       % Structure 3
else
    bc=8e-7;      % Structure 4 & 5
    bv=bv./1000;
end

beam=-ones(round((bv(1)/bc)/10),length(xv));

for i=1:length(xv)
    eratio=ratio(i);
    beam(1:round((bv(i)/bc)/10),i)=eratio;
end

% generate the histogram
 j=find(beam>=0);
 number=hist(beam(j),bin);
 numberp=(number./length(j))*100;
 figure
 bar(bin,numberp,1)

n75=find(beam(j)>=0.75);  % find the index which higher than 0.75
n50=find(beam(j)>=0.50);  % find the index which higher than 0.5
format short
Percentage75=length(n75)/length(j)*100
% Get the percentage value for 0.75 strain ratio
Percentage50=length(n50)/length(j)*100
% Get the percentage value for 0.50 strain ratio
```

Appendix H Numerical modelling for different beam structure

```
%%%%%%%%%%%%%%%%%%%%%%%%%%%%%%%%%%%%%%%%%%%%%%%%%%%%%%%%%%%%%%%%%%%%%%%%%%%%
% A supported cantilever beam which a concentrated load at the free end
% will be analytically modeled, 5 different structure will be consider.
% This program will read in ANSYS data, normalizes the data, and plot
% those data as histogram. Number of nodes that having the strain ratio
% more than 0.5 and 0.75 are also calculated.
%%%%%%%%%%%%%%%%%%%%%%%%%%%%%%%%%%%%%%%%%%%%%%%%%%%%%%%%%%%%%%%%%%%%%%%%%%%%

close all
clear all
format short e
structure=5;      % select the structure to be displayed

list=xlsread(['nStrain' num2str(structure) '.xls']);
%import the ansys data into matlab
maximum=max(list);
minimum=min(list);
ratio = list./maximum;  % creating the strain ration
bin=linspace(minimum/maximum,maximum/maximum,21);
% creating the bin space

display('Average of the total of strain ratio')
Average=sum(ratio)/length(ratio)   %Average of strain ratio

number= hist(ratio,bin);
% getting the number of nodes for each strain ratio
numberp=(number./length(list))*100;
% convert the number of nodes into percentage
figure
bar(bin,numberp,1)
% plot the histogram
title(['Structure ' num2str(structure) ''])
xlabel('Strain Ratio')
ylabel('Number of Nodes in Percent (%)')

count75=0;
count50=0;
l=length (ratio);

for n = 1:l
    if (ratio(n) >=0.75)       % i=find (ratio>0.5)
        count75 = count75+1;   % count the number of number >0.75
    end
    if (ratio(n) >=0.5)       % i=find (ratio>0.5)
        count50 = count50+1;  % count the number of number >0.5
    end
end

format short
Percentage75=(count75/l)*100    % display the number in percent
Percentage50=(count50/l)*100
```

Appendix I Simulink Model for loads switching tuning method

In order to improve the readability in Chapter 8, many of the details were left out regarding the Matlab Simulink model for the load switching tuning method. However, in this appendix, more detail of the all the Matlab coding and the Simulink simulation in that chapter is provided.

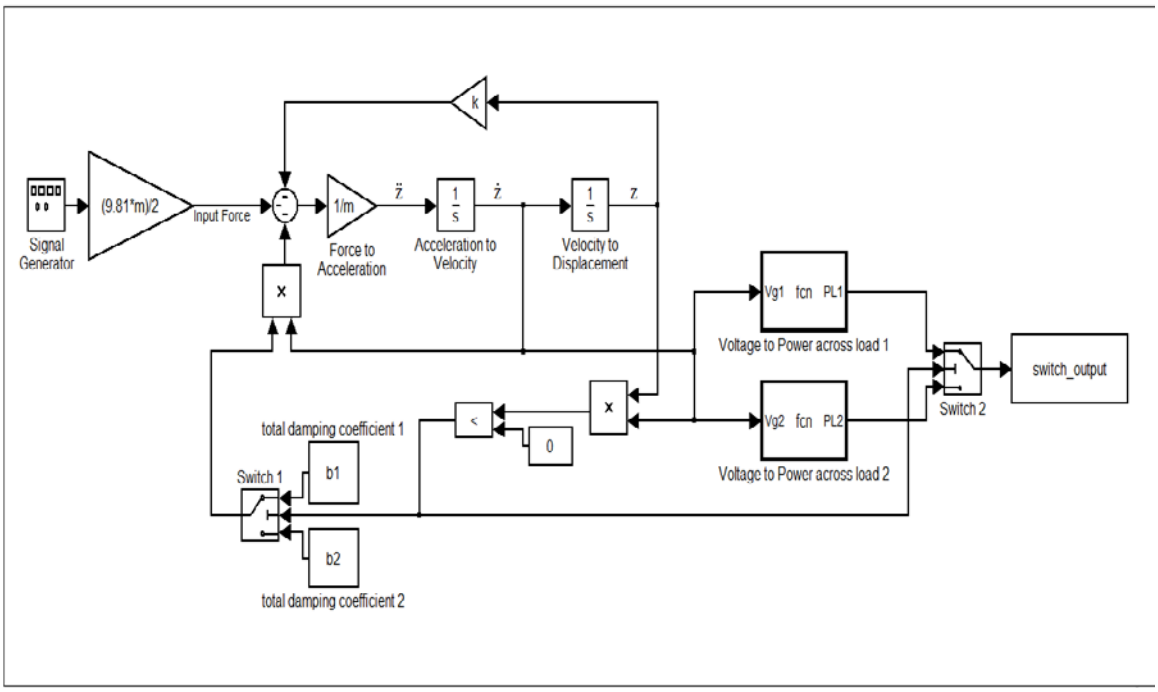

Figure I1 - Simulink model for Electromagnetic loads switching generator

Figure I1 shows the entire Simulink model for Electromagnetic load switching generator. This model can be separated into four parts, the first part is the governing equation model for the system which is shown in Figure I2 and the governing equation is given as:

$$m\ddot{z} + (b_e + b_m)\dot{z} + kz = -m\ddot{y} \qquad \text{Equation I1}$$

rearrange this equation gives

$$m\ddot{z} = -m\ddot{y} - (b_e + b_m)\dot{z} - kz \qquad \text{Equation I2}$$

where $\ddot{y}$ is the driving acceleration amplitude which equal to 0.5g and g is the standard gravity that is established as 9.81 m/s^2. There are two total damping coefficients that will be used in turn here according to the oscillating quadrant. They are $b_1 = b_{e1} + b_m$ which is used in quadrant I and III and $b_2 = b_{e2} + b_m$ which is used in quadrant II and IV.

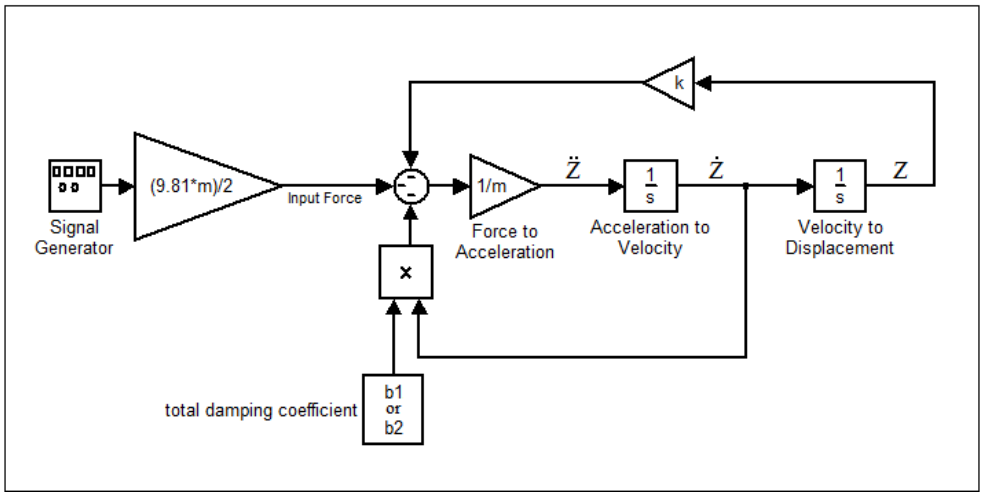

Figure I2 - Governing equation model

Added to the above, in this model a selecting device that is responsible for deciding which damping value should be used during the simulation. Therefore, the second part of the system will be the "decision maker" as shown in Figure I3. This model will multiply the system's Displacement (z) and Velocity ($\dot{z}$). The product in quadrant I and III will be below zero but on the other hand the product in quadrant II and IV will be above zero. This allow the Relational Operation in this model to create two set of outputs, True for quadrant I and III and False for quadrant II and IV. The True and False outputs will then be sent to the switches to decide which damping coefficients and velocity-to-power conversations need to be applied during the oscillation at that particular time.

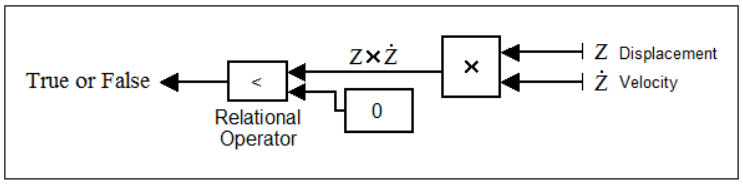

Figure I3- “Decision maker” model

Figure I4 is the controller for the total damping coefficients also the third part of the system. It decides which damping coefficient is to be used during the different quadrant. It takes the True and False signal generated from the “decision maker” model and decides what its output according to the conditional input. Switch 1 will send out the first damping coefficient (b_1) when the conditional input is True and on the other hand it will send out the second damping coefficient (b_2) when the conditional input is False.

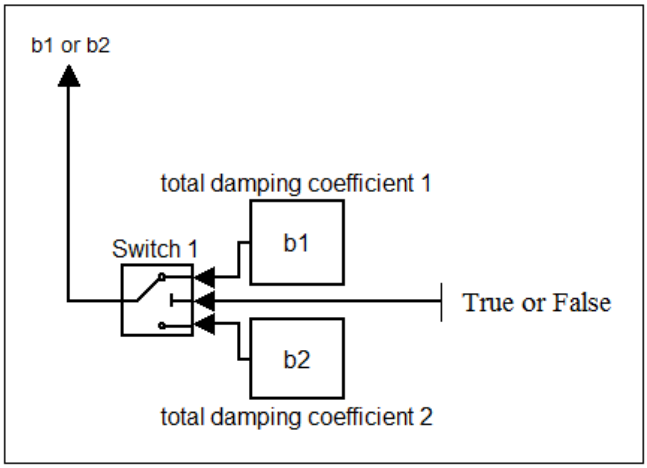

Figure I4- switch controller for the total damping coefficient

In Figure I5, it shows the final part for this modelling. This model is responsible for the velocity-to-power conversion by using the general power equation, $P = \frac{V^2}{R}$. Similar to the damping coefficient controller, this model takes the True and False signal generated from the “decision maker” model and decides which converter going to be used to transform the velocity into power. Switch 2 will use the first converter if conditional input is True and in the contrary second converter will be used if the conditional input is False.

The embedded Matlab function “Vel fcn PL1” translates velocity into power using the following code shown in Figure I6. The code for embedded Matlab function “Vel fcn PL2” is similar to the first one except the variables PL1,VL1 and RL1 are replaced by PL2, VL2 and RL2 respectively as shown in Figure I7.

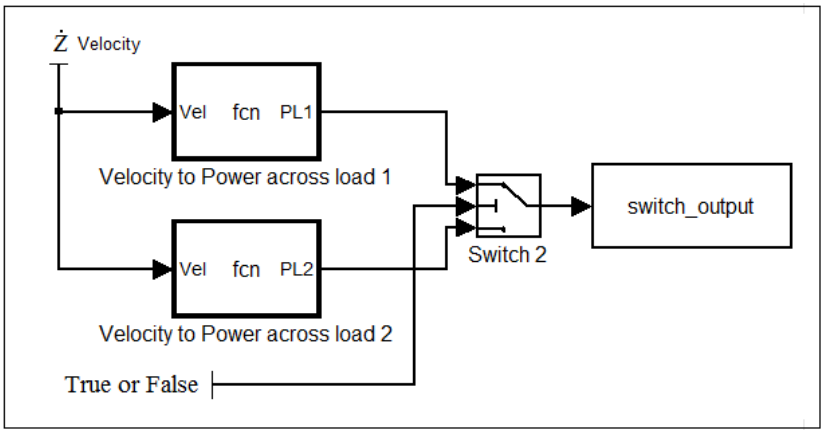

Figure I5 - switch controller for the velocity-to-power conversion

```
% This Matlab function will convert the velocity (Vel) to Power (PL1)

function PL1 = fcn(Vel)
% PL1= Power across Load 1
% Vel= system velocity

Vg=Vel*ke;
% Vg is the generated voltage
% ke is the EMF constant
VL1=Vg*RL1/(Rc+RL1);
% VL1 is the voltage across load 1
% RL1 is the resistive load 1
% Rc is the coil resistance for the generator
PL1=VL1^2/RL1;
% PL1 is the power across load 1

```

Figure I6 - Embedded Matlab function code for velocity to power conversion 1

```
% This Matlab function will convert the velocity (Vel) to Power (PL2)

function PL2 = fcn(Vel)
% PL2= Power across Load 2
% Vel= system velocity

Vg=Vel*ke;
% Vg is the generated voltage
% ke is the EMF constant
VL2=Vg*RL2/(Rc+RL2);
% VL2 is the voltage across load 2
% RL2 is the resistive load 2
% Rc is the coil resistance for the generator
PL2=VL2^2/RL2;
% PL2 is the power across load 2

```

Figure I7 – Embedded Matlab function code for velocity to power conversion 2

Chapter 10 References

[1] Agah, M., Baek, k., & Potkay, J. A. (2002). Design and Analysis of a Piezoelectric Vibration Powered Microgenerator System. *ME 553 University of Michigan* .

[2] Amirtharajah, R., & Chandrakasan, A. P. (1998). Self-powered signal processing using vibration-based power generation. *IEEE J. Solid-State Circuits* (687-695).

[3] *ANSYS,Inc*. (n.d.). Retrieved from http://www.ansys.com/

[4] Baker, J., Roundy, S., & Wright, P. (2005). Alternative Geometries for increasing power density in vibration energy scavenging for wireless sensor networks. *Porc. 3rd Int. Energy Conversion Engineering Conf. (San Fancisco)* (p959-70).

[5] Bedekar, V., Oliver, J., & Priya, S. (2009). Pen harvester for powering a pulse rate sensor. *Journal of Physics D: Applied Physics , 42* (9pp).

[6] Beeby, S. P., Torah, R. N., Tudor, M. J., Glynne-Jones, P., O'Donnell, T., Saha, C. R., et al. (2007). A micro electromagnetic generator for vibration energy harvesting. *Journal of Micromechanics and Microengineering , 17* (1257).

[7] Beeby, S. P., Tudor, M. J., & White, N. M. (2006). Review Article-Energy harvesting vibration source for microsystems applications. *17* (R175-R195).

[8] Beeby, S. P., Tudor, M. J., Koukharenko, E., White, N. M., O'Donnel, T., Saha, C., et al. (2005). Micromachined silicon Generator for Harvesting Power from Vibrations. (pp 780-3).

[9] Beeby, S. P., Tudor, M. J., Koukharenko, E., White, N. M., O'Donnell, T., Saha, C., et al. (2005). Design and performance of a microelectromagnetic vibration-powered generator. *Actuators and Microsystems , 1* (pp780-783).

[10] Benham, P. P., Crawford, R. J., & Armstrong, C. G. (1997). *Mechanics of Enginering Materials* (Vols. [ISBN: 0-582-25164-8]). Prentice Hall.

[11] Bin, Y., Chengkuo, L., Wenfeng, X., Jie, X., Jonny Han, H., Rama, K. K., et al. (2009). Electromagnetic energy harvesting from vibrations of multiple frequencies. *Journal of Micromechanics and Microengineering , 19* (8pp).

[12] Challa, V. R., Prasad, M. G., Shi, Y., & Fisher, F. T. (2007). A vibration energy harvesting device with bidirectional resonance frequency tunability. *Smart Materials and structures , 17* (015035 (10pp)).

[13] Cho, J., Anderson, M., Richards, R., Bahr, D., & Richards, C. (2005). Optimization of electromechanical coupling for a thin-film PZT membrane: I Modeling. *J. Micromech. Microeng. , 15* (1797-1803).

[14] Cho, J., Anderson, M., Richards, R., Bahr, D., & Richards, C. (2005). Optimization of electromechanical coupling for a thin-film PZT membrane: II Experiment. *J. Micromech. Microeng , 15* (1804-1809).

[15] Cottone, F., Vocca, H., & Gammaitoni, L. (2009). Nonlinear Energy Harvesting. *Phys. Rev. Lett. , 102* (8).

[16] Donelan, J. M., Li, Q., Naing, V., Hoffer, J. A., Weber, D. J., & Kuo, A. D. (2008). Biomechanical Energy Harvesting: Generating Electricity During Walking with Minimal User Effort. *Science , 319* (pp807-810).

[17] Eichhorn, C., Goldschmidtboeing, F., & Woias, P. (2009). Bidirectional frequency tuning of a piezoelectric energy converter based on a cantilever beam. *J. Micromechanics and microengineering , 19* (6pp).

[18] El-hami, M., Glynne-Jones, P., White, N. M., Hill, M., Beeby, S. P., James, E., et al. (2001). Design and fabrication of a new vibration-based electromechanical power generator. *Sensors and Actuators* (335-342).

[19] *Engineering Mechanics*. (n.d.). Retrieved July 25, 2010, from Pure Bending: http://emweb.unl.edu/negahban/em325/11-Bending/Bending.htm

[20] Ferrari, M., Ferrari, V., Guizzetti, M., Ando, B., Baglio, S., & Trigona, C. (2009). Improved energy harvesting from wideband vibrations by nonlinear piezelectric converters. *Procedia Chemistry , 1* (pages 1203-1206).

[21] Gilbert, J. M., & Balouchi, F. (2008). Comparison of Energy Harvesting Systembs for Wireless Sensor Netowrks. *International Journal of Automation and computing , 5* (334-347).

[22] Glynne-Jone, P., Tudor, M. J., Beeby, S. P., & White, N. M. (2004). An electromagnetic, vibration-powered generator for intelligent sensor systems. *Sensors Actuators* (344-9).

[23] Goldschmidtboeing, F., & Woias, P. (2008). Characterization of different beam shapes for piezoelectric energy harvesting. *Journal of micromechanics and microengineering , 18* (7pp).

[24] Gonzalez, J. L., Rubio, A., & Moll, F. (2001). Human Powered Piezoelectric Batteries to Supply Power to Wearable Electronic Devices. *International Journal of Society of Materials Engineering for Resources , 10* (p34-40).

[25] Jiang, S., Li, X., Guo, S., Hu, Y., Yang, J., & Jiang, Q. (2005). Performance of a piezoelectric bimorph for scavenging vibration energy. *Smart Materials and Structures , 14* (769-774).

[26] John, W. (2009, November 6). *EETimes.com*. Retrieved June 18, 2010, from Nokia working on energy-harvesting handset: http://www.eetimes.com/electronics-news/4195530/Nokia-working-on-energy-harvesting-handset

[27] Kymissis, J., Kendall, C., Paradiso, J., & Gershenfeld, N. (1998). Parasitic Power Harvesting in Shoes. *Proceedings of the 2nd IEEE International Symposium on Wearable Computers, Pittsburgh,PA* (132-139).

[28] Lee, S., & White, R. M. (1995). Self-excited Piezoelectric Cantilever Oscillators. *Solid-State Sensors and Actuators , 1* (p417-420).

[29] Leland, E. S., & Wright, P. K. (2006). Resonance tuning of piezoelectric vibration energy scavenging generators using compressive axial preload. *Smart Material Structure* (p1413-1420).

[30] Leland, E. S., Lai, E. M., & Wright, P. K. (2007). A self-powered wireless sensor for indoor environmental monitoring.

[31] Liu, J. Q., Fang, H. B., Xu, Z. Y., Mao, X. H., Shen, X. C., Chen, D., et al. (2007). A MEMS-based piezoelectric power generator array for vibration energy harvesting. *Microelectronics Journal , 39* (5 p802-806).

[32] Mansour, M. O., Arafa, M. H., & Megahed, S. M. (2010). Resonator with magnetically adjustable natural frequency for vibration energy harvesting. *Sensors and Actuators A: Physical , In Press* (Corrected Proof).

[33] Marzencki, M. (2005). Vibration energy scavenging. *European Commission research Project VIBES of the 6th STREP Framework Program* .

[34] Mateu, L., & Moll, F. (2005). Optimum piezoelectric bending beam structures for energy harvesting using shoe inserts. *J. Intell. Material System Structure , 16* (p835-45).

[35] Mateu, L., & Moll, F. (2005). Review of energy Harvesting Techniques and Applications for Microelectronics. *In Proceedings of SPIE- The International Society for Optical Engineering, VLSI Circuits and Systems II, SPIE Press , 5837* (pp. 359-373).

[36] Meninger, S., Mur-Miranda, J. O., Amirtharaja, R., Chandrakasan, A., & Lang, J. H. (2001). Vibration-to-electric energy conversion. *Very Large Scale Integration (VLSI) Systems, IEEE Transactions on , 9* (64-76).

[37] Miller, L. M., Emiley, N. C., Shafer, P., & Wright, P. K. (2008). Strain Enhancement within cantilevered, Piezoelectric MEMS Vibrational Energy Scanveging Devices. *Advances in Science and Technology , Smart Materials &Mico/Nanosystems* (pp405-410).

[38] Minazara, E., Vasic, D., Costa, F., & Poulin, G. (2006). Piezoelectric diaphragm for vibration energy harvesting. *Ultrasonics , 44* (e699-e703).

[39] Miyazak, M., Tanaka, H., Ono, G., Nagano, T., Ohkubo, N., Kawahara, T., et al. (2003). Electric-energy generation using variable-capacitive resonator for power-free LSI: efficiency analysis and fundamental experiment. *Low Power Electronics and Design, 2003. ISLPED '03. Proceedings of the 2003 International Symposium on* (193-198).

[40] Morgan Electro Ceramics. (n.d.). *Technical Publication TP-245*. (Morgan Electro Ceramics) Retrieved July 28, 2010, from Morgan Electro Ceramics Web Site: www.morgan-electroceramics.com

[41] Ng, T. H., & Liao, W. H. (2005). Sensitivity Analysis and Energy Harvesting for a Self-Powered Piezoelectric Sensor. *Journal of Intelligent Material Systems and Structures , 16* (785-797).

[42] Paradiso, J. A., & Starner, T. (2005). Energy Scavenging for Mobile and Wireless Electronics. *IEEE Pervasive Computing , 4* (pp. 18-27).

[43] Piezo System, I. (2007). (Piezo System, Inc) Retrieved August 25, 2008, from CATALOG 2007: http://www.piezo.com/catalog.html

[44] *Piezoelectricity*. (n.d.). Retrieved Feb 4, 2007, from Hot Topics: http://www.discoverchemistry.com

[45] *Piezoelectricity*. (n.d.). Retrieved June 29, 2008, from MaterialsWorld: http://www.materialsworldmodules.org/.

[46] Qi, S., Shuttleworth, R., Oyadiji, S. O., & Wright, J. (2010). Design of a multiresonant beam for broadband piezoelectric energy harvesting. *Smart Material and Structure , 19* (pp10).

[47] Randall, J. F. (2003). On ambient energy sources for powering indoor electronic devices. *PhD thesis* . Ecole Polytechnique Federale de Lausanne, Switzerland.

[48] Roundy, S. (2003). Energy Scavenging for wireless sensor nodes with a focus on Vibration to electricity conversion. *PhD Thesis* . University of California Berkely.

[49] Roundy, S. (2005). On the effectiveness of vibration-based energy harvesting. *Journal Intell. Material System Structure , 16* (p809-23).

[50] Roundy, S., & Zhang, Y. (2005). Toward self-tuning adaptive vibration-based microgenerators. *Smart Structures, Devices, and Systems II* (373-384).

[51] Roundy, S., Leland, E. S., Baker, J., Carleton, E., Reilly, E., Lai, E., et al. (2005). Improving power output for vibration-based energy scavengers. *IEEE pervasive Computing* (28-36).

[52] Roundy, S., Steingart, D., Frechette, L., Wright, P., & Rabaey, J. (2004). Power Sources for Wireless Sensor Networks. *Lecture Notes in Computer Science, Springer-Verlag , 2920* (pp1-17).

[53] Roundy, S., Wright, P. K., & Rabaey, J. A. (2003). A study of low level vibrations as a power source for wireless sensor nodes. *Computer Communications , 26* (1131-1144).

[54] Sari, I., Balkan, T., & Kulah, H. (2008). A electromagnetic micro power generator for wideband environmental vibrations. *Sensors and Actuators , A145* (405-13).

[55] Shahruz, S. M. (2006). Design of mechanical band-pass filters for energy scavenging. *Journal of sound and vibration Volume , 292* (p987-998).

[56] Shahruz, S. M. (2006). Limits of performance of mechanical band-pass filters used in energy scavenging. *Journal of sound and vibration , 293* (p449-461).

[57] Shen, D., Park, J., Ajitsaria, J., Choe, S., Wikle III, H. C., & Kim, D. (2008). The design, fabrication and evaluation of a MEMS PZT cantilever with an integrated Si proof mass for vibration energy harvesting. *J. Micromech. & Microeng. , 18*.

[58] Shen, D., Park, J., Noh, J. H., Choe, S., Kim, S., Wikle III, H. C., et al. (2009). Micromachined PZT cantilever based on SOI structure for low frequency vibration energy harvesting. *Sensors and Actuators , A154* (p103-108).

[59] Shenck, J. S., & Paradiso, J. A. (2001). Energy scavenging with shoe-mounted piezoelectrics. *IEEE Micro. , 21* (30-42).

[60] Sodano, H. A., Inman, D. J., & Park, G. (2005). Comparison of piezoelectric energy harvesting devices for recharging batteries. *J. Intell. Mater. Syst. Structure , 16* (799-807).

[61] Sodano, H. A., Lloyd, J., & Inman, D. J. (2004). An Experiment comparison between several active composite actuators for power generation. *Smart material Structure , 15* (1211-1216).

[62] Starner, T. E. (2003). Powerful Change Part1: Batteries and Possible Alternatives for the Mobile Markat. *IEEE Pervasive Computing , 2* (pp86-88).

[63] Starner, T. (1996). Human-Powered wearable computing. *IBM Systems Journal , 3* (618-629).

[64] Stephen, N. G. (2006). On erngy harvesting from ambient vibration. *Journal of Sound and Vibration* (p409-425).

[65] Stordeur, & Stark, M. (1997). Low power Thermoelectric Generator- Self-sufficient energy supply for micro systems. *16th International Conference on Thermoelectrics* (p575-577).

[66] Sunghwan, K. (2002). Lower Power Energy Harvesting with Piezoelectric generators. *PhD Thesis* . University of Pittsburgh.

[67] Wang, P., Tanaka, K., Sugiyama, S., Dai, X., Zhao, X., & Liu, J. (2009). A micro electromagnetic low level vibration energy harvester. *Microsyst Technol , 15* (941-951).

[68] Williams, C. B., & Yates, R. B. (1996). Analysis of a micro- electric generator for microsystem. *Sensor & Actuators* (8-11).

[69] Wu, w.-J., Chen, Y.-Y., Lee, B.-S., He, J.-J., & Peng, Y.-T. (2006). Tunable resonant frequency power harvesting devices. *Smart Structures and Materials 2006: Damping and Isolation. , 6169* (pp 55-62).

[70] Zhou, Y., Paul, S., & Bhunia, S. (2008). Harvesting Wasted Heat in a Microprocessor Using Thermoelectric Generators: Modelling, Analysia and Measurement. *Design, Automation and Test in Europe* (10-14).

[71] Zhu, D., Roberts, S., Tudor, M. J., & Beeby, S. P. (2008). closed loop frequency tuning of a vibration-based micro-generator. *Proc. PowerMEMS 2008+ micro EMS2008* (pp229-32).

[72] Zhu, D., Tudor, M. J., & Beeby, S. (2010). Strategies for increasing the operating frequency range of vibration enegy harvester: a review. *Measurement Science and Technology , 21* (pp29).